ACADEMIA DA FORÇA AÉREA

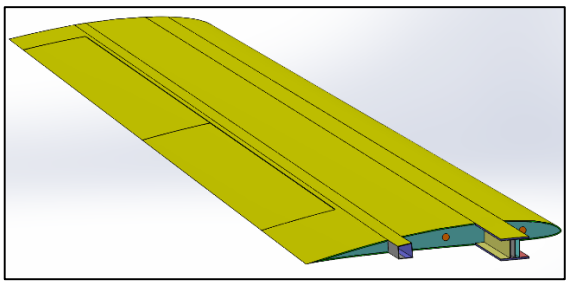

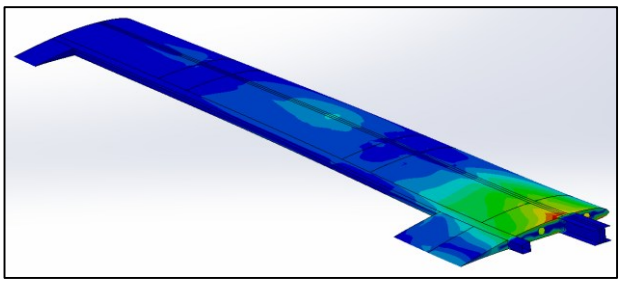

Design and Optimization of a Wing Structure for a UAS Class I 145 kg

By: **João Jorge Miguel da Silva**

AlfAl / EngAer /137735-D

A thesis to obtain the Master Degree in

Military Science

Aeronautical Engeneering

Examination Committee:

Chairperson:	Cor/EngAer Fernando António Bento de Oliveira
Supervisor:	Prof. Dr. Virgínia Isabel Monteiro Nabais Infante
Co-Supervisor:	Maj/EngAer Diogo Xufre de Sousa Duarte
Members of the Committee:	Prof. Dr. Rui Miguel Barreiros Rúben

Sintra, July 2017

"Necessity is the mother of invention"

- Proverb -

Dedicatória

Aos meus Pais por toda a educação que me deram, pelos sacrifícios que fizeram e pelo apoio e motivação constantes.

À minha Irmã por toda a amizade, apoio e companhia, e a quem desejo um grande futuro.

À minha Tia Ilda porque sem ela não teria chegado onde cheguei.

À minha Avó Francisca que na sua sabedoria muito me ensinou.

Ao meu Tio António pelo inabalável apoio moral.

Aos Quasares pelas alegrias e tribulações que me ajudaram a crescer.

Ao meu camarada Pedro Perestrelo pela amizade, companhia e grande apoio ao longo da Academia.

À minha camarada Marta Santos pela amizade, paciência e imprescindível ajuda ao longo destes últimos 6 anos.

Acknowledgements

The completion of this thesis would not have been possible without the help and the support of many people to whom I would like to show my gratitude:

I thank Major Diogo Duarte for allowing me to develop such a demanding topic / project and for his help and patience during the critical moments.

I thank Professora Virgínia Infante for always being available and especially for the precious help with the determination of the material's properties.

I thank Capitão João Caetano for all the support and guidance and also for his promptness to take care of urgent matters.

I thank the Doctoring Student Mário Vieira for this invaluable help with the data acquisition during the testing of the material's specimens.

I thank Sargento Ajudante Paulo Mendes for all his help concerning the use of equipment and materials at the CIDIFA and for this availability and willingness to discuss and exchange ideas regarding manufacturing processes.

I thank Major Aurélio Santos for all the help concerning the use of equipment at the CIDIFA.

I thank the students from Fórmula Student, especially Bogdan for his availability and tutoring on how to use the FEA software *HyperMesh*.

I thank Major Carlos Silva for having clarified some doubts about wing structural design practices.

I thank Capitão Bruno Serrano for his availability and willingness to teach how to work with the AFA's destructive testing machine.

I thank Capitão Luís Félix for providing information concerning other thesis and data concerning composite materials.

Last but not least, I also thank Capitão Dinis Paiva, Tenente Sara Monte and Alferes Marta Santos for making their thesis available.

Resumo

No contexto do poder aéreo à escala Gobal, sistemas aéreos não tripulados (UAS) apresentam-se como uma necessidade actual e futura, razão pela qual, fazem parte não só da visão estratégica da Força Aérea Portuguesa (FAP) mas também da Estratégia Nacional para o Mar 2013-2020.

Desde 2008 que a FAP tem vindo a desenvolver UAS cada vez mais capazes e, actualmente, algumas das suas plataformas experimentais encontram-se já em utilização em contextos operacionais tanto nacionais como internacionais.

Por forma a expandir essa utilização, de forma segura e responsável, para missões de busca e vigilânica sobre a vasta área sob a jurisdição de Portugal, existe a necessidade de contruir novas plataformas capazes de dar resposta a todos os requesitos operacionais e de aeronavegabilidade e de estabelecer procedimentos para a uma eventual produção em larga escala das mesmas.

Perante estas necessidades, a presente tese de mestrado consiste no design e otimização da estrutura da asa de uma nova plataforma operacional com um peso máximo à descolagem de 145 kg (UAS class I). Paralelamente ao emprego operacional, esta plataforma desempenhará também, o papel funamental de modelo de teste – à escala reduzida - de um UAS de grandes dimensões (class II), actualmente em devenvolvimento por um consórcio entre a FAP, empreas nacionais e o Ministério da Defesa Nacional (MDN).

O processo de design e otimização da asa involveu a determinação das forças a actuar sobre a estrutura (definição do envelope de voo da aeronave e identificação da situação correspondente ao carregamento crítico da asa), o planeamento da geometria geral e da disposição de compoentes, a escolha de materiais (compósitos - fabrico de provetes e determinação das suas propriedades experimentalmente) e, posteriormente, definição da geometria, dimensionamento e otimização dos vários componentes por forma a garantir a robustez estrutural da asa com o mínimo de massa e custos, possível.

Todas as desisões de design foram fundamentadas com base em regulamentos (entre eles, o NATO STANAG AEP-83), manuais de design estrutural, livros e artigos científicos, por foma a garantir a certificação da estrutura em termos de aeronavegabilidade.

O processo de otimização utilizado / criado - "chain top-down approach" - mostrou-se simples e eficaz e consistiu numa otimização individual mas interligada, de cada componente, seguindo uma sequência hierárquica, de acordo com a importância estrutural de cada um.

Todos os modelos geométricos produzidos (3D) e todas as análises estruturais efectuadas (análises numéricas através da discretização da estrutura em elementos finitos - FEA), foram realizados com recurso ao software *SolidWorks 2016 x64 Edition.*

O modelo final obtido, satisfas todos os requisitos estruturais (capaz de suportar entre -1.5 a 4 G's com deslocamento da ponta da asa < 5% do comprimento de meia envergadura), requisitos operacionais (em cada meia-asa, capaz de suportar payload suspenso ≤ 10 kg) e de peso (massa < 26.2 kg), e apresenta um custo de produção, em termos de materiais, de cerca de 3000 €.

Palavras Chave: Poder aéreo, FAP, UAS class I, design estrutural de asa, otimização estrutural, compósitos.

Abstract

In the context of air power in a Global scale, unmanned aerial systems (UAS) are a present and future necessity, reason why, they are part of the Portuguese Air Force (FAP) strategic vision and part of the Portuguese National Strategy for the Sea 2013-2020.

Since 2008 the FAP has been developing UAS ever more capable and, nowadays, some of its experimental platforms are already being used operationally, both nationally and internationally.

In order to expand their use, in a safe and responsible manner, for search and surveillance missions over the vast area under Portugal's jurisdiction, there is the necessity to manufacture new platforms capable of fulfilling all the operational and airworthiness requirements and to establish procedures for their eventual mass production.

In light of these necessities, the present master's thesis consists of the design and optimization of the structure of the wing of a new operational platform with a maximum take-off weight of 145 kg (UAS class I). Parallelly to the operational use, this platform will also play the fundamental role of being the test model – at a reduced scale – for a large UAS (class II), currently in development by a consortium between the FAP, national companies and the Portuguese National Ministry of Defense (MDN).

The wing design and optimization process, involved determining the loads acting on the structure (definition of the aircraft's flight envelope and identification of the wing's critical loading condition), planning the general shape and components layout, choosing materials (composites – manufacturing of specimens and experimental testing to obtain their properties), and then, shaping, sizing and optimizing its many components to give every part just enough strength without excess weight and also to reduce costs.

All design decision were fundamented based on regulations (e.g. the NATO STANAG AEP-83), structural design manuals, books and scientific articles, in order to guarantee the certification of the structure in terms of airworthiness.

The optimization process used / created – "chain top-down approach" – proved to be simple and effective and consisted in an individual but interconnected optimization, of each component, following a hierarchical sequence, in accordance with the structural importance of each one.

All the geometric models produced (3D) and all the structural analysis performed (numerical analysis resorting to the discretization of the structure using finite elements – FEA), were achieved by using the software *SolidWorks 2016 x64 Edition.*

The final wing model obtained, fulfilled every structural requisite (capable of enduring between -1.5 and 4 G's with a wing tip displacement < 5% of half-wing span), operational requisite (capable of carrying up to 10 kg of suspended payload from each half-wing), and weight requisite (mass < 26.2 kg), with a manufacturing cost, in terms of materials, close to 3000 €.

Keywords: Air power, FAP, UAS class I, wing structural design, structural optimization, composites.

Table of Contents

List of Figures

List of Tables

List of Acronyms

AAN	Autoridade Aeronáutica Nacional
AC	Aerodynamic Center
AFA	Academia da Força Aérea – Portuguese Air Force Academy
AI	Artificial Intelligence
ANTEX-M	Experimental Unmanned Aircraft - Military
ASTM	American Society for Testing Materials
BF	Body Force
Bi CF	Bidirectional Carbon Fiber
BLOS	Beyond the Line-of-Sight
CAD	Computer-Aided Design
CEiiA	Centro de Excelência e Inovação da Indústria Automóvel
CFRP	Carbon Reinforced Polymer
CIDIFA	Centro de Investigação, Desenvolvimento e Inovação da Forca Aérea – Portuguese Airforce Investigation, Development and Innovation Center
CNC	Computer Numerical Control
CP or C	Center of Pressure
CSW	Critical Software
DGPM	Direção Geral de Política do Mar
DGPS	Differential Global Positioning System
EAS	Equivalent Airspeed
EDA	European Defense Agency
EDP	Energias de Portugal
EEZ	Economic Exclusive Zone
EMSA	European Maritime Safety Agency
EU	European Union
FAP	Força Aérea Portuguesa - Portuguese Air Force
FCUL	Faculdade de Ciênicas da Universidade de Lisboa
FE	Finite Element
FEA	Finite Element Analysis
FEUP	Faculdade de Engenharia da Universidade do Porto
FIR	Flight Information Region
GNR	Guarda Nacional Republicana
HS	High Strength
IT	Instituto de Telecomunicações
IST	Instituto Superior Técnico
LNEC	Laboratório Nacional de Engenharia Civil
MAC	Mean Aerodynamic Chord
MDN	Ministério da Defesa Nacional
MDO	Multidisciplinary Optimization

MFA	Manual da Força Aérea
MTOW	Maximum Take-Off Weight
NASA	National Aeronautics and Space Administration
NATO	North Atlantic Treaty Organization
NHAA	Negative High Angle of Attack
NLAA	Negative Low Angle of Attack
PC	Personal Computer
PHAA	Positive High Angle of Attack
PITVANT	Projeto de Investigação e Tecnológia em Veículos Aéreos Não-Tripulados - Project of Technological Investigation in Unmanned Aerial Vehicles
PLAA	Positive Low Angle of Attack
PTInS	Portugal Telecom Innovation and Systems
RD&I	Research, Development and Innovation
REP	Rapid Environmental Picture
SAR	Search and Rescue
SF	Safety Factor
SRR	Search and Rescue Region
SSL	Standard Sea Level
STANAG	Standardization Agreement
SW	SolidWorks 2016 x64 Edition
TO	Topology Optimization
UAS	Unmanned Aircraft System
UBI	Universidade da Beira Interior
UCB	University of California and Berkley
UM	University of Munich
Uni CF	Unidirectional Carbon Fiber
UW	University of Warsaw
WWII	World War II
2D	Two Dimensions
3D	Three Dimensions

List of Symbols

α	Angle of attack
α_{root}	Wing twist at the root
α_{tip}	Wing twist at the tip
γ	Shear strain
Γ	Wing *dihedral* angle
ε	Strain
$\lambda = \frac{c_{tip}}{c_{root}}$	Wing taper ration
Λ_{LE}	Wing sweep angle (leading edge)
μ	Mass ratio
v	Viscosity / Poisson's ratio
ρ	Density
σ	Stress
σ_u	Ultimate stress or Ultimate Strength
σ_y	Yield stress or Yield Strength
τ	Shear stress
#	Number
a	Acceleration
A	Area
$AR = \frac{b^2}{S}$	Wing aspect ratio
b	Wing Span
c	Local wing chord
$\bar{c}$	Wing standard mean chord
C_l	Airfoil lift coefficient
C_L	Lift coefficient
C_{L_α}	Lift coefficient slope
C_m	Airfoil pitching moment coefficient
cm	Centimeter
C_M	Pitching moment coefficient
c_{root}	Wing chord at the root
c_{tip}	Wing chord at the tip
d	Distance between the CP and the AC along the airfoil's chord (c)
D	Drag / Diameter
E	Modulus of elasticity or Young's modulus
F	Force
F_i	Inertial forces
ft	Foot
g	Earth's gravity acceleration

G	Modulus of rigidity or Young's modulus for shear
G's	Earth's gravity acceleration
GPa	Giga Pascal
gr	Grams
H	Horizontal (x direction) component of the force resultant (R)
I	Area moment or inertia
K	Gust alleviation factor
kg	Kilogram
l	Solid's dimension
l_0	Solid's initial dimension
L	Lift
m	Mass / meter
M	Moment
mm	Millimeter
M_0	Constant pitching moment
MPa	Mega Pascal
m/s	Meters per second
n	Wing load factor
N	Normal component of the force resultant (R) / Newton
q	Dynamic pressure
r	Radius
R	Force resultant
Re	Reynold's number
rpm	Rotations per minute
S	Area of the wing platform (projected area on the horizontal plane)
sl	Sea level
T	Temperature
u	Equivalent gust velocity
$\hat{u}$	Standard gust velocity
V	Velocity
V_c	Aircraft cruise velocity
V_D	Aircraft dive velocity
V_e	Equivalent airspeed
W	Weight

1 Introduction

1.1 Framework

The work herein presented regards the development of a cost-effective unmanned aerial system (UAS) to be used for search and surveillance purposes over the vast area under the Portuguese jurisdiction.

Portugal has search and rescue (SAR) responsibilities over almost 6 million km^2 (square kilometers) of airspace from which 98% are over water (including interior waters, territorial sea and the Economic Exclusive Zone (EEZ)) [1] [2] [3] [4] [5], which makes Portugal the country holding the vastest water jurisdiction area in the European Union (EU), and the second vastest in the world [1] [2] [3] [6] [7] [8]. See Figure 1.

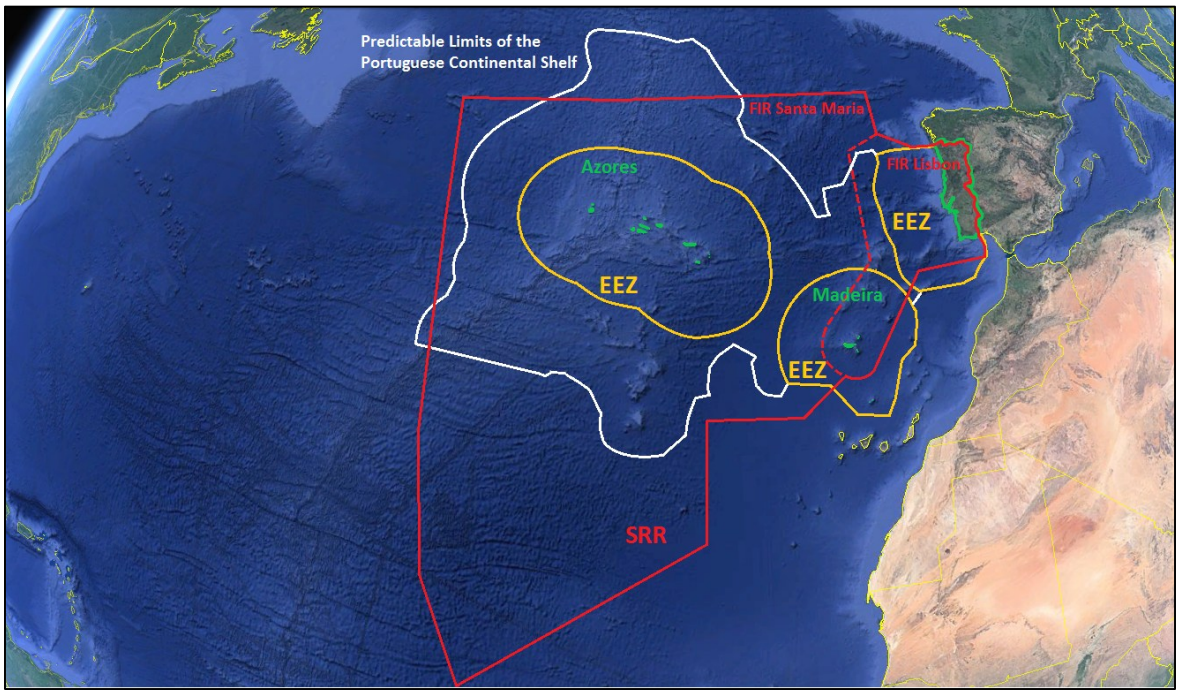

Figure 1 - Airspace, Water and Land areas under Portugal's responsibility and/or jurisdiction: Green: Land area (mainland Portugal, Archipelago of Madeira and Archipelago of Azores); Yellow: Economic Exclusive Zone (EEZ) (1.66 million km^2 [3]); White: Proposal to extend the limits of the continental shelf (3.6 million km^2 [3]); Red: Airspace under Portugal responsibility which coincides with the Search and Rescue Region (SRR) of responsibility (5.8 million km^2, divided into two Flight Information Regions (FIR) – Santa Maria and Lisbon [1]).

All of this areas require aerial presence either in the form of surveillance or patrol to ensure that the country's rights and duties are enforced and no illegal activities are performed. Also, monitoring is crucial to ensure border control and, therefore, the security and sovereignty of the Nation [4].

Missions of surveillance, patrol and SAR in the Portuguese EEZ and/or the SRR are the daily responsibility of entities such as the Portuguese Air Force (FAP), Portuguese Navy, Maritime Police, National Civil Protection Authority (ANPC), Port Authorities and others [3] [8].

The size, importance and mandatory nature of these missions, requires the existence of means/equipment/platforms (aerial, maritime and ground), that can act in an integrated manner.

In order to better assist and alleviate the operational load of these missions, the Portuguese Air Force (FAP) began, in 2008, a project of Research, Development and Innovation (RD&I) called PITVANT

(Project of Technological Investigation in Unmanned Aerial Vehicles), Figure 2. Its main objective was to develop technology in various study areas regarding small and medium-sized unmanned aerial systems (UAS). This was achieved by creating and testing new systems and technologies and also new concepts of operation, for both military and civilian applications. In addition, the personal gained *Know-how* and the ability to define operational and maintenance requisites for this type of systems [9] [10].

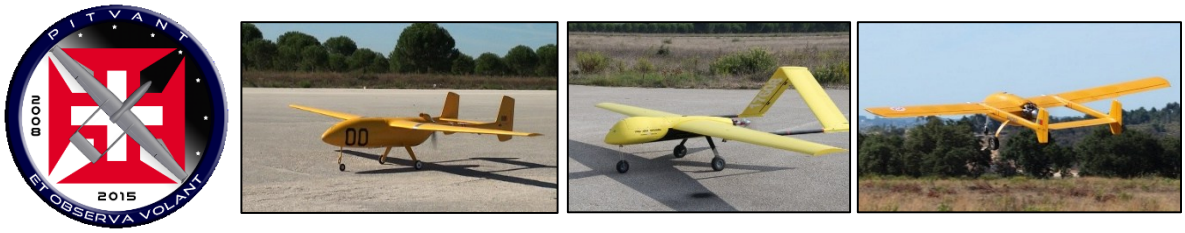

a) b) c) d)

Figure 2 – a) The project's Patch with its moto "ET OBSERVA VOLANT" [9]; b) ANTEX-X02 Alfa, UAS with maximum take of weight (MTOW) of 25 kg [11]; c) UAS30, with MTOW of 30 kg [12]; d) ANTEX-X03, with MTOW of 149 kg [13].

During the PITVANT project, which was developed in accordance with the Air Force Manual (MFA) 500-12[1], various UAS of class I[2] (Figure 2) were designed, manufactured and flown, totalizing more than 800 flight hours [14] [15] [16].

Innumerous systems were developed, tested and integrated in the platforms, which included: algorithms for identification and tracking of land features (such as coast-lines, roads, railways, etc.) and also stationary or moving targets either at sea or land; systems that allowed nocturnal flights, multiplatform coordinated flights and *beyond the line-of-sight* (BLOS) flights; multispectral cameras (including thermal); real time video feed; integration of the *Differential Global Positioning System* (DGPS) to allow for precise automatic landings; the development of an onboard Computer Architecture for an easy integration of new sensors; etc. [14] [15].

The platforms developed during this project were also put to test in various Operational Exercises such as: the maritime surveillance exercise *Rapid Environmental Picture* (REP) that took place in 2012 (REP-12) and 2013 (REP-13); the *SharpEye* exercise in 2014; the *ZARCO* exercise in 2015, which involved the three branches of the Portuguese armed forces; among others [15].

The project allowed for the acquisition and development of competences by the personal involved leading to the qualification of the first UAS operators belonging to the FAP and the training of various class I UAS operating teams [15].

[1]Portuguese Air Force Manual 500-12 entitled Strategic Foresight for Unmanned Aerial Systems [16].

[2]According to the *North Atlantic Treaty Organization* (NATO) on the classification of UAS [73], they can be divided into 3 Categories: *i*) **CLASS I**: Less than 150 kg. Divided into the Categories: MICRO (< 2 kg), MINI (2-10kg) and SMALL (>20kg); ii) **CLASS II**: 150 kg to 600 kg. Category: TACTICAL; iii) **CLASS III**: More than 600 kg. Categories based on altitude and mission: Strike/Combat (≤65,000 ft), HALE (High Altitude Long Endurance) (≤65,000 ft) and MALE (Medium Altitude Long Endurance) (≤45,000 ft). Operates at the higher altitudes and with the higher speeds, range, endurance and size.

Furthermore, during the various phases of the project, collaboration was established between the FAP and various governmental and non-governmental, military and civilian entities/companies namely: the Portuguese Navy; the Portuguese Army; the National Republican Guard (GNR); the Direção Geral de Política do Mar (DGPM); the Instituto Superior Técnico (IST); the Faculdade de Ciênicas da Universidade de Lisboa (FCUL); the Faculdade de Engenharia da Universidade do Porto (FEUP); the Universidade da Beira Interior (UBI); the Civil Engineering National Laboratory (LNEC); the Telecommunications Institute (IT); the center of excellency and innovation of the automobile industry (CEiiA); Critical Software (CSW); the UAVision; the Deimos – Engineering; the OPTIMAL; the INOVAWORKS; the INESC-Inov, the Portugal Telecom Innovation and Systems (PTInS); the Energies of Portugal – Innovation (EDP-innovation); the University of California and Berkley (UCB), the University of Saltzburg, the University of Munich (UM), the University of Delft, the University of Warsaw (UW) and the European Maritime Safety Agency (EMSA) [15].

The developed UASs achieved with success the objectives that had been set nevertheless, with the arrival of the year 2015, the project came to its end.

In order to follow in the footsteps of this project and to answer to the new operational objectives that required a certifiable platform capable of performing maritime surveillance and SAR missions (in light of the Nacional Strategy for the Sea 2013-2020), a new project was started in 2016 entitled "Industrialização e Comercialização de um Sistema Aéreo Autónomo Não Tripulado classe II". This new project had the goal to design, qualify, certify and possibly commercialize unmanned aircrafts for operational use (either military or civilian), integrating the systems that were developed and tested in the project PITVANT [14] [15] [17].

In light of this new project started in 2016, the present thesis applies to the class II UAS (Unmanned Aerial System) platform that is currently under development by a Consortium between the FAP and National companies, financed by the Portuguese Ministry of National Defense (MDN) [17].

This class II project requires the development of a scale down class I model "UAS145" (Maximum Take-Off Weight (MTOW) of 145Kg) to validate concepts and systems and optimize aerodynamics and structures.

The developed UAS145 should result in a product suitable for operational missions, and should be developed with the aim of being certifiable by the AAN (National Aeronautical Authority) in accordance with NATO regulations, replacing the ANTEX-M (Experimental Unmanned Aircraft - Military) platforms, which service life is ending due to limitations of its operational use and also due to the lack of a solid structural design which makes those platforms unsuitable for certification.

The use of the class I platform for search and surveillance purposes, in the vast area under Portugal's responsibility, demands for the optimization of its range and endurance capabilities.

The present thesis aims to answer that need by designing and optimizing the UAS145 wing structure, making it a better and more cost-effective platform.

The external geometry of the wing was previously established by the Portuguese company UAVision which was responsible for creating the class I preliminary designs.

1.2 Objectives

1.2.1 Primary

- Design a wing structure that fulfills all structural, mass and operational requirements:
  - Symmetric positive limit maneuvering load factor ≥ 3.8 and symmetric negative limit maneuvering load factor ≤ -1.5;
  - High wing stiffness - wing tip displacement ≤ 5% of the wing's half span;
  - Wing mass ≤ 26.2 [kg];
  - Each half-wing capable of carrying an external suspended payload up to 10 [kg];
  - Wing structure capable of being certifiable in terms of airworthiness.
- Optimize the structure – simplify the structure's geometry and reduce its mass while fulfilling the previous requirements:
  - Minimize weight;
  - Reduce manufacturing costs.

1.2.2 Secondary

- Create a structure capable of being used in multiple operational scenarios and environments, within and beyond the requirements:
  - Choose the most suitable materials;
  - Create multipurpose attachment areas.
- Establish a straight-forward functional methodology that allows for quick design and optimization of simple wing structures.

1.3 Conditions / Restrictions

- Use the materials available at the *Centro de Investigação, Desenvolvimento e Inovação da Força Aérea* (CIDIFA);
- Wing's external geometry established by the UAVision;
- Wing has to allow for the internal routing of electric cables for the various electronic equipment and for the wing-tip lights;
- Wing has to allow for the installation of "servo-motors" to control the ailerons and flaps;
- Wing has to allow for the installation of wing-tips / winglets.

1.4 Thesis Structure

The present thesis is comprised of **7 sections**:

Section 1 - Introduction:

- Framework – explanation of the purpose and importance of the thesis;
- Definition of the objectives and restrictions;
- Insight into the "State of the Art".

Section 2 - Wing external geometry:

- Definition of the wing's external geometric parameters and creation of an initial 3D model.

Section 3 - Forces Acting on the Wing:

- Definition of the aircraft's flight envelope;
- Identification of the critical forces and moments acting on the wing and how.

Section 4 - Wing Initial Structural Design:

- Materials selection and properties definitions via experimental procedures;
- Design of an initial structure that satisfies the structural requirements and that could be certifiable.

Section 5 - Wing Structure Analysis and Optimization:

- Structural *Finite Element Analysis* (FEA) and a 4 step "chain top-down" optimization process.

Section 6 - Wing Final Design including Flaps and Ailerons:

- Wing final design and respective 3D model;
- Summary of the wing's: structural characteristics; materials used; final mass; and manufacturing costs.

Section 7 - Conclusions and Future Work:

- Conclusions and Recommendations for future works that may give continuity to the present thesis.

1.5 Design and Optimization of Aircraft Structures - State of the Art

Designing aircraft structures is particularly challenging because their weight must be kept to a minimum while all of the needed strength and rigidity are provided, in order for the aircraft to meet all of its design requirements. Any excess structural weight often makes an aircraft cost more to build and to operate.

"Designing aircraft structures involves determining the loads on the structure, planning the general shape and layout, choosing materials, and then shaping, sizing and optimizing its many components to give every part just enough strength without excess weight. (…) Choice of materials for the structure can profoundly influence weight, cost, and manufacturing difficulty. The extreme complexity of modern aircraft structures makes optimal sizing of individual components particularly challenging" [18].

The design of an aircraft structure has inherently become an optimization process which requires a proactive approach from the designer in being able to simultaneously balance three fundamental criteria: design, materials selection and manufacturing processes.

In the last decades, major advances in composite materials and sandwich structures have revolutionized the way structures are designed as well as the tools and processes used for their manufacturing and testing.

The 3D printing technology is perhaps the most promising of those tools since, although still in its infancy, there are already 3D printers capable of not only printing polymers, ceramics and metals but also full composite structures using continuous carbon, aramid (Kevlar) or glass fibers. This will undoubtedly allow for the reduction of the complexity and the manufacturing costs of composite structures as well as increase the uniformity of the final products.

The 3D printing technology will also offer designers greater freedom to pursue more "exotic" structures that could never before be manufactured with conventional methods.

Due to the increasing complexity of the structures and the materials used, finite element analysis (FEA) has become indispensable for structural evaluation and optimization purposes.

Since tools influence the design, designers had to adapt their design practices by assuming approximations (e.g. surface approximations [19]) and decomposition strategies to cope with very high computational demands and complexities arising from the organization of optimization tasks.

Nevertheless, the exponential increase in computational power observed in the last 50 years has allowed designers to create ever more complex structures and to simulate them without the need for over-simplification.

Computer technology has evolved so much that, nowadays, almost any regular personal computer (PC) is able to run multidisciplinary optimization (MDO) processes, although time consumed might be an issue.

A "new" significant advance in design optimization is the "topology optimization" (TO) which is making full use of new advances in computer science including the development of artificial intelligence (AI). Although this technology might undermine the creative thinking of structural designers, human intervention is still expected to be part of the process by introducing boundary conditions and other necessary parameters. Figure 3 show an example of a "topological optimization process".

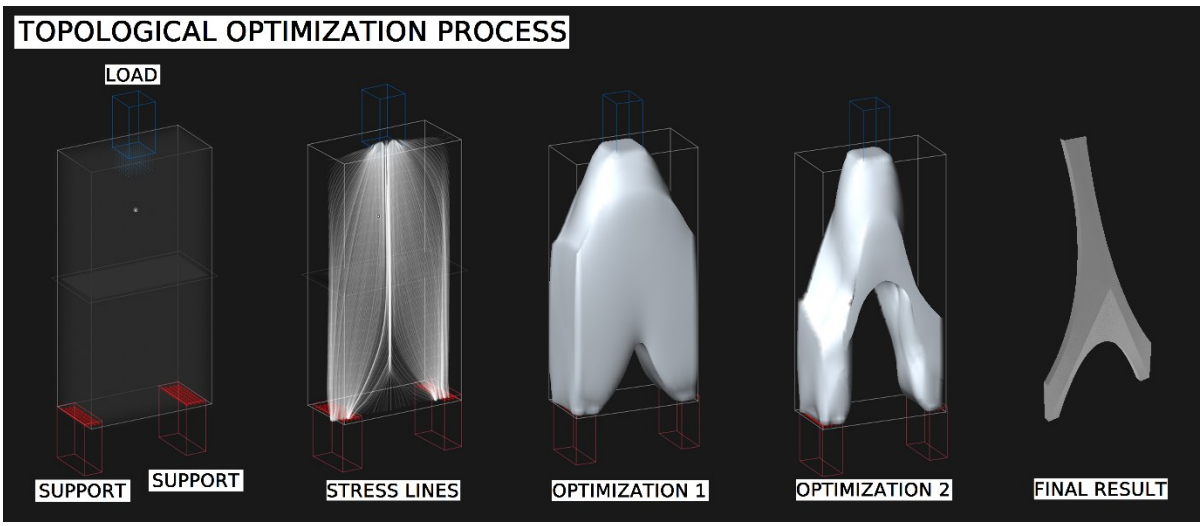

Figure 3 – Example of topological optimization process [20].

Yet, for assemblies, the mathematical fundaments and logical processes used for optimization purposes remain based on the same proven "hierarchical" and "non-hierarchical" decomposition techniques as explained by [19]. Therefore, for an assembly, although powerful software exist, a good degree of overall structural optimization can, nowadays, alternatively be accomplished by using the readily available computational power of a PC to run a "simple" software capable of performing FEA analysis and by introducing each optimization step (new geometric configuration) by hand. This may increase the overall optimization time but allows the user to avoid using complex, "heavy" and expensive software and to have full control over the optimization process.

2 Wing External Geometry

2.1 Geometric Parameters Definition

From the UAVision's document [21] containing the aircraft's preliminary specifications, the information regarding the wing geometry was selected. That information is presented in Table 1.

Table 1 –Wing External Geometry Specifications.

General	
Span (b)	6.500 [m]
Root chord (c_{root})	0.722 [m]
Tip chord $\left(c_{tip}\right)$	0.578 [m]
Taper ratio $\left(\lambda = \frac{c_{tip}}{c_{root}}\right)$	0.8
Twist at the root (α_{root})	4.4º
Twist at the tip $\left(\alpha_{tip}\right)$	0º
Sweep angle (leading edge) (Λ_{LE})	0º
Dihedral Angle (Γ)	+2º
Area of the wing platform (projected area on the horizontal plane) (S)	4.225 [m^2]
Aspect ratio $\left(AR = \frac{b^2}{S}\right)$	10
Airfoil	
Section (profile)	SELIG S4110
Maximum relative thickness location (relative to the leading edge, and measured at the local wing chord (c))	28.0%
Ailerons	
Span (each)	1.300 [m]
Relative chord (relative to the local wing chord)	30.0%
Location along the wing span	55.0%
Maximum up deflection	−25º
Maximum down deflection	25º
Flaps	
Type	Plain
Span (each)	1.300 [m]
Relative chord (relative to the local wing chord)	30.0%
Maximum down deflection	30º

2.2 Wing External Geometry Modeling

In order to better understand the wing's geometry and to establish the structure's outer limits, a 3D model was obtained using the modeling capabilities of the software *SolidWorks 2016 x64 Edition* (SW), the information presented in Table 1 and additional airfoil geometric data from [22]. That information and data allowed to define the root and tip airfoils' shape and location (see Annex 1), which were then imported into the SW allowing for the modeling of the wing's surface geometry (2D shells), shown in Figures 4 and 5 (dimensions are in [mm]).

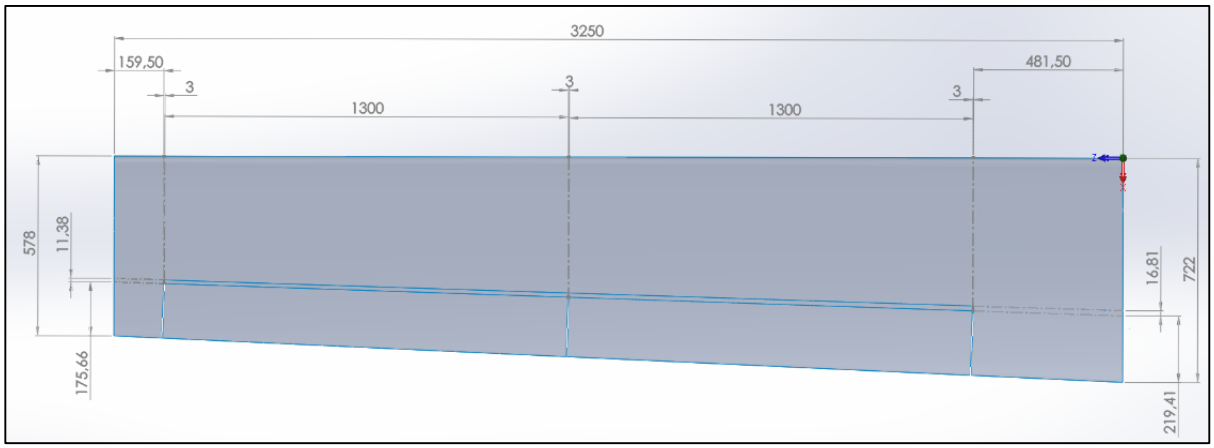

Figure 4 – Half-wing top view.

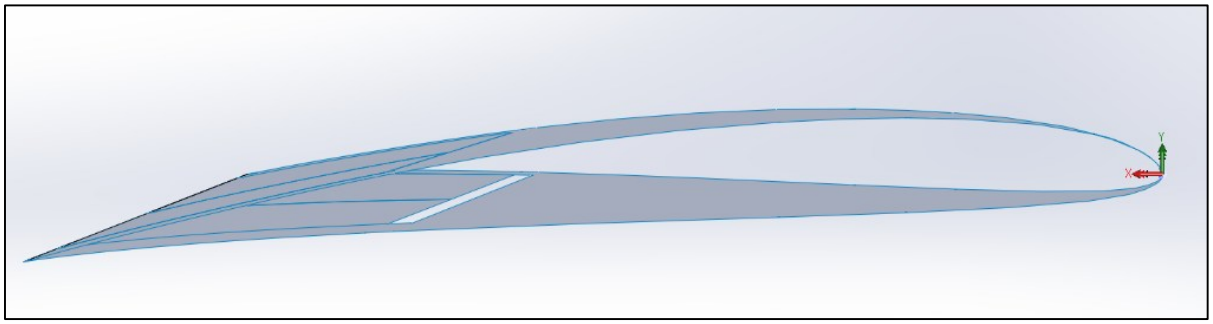

Figure 5 – Half-wing side view (root).

For modeling simplification purposes, only half wing was modeled, since the wing is symmetric in relation to the fuselage.

Also, the dihedral angle was not introduced into de model since it would only change the direction of the z and y axis. The dihedral angle can be introduced to the each half-wing when attaching them to the fuselage.

Moreover, as it can be observed in Table 1, the Flap location was not fully defined. In order to maximize the wing's structural strength – by leaving the largest possible continuous skin area near the wing root - it was decided to place the Flap next to the Aileron with a 3 mm gap separation between them, allowing for their free relative movement. For the same purpose, another two 3 mm gaps were also left between the main wing surface and the tips of both the Flap and Aileron.

Finally, a specifically dimensioned gap was left between the main wing bottom surface and bottom leading edge surfaces of both the Flap and Aileron, to allow for their maximum deflections (considering their articulation axis to be located at their top leading edge surfaces).

All gaps were created by suppressing area from the main wing surface in order to maintain the Flap and Aileron specified dimensions, thus maintaining the wing's aerodynamic characteristics.

3 Forces Acting on the Wing

3.1 Aircraft Loads Overview

The loads on an aircraft are due to a combination of static and dynamic weights, and aerodynamic forces [23].

An aircraft structure is required to support two distinct classes of load: ***ground loads***, which include all loads encountered by the aircraft during movement or transportation on the ground (e.g. landing, taxiing, towing, hoisting, etc.); and ***air loads***, which comprise loads that are imposed on the structure during flight by maneuvers and gusts (sudden, brief change in the velocity of an air mass). "The two classes of loads can be further divided into: *surface forces* which act upon the surface of the structure, e.g. aerodynamic and hydrostatic pressure; and *body forces* which act over the volume of the structure and are produced by gravitational and inertial effects" [24]. These two subclasses can be divided even further into: *point loads / concentrated loads, e.g.* catapult launching, towing, arresting external stores, and landing gear loads; and *distributed loads, e.g.* aerodynamic loads such as lift and drag, which are a result of pressures and shear stresses distributed over the aircraft surface [18].

Figure 6 shows typical force and moment resultants experienced by an aircraft in steady flight (air loads: *surface forces + body forces*).

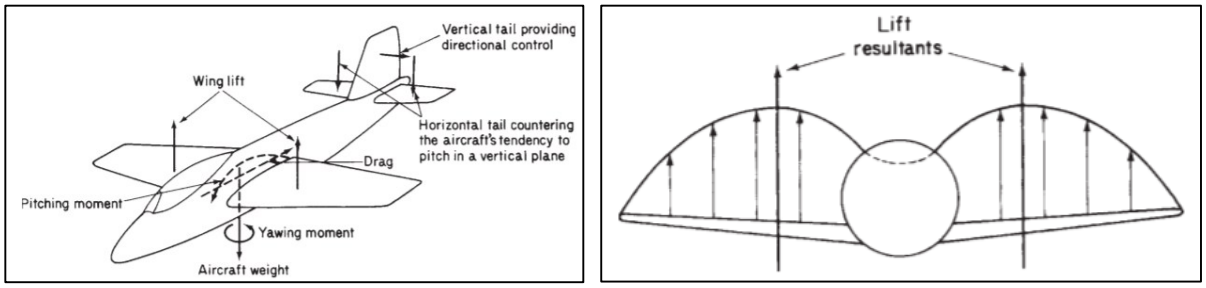

a) b)

Figure 6 – a) Typical force and moment resultants for a flying aircraft; b) Typical non-uniform lift distribution [24].

It should be noted that "maneuvers and gust do not introduce different loads but result only in changes of magnitude and position of the type of existing loads" [24].

3.1.1 Surface Forces - Aerodynamic Loads

"There are only two ways in which a fluid can impact forces to a body immersed in it. The first way, (…) is by exerting pressure perpendicular to the body's surface. If the pressures on opposite sides of a body are not equal, then a net force such as lift is exerted on the body. A portion of the drag on a moving body likewise results from pressure imbalances, but a significant portion also results from *shear* stresses exerted parallel to the body surface caused by the *viscosity* (resistance to flowing) of the fluid. In reality, lift and drag are components of a total *aerodynamic force* on the body, which is a sum of the net force caused by pressure imbalances and the net force caused by shear stresses" [18].

"Pressure loads are generally of a much greater magnitude than aerodynamic loads which are caused by shear." In other words, generally Lift >> Drag [18].

“The force on an aerodynamic surface (wing, vertical or horizontal tail) results from a differential pressure distribution caused by incidence, camber and a combination of both” [24]**.** See Figure 7 a).

“Such a pressure distribution, (…) has vertical (lift) and horizontal (drag) resultants acting at a centre of pressure (CP). (In practise, lift and drag are measured perpendicular and parallel to the flight path respectively)” [23] [24], see Figure 7 b). Also, at the CP the moment due to the lift and drag forces is zero, see and Figure 8 a).

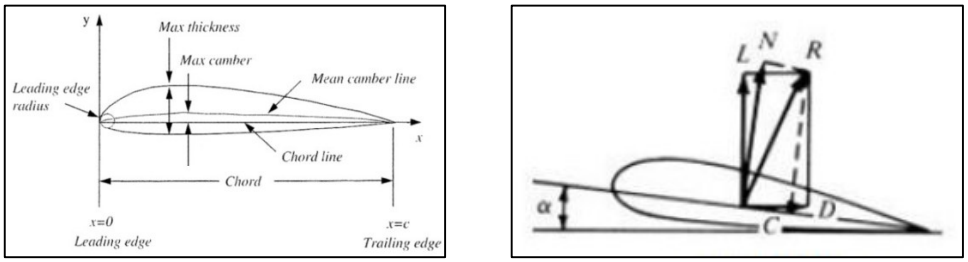

a) b)

Figure 7 – a) Airfoil Shape Parameters [18]; b) Aerodynamic Force Resultants on an Airfoil [25].

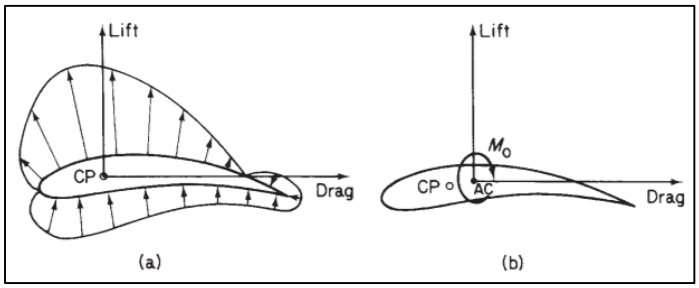

Figure 8 - a) Pressure Distribution on airfoil; b) Transference of Lift and Drag loads to Aerodynamic Center [24].

“(…) the position of the CP changes as the pressure distribution varies with speed or wing incidence. However, there is, conveniently, a point in the aerofoil section about which the moment due to the lift and drag forces remains constant. Thus we replace the lift and drag forces acting at the CP by lift and drag forces acting at the aerodynamic centre (AC) plus a constant moment M_0” [24] as shown in the Figure 8 b). This constant moment is also referred to as pitching moment.

“While the chordwise pressure distribution fixes the position of the resultant aerodynamic load in the wing cross-section, the spanwise distribution locates its position in relation, say, to the wing root” [24]. A typical distribution for a wing/fuselage combination is shown in Figure 6 b).

“Even when the pressure and shear loads on an airfoil are represented as lift-and-drag point loads at the airfoil’s center of pressure, they must be considered as a distributed load across the span of the wing” [18]. “Drag and pitching moment also have spanwise distributions. These distributions typically have their maximum magnitudes when the aircraft is maneuvering at its maximum design load factor at low altitude and high speed. If the aircraft is banking or rolling, the lift distribution is no longer symmetrical and the wing generation the most lift often has a peak in lift distribution near the deflected aileron. (…) For asymmetrical maneuvers (…), the maximum load factor limit is set by the maximum structural load that can be sustained by the most heavily loaded wing” [18], see Figure 9. The *load factor* is a relation between Lift and Weight of an aircraft and is represented by *n.*

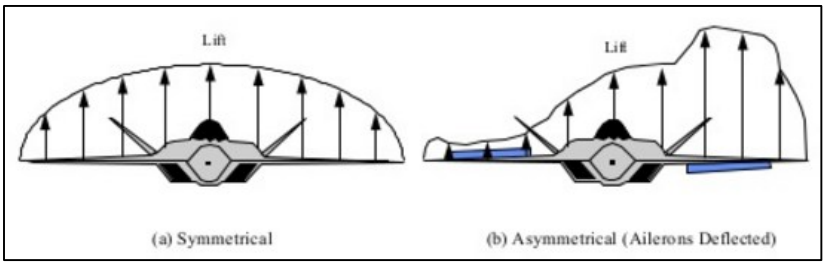

Figure 9 - Symmetrical and asymmetrical spanwise lift distributions [18].

3.1.2 Body Forces – Weight and Inertial Loads

According the Newton's second law of motion ($F_{net} = m \cdot a$), if a body has mass and it experiences an acceleration $\left(\frac{\Delta Velocity}{\Delta Time}\right)$ then, there will be an associated Force that caused it.

The Weight of a body is the Force applied by the Earth on the body. That force is calculated by multiplying the body mass (m) by the Earth's gravity acceleration (g). At sea level, the Earth's gravity acceleration is 9.81 $[m/s^2]$.

When performing a flight maneuver, the Forces acting on the aircraft are not in equilibrium ($Net\ Force \neq 0$) therefore, the body will experience an additional acceleration. That *maneuver acceleration* can be determined from the Net Force if the body mass is known or from the aircraft speed and maneuver radius.

For the same type of maneuver, the acceleration value depends on the aircraft's attitude. Figure 10 a) displays the acceleration equations for the same "pull" type maneuver but for three different aircraft attitudes.

In a maneuver, the body is said to be under dynamic conditions of the accelerated motion. The accelerated motion condition can be replaced by an equivalent set of static conditions in which the applied loads (aerodynamic loads and weight) are in equilibrium with inertial forces ($\sum F = 0$) [24]. Figure 10 b).

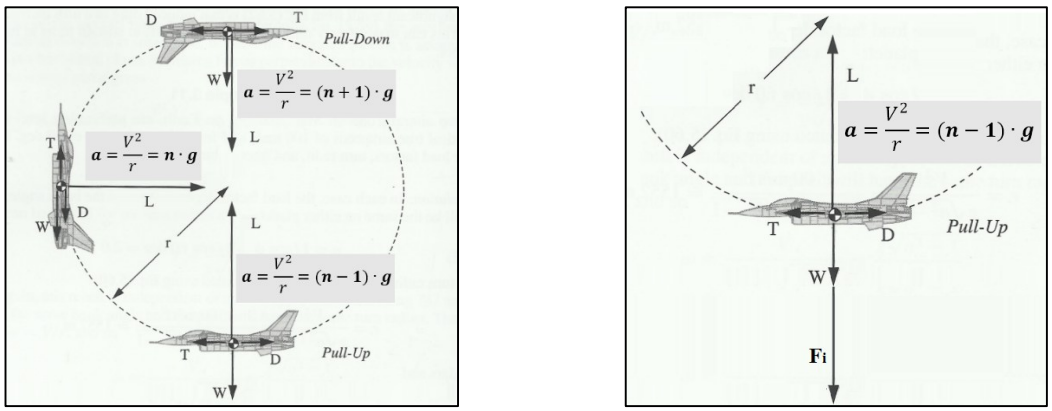

Figure 10 – a) Forces acting on an aircraft's center of gravity, at three points in a loop. Dynamic Conditions of Accelerated Motion [18]; b) Equivalent set of Static Conditions.

The inertial forces (F_i) are oriented in the opposite direction to the body acceleration. Their value is determined by multiplying the body mass (m) by the maneuver acceleration. Inertial forces caused by "pull" maneuvers are also usually called centrifugal forces.

It should be noted that in a "loop" the maximum aircraft speed will occur for the lowest position and minimum speed for the highest position as kinetic energy is exchanged by potential energy thus, the maximum and minimum load factors will also occur for the lowest and heights positions, respectively [18].

3.1.3 Wing Loads

In addition to the aerodynamic loads and inertial loads applied on the wings due its shape and structural mass, respectively, there are other loads that should also be taken into consideration.

In the specific case of payload carried on the wings, which can consist of: weapons, extra fuel tanks, electronic devices, etc., there will be additional aerodynamic and body forces contributing to the existing bending, shear and torsion of the wing [24].

Also, many aircraft have their main undercarriage located in the wings. "(...) the position of the main undercarriage should be such as to produce minimum loads on the wing structure compatible with the stability of the aircraft during ground maneuvers. This may be achieved by locating the undercarriage just forward of the flexural axis of the wing and as close to the wing root as possible. In this case the shock landing load produces a given shear, minimum bending plus torsion, with the latter being reduced as far as practicable by offsetting the torque caused by the vertical load in the undercarriage leg by a torque in an opposite sense due to braking" [24].

For the case of engines mounted on the wings, the loads caused by their thrust usually act in a plane of symmetry but may, in the case of engine failure, cause severe wing and fuselage bending moments. Also, engines will cause concentrated shock loads during hard landings and catapult launches [24].

"Before detail design of an aircraft structure can occur, the maximum magnitudes and frequencies of application, of these many loads that the aircraft must sustain in order to meet the design requirements, must be determined" [18].

The maximum loads will, therefore, establish the critical loading condition for which the structure must be designed to withstand.

For a wing, the maximum loads occur during flight. An aircraft's flight envelope provides the necessary information to determine the maximum loads the wing will be subjected to, within the aircraft's predicted operating parameters of the flight velocity (speed), load factor and altitude.

3.2 Wing Critical Loading Condition

3.2.1 Aircraft Flight Envelope

An aircraft Flight Envelope is a graph (diagram) that maps the possible combinations of maximum and minimum values of speed vs load factor that an aircraft can experience during flight. Within this "envelope" the aircraft can operate without suffering any structural damage.

This envelope results from the superposition of the *maneuvering envelope* (V-n diagram) and the *gust envelope* (V-g diagram).

3.2.1.1 Aerodynamic Load Factor

"The design of the structure is based on a load limit, which is the largest expected load. (…) this is related to the *aerodynamic load factor, n"* [23] also known as *maneuver load factor* [24] or simply by *load factor*. The load factor, *n*, is also commonly referred to as the *number of G* the aircraft is pulling, where *G* or *g* is the Earth's gravitational acceleration [18]. The load factor, *n* is given by:

$$n = \frac{L}{W} \tag{1}$$

Where *L* is the lift and *W* the weight of the aircraft.

When n = 1, *L*=*W*, the aircraft is in equilibrium (level flight) and so the aircraft is subjected to 1 *G*. 0 *G* situation would correspond to when Lift = 0 (free fall).

When designing a structure the load factor that should be used is the *design load factor*, n_{design}, which represents the ultimate load that the structure is designed to withstand without suffering permanent deformation or failure. It is given by:

$$n_{design} = Load\ SF \cdot n_{limit} = Load\ SF \cdot (n_{max} + \Delta n) \tag{2}$$

Where:

- *Load SF* is the *load safety factor* (≥1.5 being the standard for the aircraft industry for structures whose failure would lead to a Hazardous or more serious failure condition [26]). Also, according to [26] regulations an additional factor ≥1.5 should be applied for composite structure where specimen were tested with no specific allowance for moisture and temperature;
- n_{limit} is the *limit load factor*, being the sum of the highest of all load factors (n_{max}) from the maneuvering envelope (V-n) of an aircraft, with the incremental load due to turbulent gusts (Δn) [23].
- n_{limit} is usually obtained directly from the aircraft's flight envelope which is the result of combining the maneuvering envelope (V-n) with the gusts envelope (V-g) [25].

3.2.1.2 V-n Diagram

The maneuvering envelope is a graph of the Aircraft's Equivalent Velocity vs Load Factor (V-n diagram). For the maneuvering envelope, the aircraft is considered to be in "symmetric" flight, which means, no side-slipping, rolling or yawing.

For non-acrobatic aircrafts such as the one being considered, the flight envelope is designed for the maximum take-off weight (MTOW) also called *all-up weight* [25]. This corresponds to the total weight of the aircraft with passengers (non-existent in this case), cargo and fuel. Also, it is designed for a "clean configuration" (no high lift devices deployed (e.g. flaps)). It should be noted that a "dirty configuration" only extends the flight envelope towards lower velocities but also decreases the maximum load factor that can be reached. This can be observed in the Figure 12.

The aerodynamic forces typically have their maximum magnitudes when the aircraft is maneuvering at low altitude, at high speed and at its maximum load factor [18] therefore, the V-n will be obtained for *sea level conditions* (*sl*) [27].

The overall aerodynamic parameters of the aircraft were obtained from the UAVision document [21] and, the airfoil parameters, from [22].

The steps taken in order to obtain the V-n Diagram were as follows:

- $C_{L_{max_{(clean)_{aircraft}}}} = 1.35$ [21]

"The **Equivalent Airspeed (EAS)** (V_e) is an airspeed at sea level (ρ_{sl} *or* ρ_0) that would result in the same dynamic pressure experienced by the aeroplane flying at altitude at its true airspeed. (...) A constant equivalent airspeed will give the same lift at all altitudes for the same gross weight and load factor" [25].

$q = \frac{1}{2} \cdot \rho \cdot V^2$ (Dynamic pressure) (3)

$q_{cruise} = \frac{1}{2} \cdot \rho_{1500m} \cdot V^2_{cruise_{1500m}} = 2530.84 \left[\frac{kg}{m \cdot s^2}\right]$

$\rho_{1500m} = 1.084\ [kg/m^3]\ for, T = 5ºC \equiv 278.3ºK$ (According to the International Standard Atmosphere (ISA) [27])

$V_{cruise_{1500m}} = 68.33\ [m/s]$; $\rho_{sl} = 1.225\ \left[\frac{kg}{m^3}\right]\ for\ T = 15º\ C \equiv 288º\ K$

- Cruise velocity at sea level: $V_{cruise_{sl}} = V_e = 64.28\ [m/s]$

According to [26] a positive margin between the maximum design speed (V_{dive}) and the maximum operating speed $\left(V_{cruise_{max}}\right)$ should exist and the maximum operating speed should be no more than 0.9 the maximum design speed:

$$\frac{V_{cruise_{max}}}{V_{dive}} \leq 0.9 \rightarrow V_{dive} \geq 1.11\, V_{cruise_{max}}$$

It was decided to use a factor of 1.5 according to [23].

- Design / Dive velocity: $V_{dive_{sl}} = 1.5 \cdot V_{cruise_{sl}} = 96.42\ [m/s]$

- Curve from $n = 0$ to PHAA (Positive High Angle of Attack) (Positive Stall Limit):

$$n_{max}(V_\infty) = 0.002358 \cdot V_\infty^2$$

$$n_{max}(V_\infty) = \frac{C_{L_{max}} \cdot \rho \cdot S}{2 \cdot W} \cdot V_\infty^2 = \frac{C_{L_{max_{(clean)_{aircraft}}}} \cdot \rho_{sl} \cdot S_{(clean)_{aircraft}}}{2 \cdot MTOW_{sl}} \cdot V_\infty^2 \quad (4)$$

$MTOW_{sl} = 145\ [kg] \cdot g_{sl} = 145 \cdot 9.81 = 1422.45\ [N]$

$S_{(clean)_{aircraft}} = 4.057\ [m^2]$ Obtained from the V_{stall} equation:

$$V_{stall}(n) = \sqrt{\frac{2 \cdot n \cdot W}{\rho \cdot S \cdot C_{L_{max}}}}\ [m/s] \quad (5)$$

$V_{stall_{2500m}} = 22.78\ [m/s]$ [21]

For $n = 1, W = MTOW_{2500m}, S = S_{aircraft}$

$\rho_{2500m} = 1\ [kg/m^3]\ for\ T = -1.24ºC \equiv 271.8ºK$

$MTOW_{2500m} = 145\ [kg] \cdot g_{2500m} = 145 \cdot 9.8 = 1421\ [N]$

$C_{L_{max}} = C_{L_{max_{(clean)_{aircraft}}}} = 1.35$

- Curve from $n = 0$ to NHAA (Negative High Angle of Attack) (Negative Stall Limit):

$$n_{min}(V_\infty) \approx -0.000639 \cdot V_\infty^2$$

$$n_{min}(V_\infty) = \frac{C_{L_{min}} \cdot \rho \cdot S}{2 \cdot W} V_\infty^2 \approx \frac{C_{L_{max\,(clean)}\,aircraft} \cdot \frac{C_{l_{min}\,airfoil}}{C_{l_{max}\,airfoil}} \cdot \rho_{sl} \cdot S_{(clean)\,aircraft}}{2 \cdot MTOW_{sl}} \cdot V_\infty^2 \quad (6)$$

For Standard Sea level (SSL) [27]:

$Temperature\ of\ fluid: T = 288.15\ [K]$ (15 [ºC]),

$Kinematic\ viscosity\ of\ fluid: v_{sl} = 1.460 \times 10^{-5} [m^2/s]$

$$q_{stall} = \frac{1}{2} \cdot \rho_{2500m} \cdot V_{stall_{2500m}}^2 = 259.464 \left[\frac{kg}{m \cdot s^2}\right]$$

$Velocity\ of\ fluid\ (air): V = V_e = V_{stall_{sl}} = 20.58\ [m/s]$,

$\rightarrow Re = \frac{V \cdot c_{root}}{v} = 1{,}017{,}720$ and $Re = \frac{V \cdot c_{tip}}{v} = 814{,}742$ (7)

Airfoil: SELIG S4110 → $C_m\ vs\ \alpha$ plot for $Re = 1{,}000{,}000$ (highest Reynold's number plot available) [22]

$C_{l_{max\,airfoil}} = 1.625$; $C_{l_{min\,airfoil}} = -0.44$

- Limit Load Factors:

According to [26] a symmetric positive limit maneuvering load factor ≥3.8 and a symmetric negative limit maneuvering load factor ≤-1.5 should be established.

"Maneuvering load factors lower than the above may be used if the UAS has design features that make it impossible to intentionally exceed these values in flight" [26].

It was decided to use the following factors:

- $n_{max} = 4$; $n_{min} = -1.5$

- The resulting V-n Diagram is shown in Figure 11.

3.2.1.3 Gust Diagram

The gust envelope is a graph of the Aircraft's Equivalent Velocity vs Load Factors Created by Gusts (V-g diagram).

The steps taken in order to obtain the V-g Diagram were as follows:

$$n_{gust_{1,2,3}}(V_\infty) = 1 \pm \frac{\rho_{sl} \cdot V_\infty^2 \cdot S_{stall(clean),\ cruise(clean),\ dive\,(clean)\,aircraft} \cdot C_{L_\alpha} \cdot tan^{-1}\left(\frac{u_1, u_2, u_3}{V_\infty}\right)}{2 \cdot MTOW_{sl}} \quad (8)$$

$$\boldsymbol{n_1(V_\infty) = 1 \pm 0.000173 \cdot tan^{-1}\left(\frac{6.67}{V_\infty}\right) \cdot V_\infty{}^2}$$

$$\boldsymbol{n_2(V_\infty) = 1 \pm 0.00018 \cdot tan^{-1}\left(\frac{13.33}{V_\infty}\right) \cdot V_\infty{}^2}$$

$$\boldsymbol{n_3(V_\infty) = 1 \pm 0.00018 \cdot tan^{-1}\left(\frac{17.60}{V_\infty}\right) \cdot V_\infty{}^2}$$

$S_{stall\,(clean)_{aircraft}} = 4.057\ [m^2]$; $S_{cruise\,(clean)_{aircraft}} \approx S_{dive\,(clean)_{aircraft}} \approx S_{wing} = 4.225\ [m^2]$

Where: $u = K \cdot \hat{u}$ (9) $K = \frac{0.88 * \mu}{5.3 + \mu}$ (10) $\mu = \frac{2 \cdot W}{S \cdot \rho \cdot g \cdot \bar{c} \cdot C_{L_\alpha}}$ (11)

K is the gust alleviation factor. It is introduced in order to account for the behavior of the gust which do not act instantaneously but rather in a sinusoidal manner. μ is the mass ratio in order to take into account the aircraft's dimension – the lighter the aircraft, the quicker the effect of the gust. $\hat{u}$ is the standard gust velocity

value established by airworthiness authorities [28] - there are three values, one for each of the following flight speeds: Max $V_{stall}, V_{cruise}, V_{dive}$.

The values for $\hat{u}_1, \hat{u}_2$ *and* $\hat{u}_3$ were obtained from [23].

$u_1 = K \cdot \hat{u}_1 = 6.67[m/s]; \qquad u_2 = K \cdot \hat{u}_2 = 13.33\ [m/s]; \qquad u_3 = K \cdot \hat{u}_3 = 17.60\ [m/s]$

$$K_{1,2,3} = \frac{0.88 * \mu_{1,2,3}}{5.3 + \mu_{1,2,3}}$$

$$\mu_{1,2\ or\ 3} = \frac{2 \cdot W}{S \cdot \rho \cdot g \cdot \bar{c} \cdot C_{L_\alpha}} = \frac{2 \cdot MTOW_{sl}}{S_{stall(clean),\ \ cruise\ or\ dive\ (clean)_{aircraft}} \cdot \rho_{sl} \cdot g_{sl} \cdot \bar{c} \cdot C_{L_{\alpha aircraft}}} = 906.793;\ 870.736$$

Wing standard mean chord $\bar{c} = 0.650\ [m]$ [21]; $\qquad C_{L_{\alpha aircraft}} = 0.099\ [/º]$ [21]

- The resulting V-g Diagram is shown in Figure 11.

3.2.1.4 Combined Flight Envelope

As mentioned previously, the combined flight envelope for an aircraft results from the superposition of the V-n and V-g diagrams, as shown in Figure 11. The graphs are then combined in order for the final flight envelope to include the maximum values of load factor expected to occur, for in any flight situation. A typical combined flight envelope in shown in Figure 12.

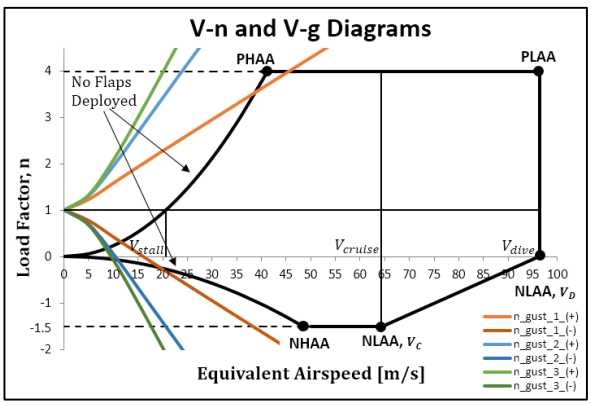

Figure 11 - Superposition of V-n and V-g diagrams.

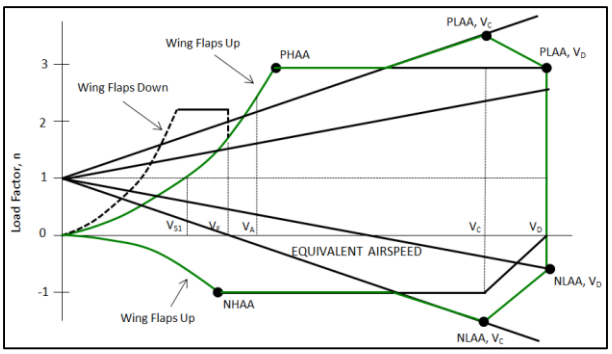

Figure 12 - Typical combined flight envelope [25].

Because the mass of the aircraft is small (MTOW – 145 kg), the standard gust values of 25, 50 and 66 [ft. /s] or 7.62, 15.24, 20.12 [m/s] result in large values of load factor that greatly surpass the maneuver envelope and, therefore, don't allow for a typical combination of both diagrams.

The solution will be to discard the influence of the wing gusts (V-g) and consider that the flight envelope of the aircraft corresponds to the maneuvering envelope (V-n), only.

Regarding this simplification, the reader should understand that, despite STANAG 4703 stablishes the requirement that wing gusts must be taken into account in the certification process of UASs, the EDA (European Defense Agency) has worked towards dividing UASs into 3 categories, where, 1 and 2 may only require an authorization resulting from a risk assessment of the aircraft's operational use. For these cases, the Nations assume the risk of not fulfilling or only partial fulfilling some requisites. In fact, the requirement to include wind gusts is one of them [29].

3.2.2 Wing Loading Conditions

According to [30], five basic conditions (shown in Figure 11) can be considered relevant for the analysis of the limit load conditions:

Positive High Angle of Attack (PHAA) – Corresponds to the positive stall angle and the minimum velocity at which the maximum load factor can be achieved.

Positive Low Angle of Attack (PLAA) – Corresponds to the lowest positive angle of attack that generates the maximum lift at maximum design speed, also known as dive speed;

Negative High Angle of Attack (NHAA) – Corresponds to the negative stall angle and the minimum velocity at which the maximum negative load factor can be achieved;

Negative Low Angle of Attack (NLAA, V_C) – Corresponds to the minimum load factor at design cruise speed;

Negative Low Angle of Attack (NLAA, V_D) – Corresponds to zero load factor at dive speed.

Each stringer and spar is either under tension or compression for each of these conditions [25]. See Figures 13 and 14.

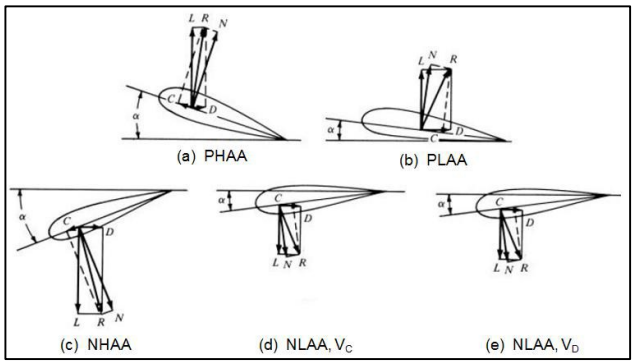

Figure 13 - Limit wing loading conditions as defined by the aircraft flight envelope [31].

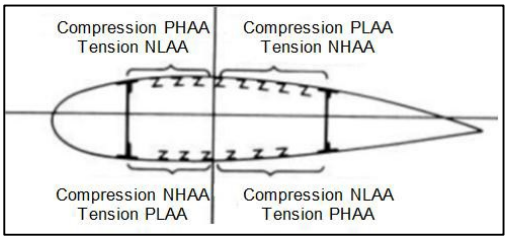

Figure 14 - Stress response as a function of the angle of attack [31].

3.2.2.1 Wing Critical Loading Condition Identification

Considering a wing to be, approximately, a tubular beam with a cross-section wider that taller, the situation that maximizes bending moments - caused by loads perpendicular to the horizontal direction - will correspond to the occurrence of maximum stresses. The tension (+) or compression (-) stress caused by a bending moment is given by:

$$\sigma = \frac{M \cdot y}{I} \text{ [Pa] or [N/m}^2\text{] (SI)} \quad (12)$$

Where M is the bending moment in a beam as a result of the load, I is the *area moment of inertia* of a beam's cross-sectional shape; and y is the vertical position in a beam cross section (measured from its neutral axis).

Therefore, for the same aerodynamic load factor ($n = \frac{L}{W}$) (same lift), limit situations of LAA will lead to higher stresses when compared to HAA - the Resultant Normal Load (N) of LAA > Resultant Normal load of HAA (assuming that the drag for both situations is approximately identical in value - HAA will mostly have an induced type drag while LAA will mostly experience a parasitic/pressure type drag). See Figure 13.

Also PLAA will lead to higher stresses than NLAA because n_{limit} positive > n_{limit} negative.

Based on the above, the point (in Figure 11) which corresponds to the aircraft's wing critical loading condition is the PLAA point.

3.2.3 Wing Critical Loading Condition Characterization

3.2.3.1 Flight Condition

The PLAA point represents a flight condition in which the airplane is flying at maximum design / dive speed (V_D) and at $n_{limit} = 4$.

Considering the aircraft's main mission (surveillance), the most probable maneuver - in terms of occurrence – that corresponds to this flight condition, would be a dive followed by a "pull-up"– symmetric maneuver.

Although the aircraft's flight envelope only accounts for symmetric maneuvers, there are also asymmetric maneuvers or combinations of maneuvers that can correspond to this flight condition. Thus, another possibility for this flight condition could be a flight situation where the dive is followed by a "pull-up" + "roll"– asymmetric maneuver. See Figure 9.

For both situations, the aircraft is assumed to be in a horizontal trajectory (and belly down) – Figure 10 b).

3.2.3.2 Loads Identification

Both previous maneuvering situations are in a state of accelerated motion. In order to perform a static analysis of an aircraft's structure it is necessary to "replace the dynamic conditions of the accelerated motion by an equivalent set of static conditions in which the applied loads are in equilibrium with the inertial forces" [24]**,** see Figure 10.

Also, it can be assumed that forward speed (V_D) remains constant considering that the maneuver is carried out rapidly, according to [24]. This approximation discards any inertial force in the forward direction caused by a decrease in forward velocity over the elapsed time.

Inertial forces in the outward direction (wing span direction – Z direction -), due to the "roll" motion, can also be discarded as they would only contribute to an increase of the structural stiffness of the wing and a consequent decrease in displacement and maximum stresses at its root [32].

All the previous approximations are conservative.

Additionally, the present wing has a payload pod mounted on its outer lower surface. This will lead to aerodynamic forces acting on the pod in the form of viscous drag (see section 3.1.1). Those forces will in turn be transmitted to the wing, together with the correspondent wing positive pitching moment (nose down moment). However, since this moment is contrary to the wing's pitching moment caused by lift and drag, and since the drag force on the pod is small due to its small cross-sectional area in association with its fusiform shape (aerodynamic shape), the conservative approximation to dismiss its aerodynamic forces contribution can be made.

This is a conservative approximation because, for a wing, torsion is more critical than bending and the torsional moment created by the pod decreases the overall wing pitching moment.

In accordance with the above, the forces acting on the wing – in a static condition- for each of the previous maneuvering situations will now be described:

First flight situation – symmetric maneuver – dive followed by "pull-up" and aircraft in a horizontal trajectory (see Figure 10 b)):

Forces acting on half-wing (static condition):

$$\begin{aligned}\sum F_{perpendicular_{half-wing}} &= N_{half-wing} - \mathrm{W}_{half-wing_{perpendicular-component}} \\ &- \mathrm{F}_{inertial_{perpendicular-component}} + F_{root-cantilever}\end{aligned} \tag{13}$$

$$\rightarrow due\ to\ low\ \alpha\ and\ D \ll L \rightarrow$$

$$\sum F_{perpendicular_{half-wing}} \approx \frac{L_{wing}}{2} - \left(W_{half-wing} + F_{inertial}\right) \cdot \cos(\alpha) \cdot \cos(\Gamma) + F_{root-cantilever} \tag{14}$$

Where N is the normal (to the wing) component of the force resultant (R) of the vector sum of lift (L) with drag (D); α is the wing angle of attack and Γ is the wing dihedral angle. (See Figure 7 b)).

Note: $N = \cos(\alpha) \cdot R = \cos(\alpha) \cdot \sqrt{L^2 + D^2} \rightarrow due\ to\ D \ll L \rightarrow\ N \approx \cos(\alpha) \cdot L \rightarrow due\ to\ low\ \alpha \rightarrow N \approx L$

$$\begin{aligned}\sum F_{horizontal_{half-wing}} &= H_{half-wing} + \left(F_{inertial} + W_{half-wing}\right) \cdot \cos(90 - \alpha) \cdot \cos(\Gamma) + F_{root-cantilever} \\ &= -\cos(90 - \alpha) \cdot L + \cos(\alpha) \cdot \mathrm{D} + \left(F_{inertial} + W_{half-wing}\right) \cdot \cos(90 - \alpha) \\ &\cdot \cos(\Gamma) + F_{root-cantilever}\end{aligned} \tag{15}$$

Where H is the horizontal (x direction) component of the force resultant of the vector sum of lift with drag.

Second flight situation – asymmetric maneuver – "pull-up" + "roll" and aircraft in a horizontal trajectory:

Knowing that the half-wing in study has an aileron that extends approximately half of the distance between the wing root and tip, the conservative approximation, that the total lift created by the aircraft is concentrated in the half-wing, could be used. As drag is a function of lift, its value would also increase.

Forces acting on half-wing (static condition):

$$\begin{aligned}\sum F_{perpendicular_{half-wing}} &= N_{half-wing} - \mathrm{W}_{half-wing_{perpendicular-component}} - \mathrm{F}_{inertial_{perpendicular-component}} \\ &+ F_{root-cantilever}\end{aligned}$$

$$\rightarrow due\ to\ low\ \alpha\ and\ applying\ Lift\ conservative\ approximation \rightarrow$$

$$\sum F_{perpendicular_{half-wing}} \approx L_{wing} - \left(W_{half-wing} + F_{inertial}\right) \cdot \cos(\alpha) \cdot \cos(\Gamma) + F_{root-cantilever} \tag{16}$$

$$\begin{aligned}\sum F_{horizontal_{half-wing}} &= H_{half-wing} + \left(F_{inertial} + W_{half-wing}\right) \cdot \cos(90 - \alpha) \cdot \cos(\Gamma) + F_{root-cantilever} \\ &= -\cos(90 - \alpha) \cdot L + \cos(\alpha) \cdot \mathrm{D} + \left(F_{inertial} + W_{half-wing}\right) \cdot \cos(90 - \alpha) \cdot \cos(\Gamma) \\ &+ F_{root-cantilever}\end{aligned}$$

From the above, the flight condition that would result in the highest bending moments in the perpendicular direction (y direction - wing coordinate system), corresponds to the situation in which the airplane would be flying at maximum design dive speed (V_D) while performing a "pull-up" + "roll" maneuver at $n = n_{limit} = 4$ and in a horizontal trajectory (Earth coordinate system).

However, considering the occurrence frequency probability of each situation associated with the main mission type of the aircraft (surveillance - far from an acrobatic type mission) and knowing that the load distributions across the wing span are different for symmetric and asymmetric maneuvers (see Figure 9), a new hypothetical critical situation, that joins both previous situations, could be created.

The "joint-situation" would maintain the forces of the second situation but the span-wise force distributions of the first.

By combining both situations, the structure would be able to resist both type forces, and also be least susceptible to failure due to fatigue (see section 4.2.5) as it would be over dimensioned for the type situation with the highest occurrence frequency probability (first situation). The "joint-situation" would undoubtedly lead to a safe structure capable of enduring any flight situation within the flight envelope.

However, designing the wing structure for the "joint-situation" would mean greatly overdesigning it, and consequently, would correspond to a considerable increase in the overall aircraft weight.

Since weight should be minimized for economic reasons, by analyzing the operational requirements of the aircraft, any "roll" maneuver could be limited to $n = 2$ (via the autopilot or other control systems) thus, resulting in:

$$\begin{aligned} \sum F_{perpendicular_{half-wing}}(\text{2nd situation}) &= \sum F_{perpendicular_{half-wing}}(\text{1st situation}) \\ &= L_{wing}/2 - \left(W_{half-wing} + F_{inertial}\right) \cdot \cos(\alpha) \cdot \cos(\Gamma) + F_{root-cantilever} \end{aligned} \tag{18}$$

Also, according to the certification specifications [33], when designing an aircraft structure, the effect of the force resultant acting in each direction should be studied separately. Therefore, considering the objective of the project at hand, the wing structure will be designed to withstand the critical force resultant in the critical direction and no other forces resultants will be considered simultaneously.

As explained in section 3.2.2.1, the critical loading direction is the one perpendicular to the wing (y direction). In that direction, the critical forces acting on the wing – for a static condition – are Lift, the wing's Weight, the wing's Inertial forces and the root forces resultant from the wing-to-fuselage attachment,

Since, for this aircraft, the wing's critical loading condition has been identified as the point PLAA, with $V = V_D \rightarrow V_e = 96.42\ [m/s]$, $n_{limit} = 4$, more specifically, for a dive condition followed by a "pull-up" maneuver and with the aircraft on a horizontal trajectory (Figure 10 b)), the correspondent maximum force resultant, on the wing, for a static condition, occurs in the y direction (wing coordinate system) and is given by:

$$\sum \boldsymbol{F_{perpendicular_{half-wing}}} \approx \frac{\boldsymbol{L_{wing}}}{\mathbf{2}} - \left(\mathbf{W_{half-wing}} + \boldsymbol{F_{inertial}}\right) \cdot \boldsymbol{cos}(\boldsymbol{\alpha}) \cdot \boldsymbol{cos}(\boldsymbol{\Gamma}) + \boldsymbol{F_{root-cantilever}} \tag{19}$$

Finally, further discretization and description of these forces and of their distributions, placement and associated moments is needed before any attempt to calculate stresses and displacements is made.

3.2.3.3 Loads Characterization

Aerodynamic Loads

Wing Lift

From the information of the lift slope for wing alone ($CL_{\alpha_{wing}} = 0.087/º$) and the lift slope for wing + fuselage + tails ($CL_{\alpha_{aircraft}} = 0.099/º$), provided by [21], it is possible to conclude that:

$$L_{wing} = \frac{0.087}{0.099} \cdot L_{aircraft} \approx 0.88 \cdot L_{aircraft}$$

However, this is only true for some situations, depending on the aircraft attitude and control surfaces deflection. Hence, the conservative approximation of $L_{wing} \approx L_{aircraft} = n \cdot W_{aircraft}$ will be used instead.

Wing Lift Distribution

Wing Geometry: Trapezoidal wing with constant tapper and twist.
Method: SCHRENK method.

"As a result of the finite aspect ratio of any wing, the lift distribution will vary along the wingspan, from a maximum near its root to a minimum near its tip" [23]. Also, [23] has shown that the spanwise lift distribution should be proportional to the shape of the wing planform.
In the case of an elliptical planform, the local chord distribution, $c(z)$ is given as:

$$c(z) = \frac{4 \cdot S_{Wing}}{\pi \cdot b} \sqrt{1 - \left(\frac{2 \cdot z}{b}\right)^2} \tag{20}$$

And the correspondent analytic spanwise lift distribution is given by:

$$L^E_{wing}(z) = \frac{4 \cdot L_{wing}}{\pi \cdot b} \sqrt{1 - \left(\frac{2 \cdot z}{b}\right)^2}, \text{ with } -b/2 \leq z \leq b/2 \tag{21}$$

The analysis of an elliptic planform wing shows that it results in an elliptic spanwise lift distribution. This result is the basis for a semi-empirical method to estimate the spanwise lift distribution on untwisted wings with general trapezoidal shapes. This method has been attributed to SCHRENK (1940) and assumes that the spanwise lift distribution of a general untwisted wing has a shape that is the average between the actual planform chord distribution, and that of the elliptical wing [23]. See Figure 15.

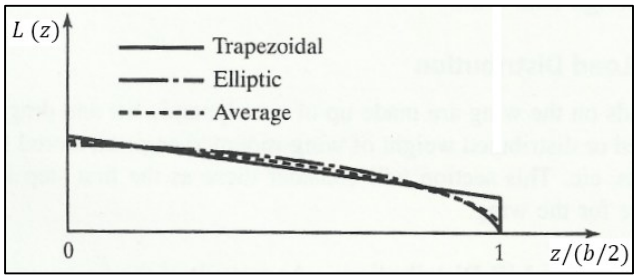

Figure 15 - Average of two lift distributions using Schrenk's approximation [23].

For the trapezoidal wing, the local chord length varies along the span as follows [23]:

$$c(z) = c_{root} \cdot \left[1 - \frac{2 \cdot z}{b} \cdot (1 - \lambda)\right] \tag{22}$$

The correspondent spanwise lift distribution is given by:

$$L^T_{wing}(z) = L_{root} \cdot \left[1 - \frac{2 \cdot z}{b} \cdot (1 - \lambda)\right] \tag{23}$$

The lift value is obtained by integrating the lift distribution over the span:

$$L = \int_{-b/2}^{b/2} L^T(z) \cdot dz = 2 \cdot L_{root} \cdot \int_0^{b/2} \left[1 - \frac{2 \cdot z}{b} \cdot (1 - \lambda)\right] \cdot dz$$

$$L = \frac{L_{root} \cdot b \cdot (1+\lambda)}{2} \rightarrow L_{root} = \frac{2 \cdot L}{b \cdot (1+\lambda)} \tag{24}$$

And, therefore,

$$L^T_{wing}(z) = \frac{2 \cdot L_{wing}}{b \cdot (1+\lambda)} \cdot \left[1 - \frac{2 \cdot z}{b} \cdot (1 - \lambda)\right], \text{ with } 0 \leq z \leq b/2 \tag{25}$$

The approximated spanwise lift distribution for a general untwisted wing is then the local average of the two distributions:

$$\bar{L}_{\,half\_wing}(z) = \frac{1}{2} \cdot [L^T_{wing}(z) + L^E_{wing}(z)], \text{ with } 0 \leq z \leq b/2 \tag{26}$$

$$\boldsymbol{\bar{L}_{\,half\_wing}(z) = \frac{1}{2} \cdot \left[\frac{2 \cdot L_{wing}}{b \cdot (1+\lambda)} \cdot \left[1 - \frac{2 \cdot z}{b} \cdot (1 - \lambda)\right] + \frac{4 \cdot L_{wing}}{\pi \cdot b} \sqrt{1 - \left(\frac{2 \cdot z}{b}\right)^2}\right]}, \text{ with } \boldsymbol{0 \leq z \leq b/2} \tag{27}$$

It should be noted that [23] points out that the SCHRENK's method does not provide trustworthy estimates of the spanwise lift distribution for highly swept wings. In that case, a panel method approach or a computational method is necessary. Also, as mentioned, this method does not take into account the case of wings with twist.

The present wing has no sweep but does have twist.

The twist on a wing shifts the Lift resultant towards a location nearer to the wing root therefore reducing maximum wing stresses. Disregarding the wing twist corresponds to a conservative approximation since it results in an overload in the wing tip, with a consequent increase on the local shear force and bending moment at the wing-fuselage joints.

From a structural optimization point of view it is not ideal to make this approximation, nor any in general, however by allowing this approximation to stand, the structure will also be over dimensioned for the second loading situation – asymmetric maneuvers – further increasing the reliability of the designed structure to withstand any loads within the flight envelope. It will therefore, not only be acceptable but also "useful" to determine the wing lift distribution with the SCHRENK method.

Wing Lift Calculation

$n_{design} = SF_{loads} \cdot n_{limit} = SF_{loads\_standard} \cdot SF_{loads\_composites} \cdot n_{limit} = 1.5 \cdot 1.5 \cdot 4 = 9$

$MTOW = 145\ [kg]; \qquad g = 9.81\ [m/s^2]; \qquad b = 6.5\ [m]; \qquad \lambda = \frac{C_{tip}}{C_{root}} = \frac{0.578}{0.722} \approx 0.8$

$L_{wing} \approx n_{design} \cdot W_{aircraft} = n_{design} \cdot MTOW \cdot g = 9 \cdot 145 \cdot 9.81 = \mathbf{12802.1}\ [\boldsymbol{N}]$

$\bar{L}_{half-wing}(z) = \frac{1}{2} \cdot \left[\frac{2 \cdot L_{wing}}{b \cdot (1+\lambda)} \cdot \left[1 - \frac{2 \cdot z}{b} \cdot (1-\lambda)\right] + \frac{4 \cdot L_{wing}}{\pi \cdot b} \sqrt{1 - \left(\frac{2 \cdot z}{b}\right)^2}\right]$, with $0 \leq z \leq b/2$

$\boldsymbol{\bar{L}_{half-wing}(z) = 1253.86 \cdot \left[\sqrt{-0.094675 \cdot (z^2 - 10.5625)} - 0.053537 \cdot (z - 16.2951)\right]}$ $[\boldsymbol{N}]$, with $\boldsymbol{0 \leq z \leq 3.25}$ $[\boldsymbol{m}]$

See Figure 16:

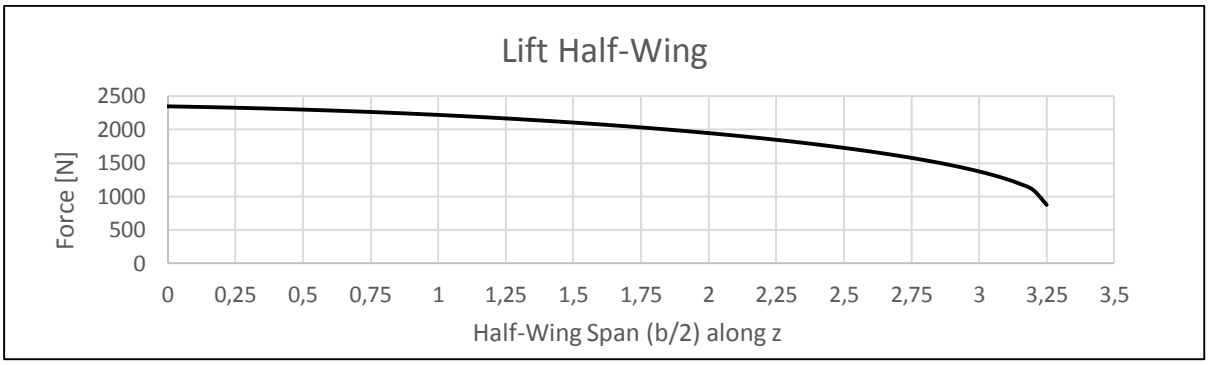

Figure 16 - Lift distribution on half-wing.

$\boldsymbol{L_{half\_wing}} = \int_0^{3.250} \bar{L}_{half\_wing}(z)\, \mathrm{dz} = \boldsymbol{6401.05}$ $[\boldsymbol{N}]$.

As explained is section 3.1.1, for an airfoil, the lift forces acting on the center of pressure (CP) are usually replaced by lift at the aerodynamic center (AC) plus a constant pitching moment M_0, also called M_{ac} or $M_{0.25c}$ since the AC is normally located at about 0.25 of the airfoil's chord (measured from the leading edge) [18]**.**

For simulation purposes, Lift will be applied to the structure along the caps of the main spar, which will be located at $0.28 \cdot chord_{local}$ (explanation, further ahead, in section 4.3.1). Therefore, the associated wing pitching moment ($M_{0.28c}$) will have to be determine.

Wing Pitching Moment

The generic equation for the wing pitching moment is given by:

$$M = C_M \cdot q \cdot S \cdot \bar{c} \tag{28}$$

At the aerodynamic center (AC) of the wing M is given by:

$$M_{ac} = C_{M_{ac}} \cdot q \cdot S \cdot MAC = M_0\ (constant) \tag{29}$$

Where, $C_{M_{ac}}$ is the wing pitching moment coefficient given by the pitching moment (C_m) of the airfoil positioned at y_{MAC}; and MAC is the mean aerodynamic chord. The value for C_m can be obtained from the airfoil's $C_m\ vs\ \alpha$ curve [18].

Aerodynamic Center

c is the chord for airfoils; $\bar{c}$ is the reference chord length for a wing.

"(…) Just as the aerodynamic center for airfoils is normally located at about 0.25 c, for wings the aerodynamic center is located approximately at 0.25 of the mean aerodynamic chord (MAC)" [18]**.** For Mach numbers below $Mach_{critical}$ (transition to supersonic flight), $x_{ac} = 0.25 \cdot \bar{c} = 0.25 \cdot MAC$. For untampered or linearly tapered wings, the spanwise location of the MAC is given by:

$$y_{MAC} = \frac{b}{6} \cdot \frac{1 + 2\lambda}{1 + \lambda} \tag{30}$$

Where λ is the wing tapper ratio: $\lambda = \frac{c_{tip}}{c_{root}}$" [18].

Mean Aerodynamic Chord (MAC)

"For untampered wings, the wing chord length is used as the reference chord length $\bar{c}$ in the expression for moment coefficient. For tapered wings, a simple average chord length is sometimes used. The most commonly used value for $\bar{c}$ is known as the mean aerodynamic chord (MAC). The MAC is a weighted average chord defined by the expression:

$$MAC = \frac{1}{S} \int_{-b/2}^{b/2} c^2 \, dy \tag{31}$$

For linearly tapered wings, simplifies to: $MAC = \frac{2}{3} \cdot c_{root} \cdot \frac{1+\lambda+\lambda^2}{1+\lambda}$" [18].

Wing Pitching Moment Distribution

As mentioned, it was decided to apply the lift force along the main spar caps which are located at $0.28 \cdot \bar{c} = 0.28 \cdot MAC$. Therefore, is necessary to determine the equivalent pitching moment for that location.

The equivalent pitching moment value for $x_{0.28 \cdot MAC}$ and y_{MAC} can be obtained by:

$$M_{0.28 \cdot MAC} = M_{ac} + 0.03 \cdot MAC \cdot L_{wing} \tag{32}$$

Nevertheless, what is wanted is the distribution of that moment across the wing span.

$$M(z) = Distance(z) \cdot Force(z) \tag{33}$$

Where, Distance and Force are orthogonal. Note: $L_{wing}(z)$ has a direction orthogonal to the direction of flight so the distance between AC ($0.25 \cdot c$) and $0.28 \cdot c$ (in other words, $0.03 \cdot c$) has to be transformed in its component, orthogonal to the lift direction.

$$M_{0.28 \cdot c}(z) = -[|M_{0.25 \cdot c}(z)| + 0.03 \cdot c(z) \cdot \cos(\alpha'(z)) \cdot L_{wing}(z)] \tag{34}$$

Where $c(z)$ is the wing chord along the wing span, Equation (16).

Where $\alpha'(z)$ is the wing's twist angle + angle of attack (measured at the wing tip), along the wing span:

$$\alpha'(z) = \alpha_{twist}(z) + \alpha = \alpha_{twist} \cdot \left(1 - \frac{2}{b} \cdot z\right) + \alpha_{tip} \text{ , with } 0 \leq z \leq b/2 \tag{35}$$

Where $M_{0.25 \cdot c}(z)$ is the pitching moment in the aerodynamic center (AC) of each airfoil along z:

$$M_{0.25 \cdot c}(z) = -d(z) \cdot \cos(\alpha'(z)) \cdot L_{wing}(z) \tag{36}$$

Where, d is the distance between CP and AC measured along the airfoil's chord. It should be noted that $M_{0.25 \cdot c}$ would remain constant along z if the airfoil was kept constant. However, since the airfoil suffers a decrease in size, it will be assumed that $M_{0.25 \cdot c}$ might suffer some change along z. Therefore, the equation for d will be determined based on the wing geometry and on the $\frac{C_m}{C_l}$ graph of the airfoil:

Wing Geometry: For a trapezoidal wing with constant tapper and twist.

From the generic equation for a straight line: $y(x) = y_{initial} \pm \frac{y_{final} - y_{initial}}{x_{final} - x_{initial}} \cdot (x - x_{initial})$:

$$d(z) = d_{root} \cdot \left[1 - \frac{2 \cdot z}{b} \cdot \left(1 - \frac{d_{tip}}{d_{root}}\right)\right] \tag{37}$$

From the moment equation (24):

$$d_{root} = \left|\frac{m_{root}}{l_{root}}\right| = \left|\frac{C_m \cdot q \cdot S \cdot c_{root}}{C_l \cdot q \cdot S}\right| = \left|\frac{C_m(\alpha'(z=0))}{C_l(\alpha'(z=0))}\right| \cdot c_{root} = \left|\frac{C_m(\alpha_{twist} + \alpha_{tip})}{C_l(\alpha_{twist} + \alpha_{tip})}\right| \cdot c_{root} \tag{38}$$

Where, C_m is the moment coefficient for the airfoil, C_l is the lift coefficient for the airfoil and c_{root} is the chord of the airfoil at the root of the wing. [18]

$$d_{tip} = \left|\frac{C_m(\alpha'(z=b/2))}{C_l(\alpha'(z=b/2))}\right| \cdot c_{tip} = \left|\frac{C_m(\alpha)}{C_l(\alpha)}\right| \cdot c_{tip} \tag{39}$$

Where, c_{tip} is the chord of the airfoil at the tip of the wing. C_m and C_l can be obtained from the airfoil's graphs C_m *vs* α and C_l *vs* α, respectively.

Resulting in:

$$M_{0.28 \cdot c}(z) = -L_{wing}(z) \cdot \cos\big(\alpha'(z)\big) \cdot \big(d(z) + 0.03 \cdot c(z)\big) \text{ , with } 0 \le z \le b/2 \tag{40}$$

$$\boldsymbol{M_{0.28 \cdot c_{half\_wing}}(z) = -\frac{1}{2} \cdot \left[\frac{2 \cdot L_{wing}}{b \cdot (1+\lambda)} \cdot \left[1 - \frac{2 \cdot z}{b} \cdot (1-\lambda)\right] + \frac{4 \cdot L_{wing}}{\pi \cdot b} \sqrt{1 - \left(\frac{2 \cdot z}{b}\right)^2}\right]}$$
$$\boldsymbol{\cdot \cos\left(\alpha_{twist} \cdot \left(1 - \frac{2}{b} \cdot z\right) + \alpha_{tip}\right) \cdot \left[d_{root} \cdot \left[1 - \frac{2 \cdot z}{b} \cdot \left(1 - \frac{d_{tip}}{d_{root}}\right)\right] + 0.03 \cdot c_{root} \cdot \left[1 - \frac{2 \cdot z}{b} \cdot \left(1 - \frac{c_{tip}}{c_{root}}\right)\right]\right]}, \text{ with } 0 \le z \le b/2 \tag{41}$$

Wing Pitching Moment Calculation

$L_{wing} \approx 12802.1\ [N]$; $n_{design} = 9$; $MTOW = 145\ [kg]$; $g = 9.81\ [m/s^2]$; $b = 6.5\ [m]$

$\lambda = \frac{c_{tip}}{c_{root}} = \frac{0.578}{0.722} \approx 0.8$; $V_e = 96.42\ [m/s]$; $S_{wing} = 4.225\ [m^2]$; $CL_{\alpha_{wing}} = 0.087/º$; $\alpha_{wing_{twist}} = 4.4º$

$\alpha_{wing_{tip}} = \frac{L_{wing}}{\frac{1}{2} \cdot \rho \cdot V^2 \cdot S_{wing} \cdot C_{L_{\alpha_{wing}}}} \approx \frac{n_{design} \cdot MTOW}{\frac{1}{2} \rho_{sl} \cdot {V_e}^2 \cdot S_{wing} \cdot C_{L_{\alpha_{wing}}}} = \frac{9 \cdot 145 \cdot 9.81}{\frac{1}{2} 1.225 \cdot 96.42^2 \cdot 4.225 \cdot 0.087} \approx 6.1º$

For Standard Sea Level (SSL):

$Temperature\ of\ fluid: T = 288.15\ [K]$ (15 [ºC])

$Velocity\ of\ fluid\ (air): V = V_e = 96.42\ [m/s]$

$Kinematic\ viscosity\ of\ fluid\ (air): v_{sl} = 1.460 \times 10^{-5} [m^2/s]$

→ $Re = \frac{V \cdot c_{root}}{v} = 4{,}768{,}167$ and $Re = \frac{V \cdot c_{tip}}{v} = 3{,}817{,}175$

Airfoil: SELIG S4110 → C_m *vs* α and C_l *vs* α plots for $Re = 1{,}000{,}000$ (highest Re # plot available) [22]. See Annex 2.

$d_{root} = \left|\frac{C_m(\alpha=10.5)}{C_l(\alpha=10.5)}\right| \cdot c_{root} = \left|\frac{-0.069}{1.441}\right| \cdot 0.722 = 0.034572\ [m]$

$d_{tip} = \left|\frac{C_m(\alpha=6.1)}{C_l(\alpha=6.1)}\right| \cdot c_{tip} = \left|\frac{-0.08}{1.044}\right| \cdot 0.578 = 0.044291\ [m]$

$$M_{0.28\cdot c_{half\_wing}}(z) = -\frac{1}{2}\cdot\left[\frac{2\cdot L_{wing}}{b\cdot(1+\lambda)}\cdot\left[1-\frac{2\cdot z}{b}\cdot(1-\lambda)\right]+\frac{4\cdot L_{wing}}{\pi\cdot b}\sqrt{1-\left(\frac{2\cdot z}{b}\right)^2}\right]\cdot\cos\left(\alpha_{twist}\cdot\left(1-\frac{2}{b}\cdot z\right)+\alpha_{tip}\right)\cdot\left[d_{root}\cdot\left[1-\frac{2\cdot z}{b}\cdot\left(1-\frac{d_{tip}}{d_{root}}\right)\right]+0.03\cdot c_{root}\cdot\left[1-\frac{2\cdot z}{b}\cdot\left(1-\frac{c_{tip}}{c_{root}}\right)\right]\right],\ \text{with}\ 0\le z\le b/2$$

$$\boldsymbol{M_{0.28\cdot c_{half-wing}}(z) = -2.08295\cdot(z+33.8496)\cdot\left(\sqrt{-0.094675\cdot(z^2-10.5625)}-0.053537\cdot(z-16.2951)\right)\cdot cos\left(1.35385\cdot(z-7.75568)\right)\ [N\cdot m],\ \text{with}\ 0\le z\le 3.25}$$

$$\boldsymbol{|M_{0.28\cdot c_{half-wing}}|} = \int_0^{3.250} M_{0.28\cdot c}(z)\ \mathrm{dz} = \boldsymbol{371.411\ [N\cdot m]}$$

See Figure 17:

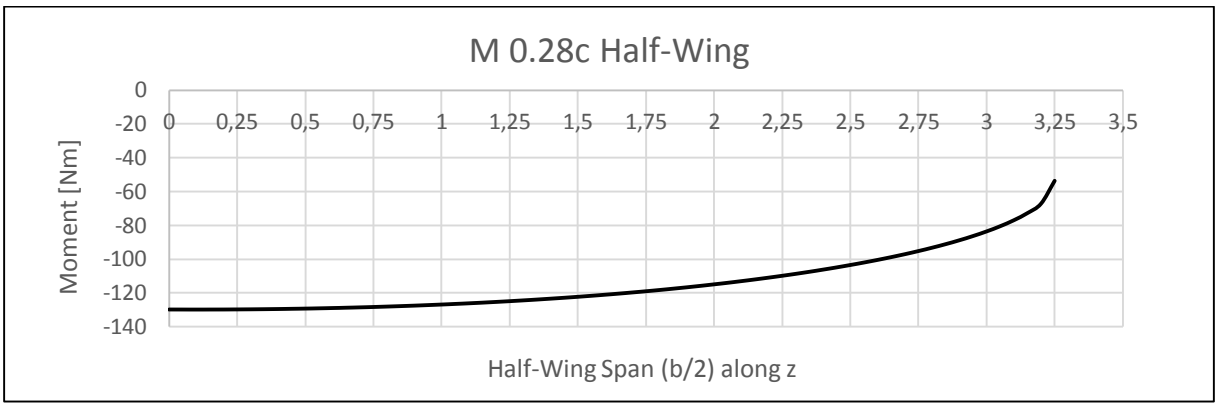

Figure 17 - Pitching moment at 0.28 chord, caused by Lift.

Weight and Inertial Loads

Wing Structure Weight and Inertial Force

$$W_{wing\_structure} = g\cdot m_{wing\_structure} \tag{42}$$

$$F_{inertial_{wing\_structure}} = (n-1)\cdot g\cdot m_{wing\_structure} \tag{43}$$

Weight and Inertial Force Distribution

Initial Wing Geometry: Trapezoidal Wing with constant taper and twist; Constant thickness of structural components; Ribs equally spaced along the wing.

$$W_{wing\_structure}(z) \approx \frac{2\cdot W_{wing}}{b\cdot(1+\lambda)}\cdot\left[1-\frac{2\cdot z}{b}\cdot(1-\lambda)\right] \tag{44}$$

$$F_{inertial_{wing\_structure}}(z) \approx (\mathrm{n}-1)\cdot\frac{2\cdot W_{wing}}{b\cdot(1+\lambda)}\cdot\left[1-\frac{2\cdot z}{b}\cdot(1-\lambda)\right] \tag{45}$$

$$W_{half-wing} = \frac{W_{wing\_structure}}{2} \approx \frac{2\cdot W_{wing}}{b\cdot(1+\lambda)}\cdot\left[1-\frac{2\cdot z}{b}\cdot(1-\lambda)\right],\ \text{with}\ 0\le z\le b/2 \tag{46}$$

$$F_{inertial_{half-wing}} = (n-1)\cdot\frac{W_{wing\_structure}}{2} \approx \frac{(n-1)\cdot 2\cdot W_{wing}}{b\cdot(1+\lambda)}\cdot\left[1-\frac{2\cdot z}{b}\cdot(1-\lambda)\right],\ \text{with}\ 0\le z\le b/2 \tag{47}$$

Because, for the flight condition in study, both the weight and the inertial force have equal distributions and their force vectors are coincident, a *total body force* (BF) can be used instead:

$$BF_{wing\_structure} = n \cdot W_{wing\_structure} \tag{48}$$

$$BF_{half-wing} = n \cdot \frac{W_{wing\_structure}}{2} \approx \frac{n \cdot 2 \cdot W_{wing}}{b \cdot (1+\lambda)} \cdot \left[1 - \frac{2 \cdot z}{b} \cdot (1-\lambda)\right], \text{ with } 0 \leq z \leq b/2 \tag{49}$$

Weight and Inertial Force Calculation

As initial condition, it will be considered that $W_{wing\_structure} = W_{wing\_estimated_{UAVision}} = m_{wing\_estimated} \cdot g = \mathbf{26.2} \cdot 9.81 = 257.022\ [N]$ (weight of the full wing span (b)).

Since one of the objectives of this work is to lower the structural weight of the conceptual design, this assumption is considered conservative.

$n_{design} = 9$; $BF_{half-wing} = n_{design} \cdot \frac{W_{wing\_structure}}{2} = 1156.6\ [N]$; $b = 6.5\ [m]$; $\lambda = \frac{C_{tip}}{C_{root}} = \frac{0.578}{0.722} \approx 0.8$

$BF_{half-wing}(z) \approx \frac{n_{design} \cdot 2 \cdot W_{wing}}{b \cdot (1+\lambda)} \cdot \left[1 - \frac{2 \cdot z}{b} \cdot (1-\lambda)\right]$, with $0 \leq z \leq b/2$

$BF_{half-wing}(z) = -24.2586 \cdot (z - 16.2951)$, with $0 \leq z \leq 3.25$

$BF_{half-wing} = \int_0^{3.250} F_{inertial_{half\_wing}}(z)\ \mathrm{dz} = 1156.6\ [N]$ (Proof)

For the design condition:

$Angle\ of\ attack$: $\alpha = \alpha_{tip} = 6.1º$

$Wing\ geometric\ dihedral\ angle$: $\Gamma = 2º$

$BF_{perpendicular_{half-wing}}(z) = BF_{half-wing}(z) \cdot \cos(\alpha) \cdot \cos(\Gamma)$

$\boldsymbol{BF_{perpendicular_{half-wing}}(z) = -24.2586 \cdot (z - 16.2951) \cdot cos(6.1) \cdot cos(2)}$, with $\mathbf{0 \leq z \leq 3.25}$

$\boldsymbol{BF_{perpendicular_{half-wing}} = \int_0^{3.250} BF_{perpendicular_{half-wing}}(z)\ \mathrm{dz} = 1149.35\ [N]}$

See Figure 18:

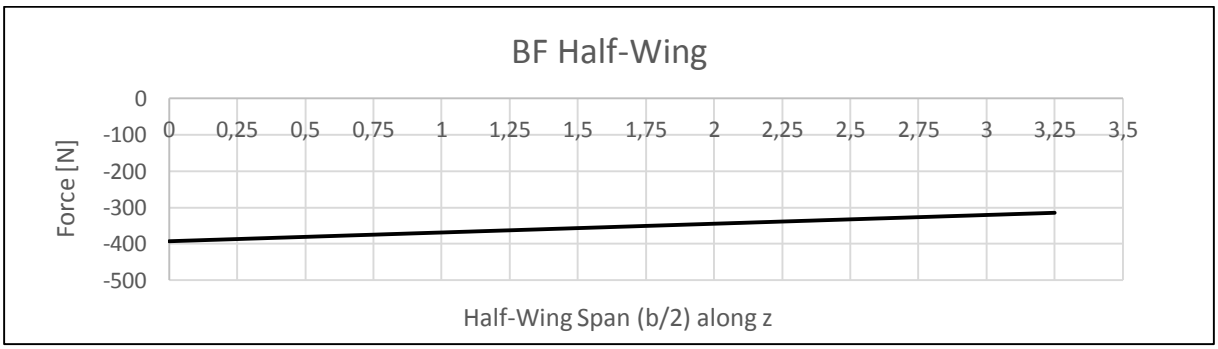

Figure 18 - Body Forces acting perpendicularly to the half-wing.

Wing Additional Masses Weight and Inertial Loads

Additional masses attached to the wing structure are: the wing payload and the two servo motors needed to actuate the ailerons and flaps (one for each). Their masses are 10, 0.2 and 0.2 [kg], respectively.

The payload mass was imposed by operational requirements. The servo motors mass was estimated based on the size of the wing and the force required to actuate its aerodynamic surfaces. From statistical data, servos with a force of 5 [kg · mm] have a mass $<$ 0.2 [kg]. The approximation is therefore conservative.

These masses will create point loads which are a combination of weight and inertial force. Because the application points and force vectors are coincident (for each body) the resulting body forces can be given by:

$$\boldsymbol{BF_{payload} = n \cdot W_{payload}} \quad (50)$$

$$\boldsymbol{BF_{motor\_1} = n \cdot W_{motor\_1}} \quad (51)$$

$$\boldsymbol{BF_{motor\_2} = n \cdot W_{motor\_2}} \quad (52)$$

Additional Masses Location

The body force caused by each mass will be applied on the structure, on its respective attachment points.

Regarding the payload, the decision was made to place it near the wing root. The reason being, that the root is expected to be the most reinforced location of the wing. Also, the decision took into consideration that, although placing an additional point mass nearer the wing tip does reduce the total deflection caused by the lift and, consequently, a decrease in the maximum stresses at the wing root, it also significantly decreases the wings structural life because of the increase in fatigue damage, as concluded by [34].

It was decided to place the payload body force on the wing surface (skin) at $z = 0.240\ [m]$ - approximate medium location between the root and the beginning of the flap - and at approximately half of the local chord. The force was distributed by the 12 holes of 5 [mm] diameter, each, simulating the bolted connection between the payload and the wing skin.

The body forces of the servo motors for the flap and aileron were placed on the wing skin at $z = 1.13437\ [m]$ and $z = 2.43957[m]$ respectively – center position of each aerodynamic surface – and at half-way between the main spar and the second spar locations. For each, the force was distributed by the 8 holes of 5 [mm] diameter, each, simulating the bolted connection between the motor supports and the wing skin. Also, cut-outs were made in the skin for each motor to be able to be installed inside the wing.

Additional Masses Forces Calculation

$BF_{payload} = n_{design} \cdot W_{payload} = 9 \cdot 10 \cdot 9.81 = 882.9\ [N]$

$BF_{motor\_1} = n_{design} \cdot W_{motor\_1} = 9 \cdot 0.2 \cdot 9.81 = 17.658\ [N]$

$BF_{motor\_2} = n_{design} \cdot W_{motor\_2} = 9 \cdot 0.2 \cdot 9.81 = 17.658\ [N]$

For the design condition:

$Angle\ of\ attack$: $\alpha = \alpha_{tip} = 6.1º$

$Wing\ geometric\ dihedral\ angle$: $\Gamma = 2º$

$BF_{payload\_perpendicular} = F_{inertial\_payload} \cdot \cos(\alpha) \cdot \cos(\Gamma) = 882.9 \cdot \cos(6.1) \cdot \cos(2) = \boldsymbol{877.366}[\boldsymbol{N}]$

$BF_{motor\_1\_perpendicular} = 17.658 \cdot \cos(6.1) \cdot \cos(2) = \boldsymbol{17.5473}\ [\boldsymbol{N}]$

$BF_{\text{motor } 2\_perpendicular} = 17.658 \cdot \cos(6.1) \cdot \cos(2) = \boldsymbol{17.5473}\ [\boldsymbol{N}]$

4 Wing Structural Design

Before the structure is designed it is a good practice to define which materials may be used because materials influence the design and the design influences how and what materials can be used.

4.1 Materials

Nowadays, aircraft designers have a variety of high performance materials to choose from [18].

The selection of the structural material for an aircraft is influenced by several factors, but amongst these, strength and lightness are probably the most important. Other properties that may also have critical significance are stiffness, toughness, resistance to corrosion, fatigue and the effects of environmental heating, ease of fabrication, availability and consistency of supply and, last but not least important, cost [24].

"The goal is to produce a structure that has sufficient strength and stiffness for a minimal weight, cost, and manufacturing effort. Two of the parameters to be considered when selecting materials, therefore, are strength-to-weight ratio $\sigma_u/(\rho \cdot g)$ and stiffness-to-weight ratio $E/(\rho \cdot g)$. These two parameters are often referred to as structural efficiency" [18]. In a wing structure design, stiffness is particularly important because wings with high amplitude oscillations will be more susceptible to aero elastic effects, such as flutter, that can cause premature failure of the structure.

"The main groups of materials used in aircraft construction have been wood, steel, aluminum alloys, (…) titanium alloys, and fiber-reinforced composites" [24]. From these, Graphite/Epoxy composites are the ones with the highest structural performance (best structural efficiency) [18].

4.1.1 Composite materials

Composite materials are those that, on a macroscopic scale, are formed by the combination of two or more distinct materials that are not soluble in each other. The combination of these materials results in a composite material with superior properties than of its constituents. In its most basic form, composite materials are constituted by two parts: the reinforcement and the matrix [35] [36] [37].

The reinforcement is responsible for resisting to the loads applied to the material while the matrix is responsible for transmitting the loads between reinforcements via shear stresses. The matrix is also responsible for maintaining the reinforcement's shape and integrity as well as protect it from exposure to damaging elements [35] [36] [37]. In aeronautic applications, the matrix is usually a polymer and the reinforcement is usually non-metallic, more specifically, glass, carbon or aramid (Kevlar) [37] [38].

Depending on the geometry of the reinforcement, composite materials can be classified as: Fiber reinforced composite materials, where fibers can be continuous or discontinuous and, regarding their orientations, they can be: random, unidirectional, bidirectional or multidirectional [36] [39]; or Particle reinforced composite materials.

The fiber reinforced composites are usually created by stacking two or more layers of reinforcement that can have been previously impregnated with the matrix (*Prepreg*) or are impregnated during the stacking procedure (*Hand-lay-up*). The stacking procedure is called *lamination* and each layer is also called a *ply*. After lamination is complete, the matrix is cured (hardened) either by leaving it exposed to

atmospheric conditions or under controlled temperature, humidity and pressure conditions, depending on the matrix material and the mechanical properties that one wishes to obtain.

Unidirectional fiber reinforced laminate composites have higher mechanical strength and higher elastic modulus (E) (high stiffness) in the fiber's direction whilst on the orthogonal direction those values are much lower [35] [37]. In order to obtain specific values for those properties, it is possible to define a specific laminate configuration with different ply orientations and thicknesses with a well-defined stacking sequence. This allows for the creation of bidirectional or multidirectional materials. It should be noticed that a material whose properties depend on the material's orientation (fibers orientation) are called anisotropic [24].

For materials whose manufacturing processes consist of stacking plies, a phenomenon called delamination can occur. It consists of a failure of the bond between the plies and occurs where shear stresses between plies are maximum, for example, on a laminate's edges and corners. Several factors can negatively contribute to delamination but the major is the incompatibility between the material properties of two consecutive plies [35] [37]. A common example is the delamination resulting from cutting or drilling into laminate materials. This will be further explained in section 4.5.1.2.

For fiber reinforced laminate composites, in addition to delamination between plies, incompatibility between the fibers and the matrix may also occur. A weak bond between them may lead to material failure in the form of: fiber breakage, fiber bucking or "delamination" [35] [37].

The high susceptibility to failure displayed by composite materials, specially by the fiber reinforced laminate ones, has lead designers to use much higher safety factors for composites (in general) than for metals [18] (see section 3.2.1.1).

4.2 Solid Mechanics

Solid mechanics or mechanics of materials is the study of the physics' laws that govern how solid objects resist or support loads applied to it [18].

4.2.1 Stress, Strain and Poisson's ratio

Stress (σ) is the force (F) per unit area (A). It can be described as the forces (strength) between the molecules within a solid:

$$\sigma = \frac{F}{A} \text{ [Pa] or [N/m}^2\text{] (SI)} \tag{53}$$

Strain (ε) is the change (variation) of a solid's dimension in a given direction ($\Delta l = l - l_0$), divided by the initial value (l_0):

$$\varepsilon \equiv \frac{\Delta l}{l_0} \tag{54}$$

Poisson's ratio (ν) is the relation between transverse and longitudinal strain (when a load is applied in the axial direction). It is characteristic of each material. It is given by:

$$\nu = -\frac{\varepsilon_{transverse}}{\varepsilon_{longitudinal}} \tag{55}$$

4.2.2 Stress-Strain Relation: Hook's Law

In the elastic domain, each material has a specific relationship between the stress applied to it and the amount of strain it exhibits. The relationship is given as:

$$\varepsilon = \frac{\sigma}{E} \tag{56}$$

Where E is a constant called *Modulus of elasticity* also known as *Young's modulus*, characteristic of each material.

Hooke's law for a structure loaded in compression is the same as for tensile loads. For shear, however, a different form of the law is used: $$\gamma = \frac{\tau}{G} \quad (57)$$

Where γ is the shear strain, τ is the shear stress and G is the Young's modulus for shear, also called the *modulus of rigidity* [18].

4.2.3 Plastic Deformation

Plastic deformation consists in the permanent change of a solids shape due to an applied force strong enough to rearrange its material's molecules [18].

"Plastic deformation of an aircraft structure can seriously affect its ability to function properly. The maximum structural limits on aircraft are always set to avoid plastic deformation of the structure. The stress beyond which a material will undergo plastic deformation is called its *yield strength* (σ_y), and the load limit for a structure beyond which it will be permanently deformed is called *yield limit*" [18]. See Figure 19.

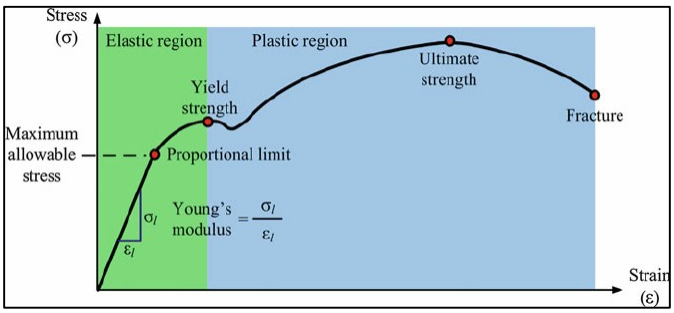

Figure 19 – Stress – Strain curve for a ductile material [40].

The very strong fibers present in composite materials prevent them from yielding significantly before the fibers break and the materials fail [18]. See Figure 20.

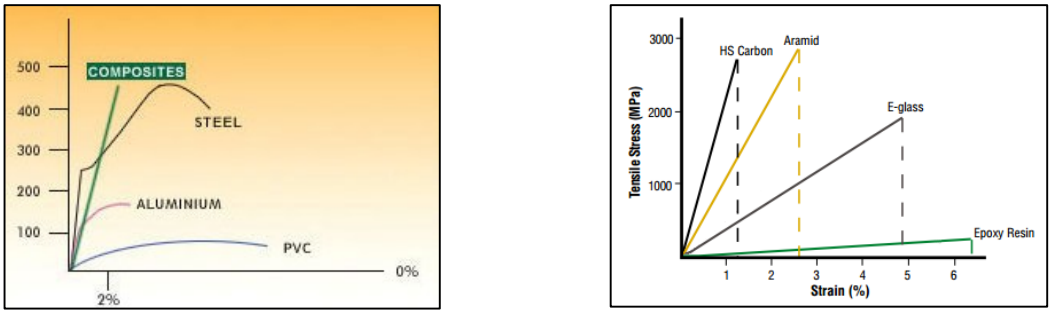

a) b)

Figure 20 – a) Comparison between the Stress-Strain curves of different materials [41]; b) Stress-Strain curves for different fibers and for epoxy resin, allowing to compare typical stress and strain failure values [42].

4.2.4 Failure

Very strong forces applied to a solid might cause some molecules to move so far from their neighbors that the intermolecular forces between them disappear and the object develops cracks or even breaks apart. This situation is called *structural failure*. "Failure of an aircraft structure frequently results in complete destruction of the aircraft" [18].

4.2.5 Fatigue

"Many materials, especially metals, will develop cracks and eventually fail after many cycles of having loads applied and removed without ever being stressed beyond their ultimate strength. This process of developing cracks due to cyclic loading is called *fatigue*" [18].

Fatigue life is the "relationship between maximum loads and the number of cycles a material can endure before developing fatigue cracks" [18]. *Fatigue limits* are the "stress levels below which the materials will not develop cracks no matter how many cycles of loading they undergo" [18].

4.3 Wing Structural Components and Considerations

The pressure and shear distributions on a wing are applied to the *skin*, collected by the *ribs* and transmitted to the *spars*. Wing skins are usually quite thin, and so they frequently have additional stiffeners or *stringers* attached to them that help transmit the skin surface loads through the ribs to the spars [18].

The combined action of skin, stringers and spars enables a wing to resist bending loads [24] [18].

Skin, ribs and spars form tubes and boxes that resist wing twisting or torsion. This resistance is mainly due to shear stresses developed in the skin and spar webs [18].

Concentrated loads (point loads) are usually applied to the ribs or directly to the spars [24].

4.3.1 Spars

Spars are the main load-bearing members in the wing. They are strong beams that run spanwise in the wing and carry the force and moments [18].

Spar webs are subjected to both vertical shear, resulting from vertical loads, and horizontal shear, caused by compression at the top of the spar and tension at the bottom. "Stresses on the spar webs (mostly shear) are relatively small compared to the stresses in the spar caps" (tensile and compressive) [18] and so the webs can be much thinner than the caps. "Because spar webs must primarily carry shear stresses, if made of composite materials, they should have their fibers in a mesh or with multiple layers in which each layer has fibers oriented 90º or 45º relative to fibers in adjacent layers" [18].

The positioning of the main spar (1st Spar) in the wing should be, ideally, where torsional moments are minimum [43]. Torsion deforms the cross-section of the spar (beam), decreasing its *area moment of inertia* (I) and consequently diminishing its effectiveness to resist bending loads.

As mentioned previously in section 3.1.1, torsional moments are zero for the center of pressure (CP) which, does not have a fixed position [43]. The design solution that is usually adopted is to place the main spar where its area moment of inertia can be maximized and not so far from the CP that torsional moments might become too big of a problem. That location is where the airfoil thickness is highest (usually between 0.3-0.35c – measured from the leading edge) [43]. In this specific case, the airfoil thickness is highest for 0.28c which is only a little further behind the aerodynamic center (0.25c).

The positioning of the secondary spar (2nd Spar) in the wing should be, ideally, as close as possible to the hinge axis of the trailing edge devices (flaps and ailerons) in order to better resist their bending and torsion loads. Nevertheless, its geometry and placement should be such as to still allow for the full range of motion of the devices.

4.3.2 Ribs

Besides transmitting the pressure and shear from the skin to the spars, ribs also distribute concentrated loads (e.g. additional wing payload loads) into the structure and redistribute stresses around discontinuities in the wing surface (e.g. inspection panels) [24].

Furthermore, one of the main functions of the ribs is to maintain the shape of the wing cross-section for all combinations of load by increasing its rigidity [24].

"Ribs increase the rigidity of the wing by increasing the column buckling stress of the skin and longitudinal stiffeners by providing end restraint and establishing their column length" [24]. Higher buckling stresses mean that the wing can withstand higher compression forces without deforming and therefore, the overall rigidity of the wing towards bending loads will increase since they cause, simultaneously, tension and compression on opposite sides of the wing.

"The dimensions of the ribs are governed by their spanwise position in the wing and by the loads they are required to support" [24].

4.3.3 Skin

"The primary function of the wing skin is to form an impermeable surface for supporting the aerodynamic pressure distribution from which the lifting capability of the wing is derived. These aerodynamic forces are transmitted in turn to the ribs and stringers" [24].

4.3.4 Stringers

As mentioned before, stringers are skin stiffeners. They are placed on the inside-fuselage-surface of the skin and are oriented in the wing's longitudinal direction.

They allow for a substantial increase in the skins longitudinal rigidity (increase the longitudinal buckling failing stresses) with minimal weight addition. In fact, far less weight than if the same rigidity would to be achieved by increasing the skin thickness.

4.3.5 Other Skin Stiffening Methods

As pointed out before, another skin stiffening method is to increase the skin thickness as it increases its area moment of inertia (I). This can be accomplished by either adding more of the same material or by introducing a lighter material in its core.

Introducing a ply of material in the middle of two plies of another material is called *sandwich laminate material configuration*. By using a light but rigid material as the core of the laminate, it enables to significantly increase the skin rigidity in both longitudinal and transverse directions with minimal weight addition [44]. See Figures 21 and 22.

Another skin stiffening method involves changing the skin shape by either changing the geometry of the whole skin or only a few layers of material (usually the core layers). For example, changing the geometry from *plain* to *wavy (corrugated)*, increases I considerably without any variation in weight. Another example is the use of "honeycomb" cores which can be made of either the same or different material than the skin [44]. See Figures 21 and 22 and 23.

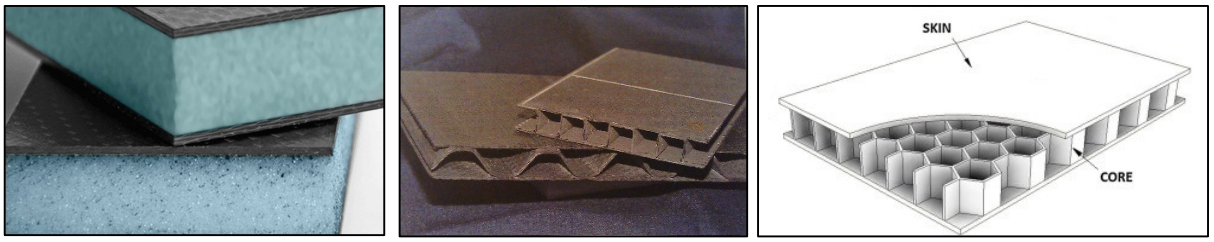

a) b) c)

Figure 21 – a) Foam core; b) Corrugated core; c) Honeycomb core [44].

t= thickness	Solid Metal Sheet t = 1" of metal or resin 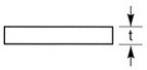	Sandwich Construction t = 1" of metal or resin PLUS 1" of honeycomb 	Thicker Sandwich t = 1" of metal or resin PLUS 2" of honeycomb 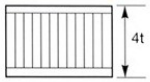
Relative Stiffness	100	700 7 times more rigid	3700 37 times more rigid
Relative Strength	100	350 35 times as strong	925 9.25 times as strong
Relative Weight	100	103 3% increase in weight	106 6% increase in weight

Figure 22 - Sandwich laminate material advantages [45].

Figure 23 – Detail: corrugated fuselage and wing skins of a Junkers J-52 3M (WWII aircraft) [46].

4.4 Ailerons and Flaps

The ailerons and the flaps are aerodynamic surfaces equivalent to the wing and therefore, the same structural principles apply [24].

From a manufacturing point of view, when it comes to wings for subsonic, low speed UASs with a span inferior to 8 m, experience has demonstrated that building the wing structure as a single block and then cutting out the trailing edge devices (flaps and ailerons), is the best practice in order to ensure their perfect fit and finish.

A simple, durable, light and cost effective solution for attaching those devices to the wing while maintaining good hinge movement is to use strips of *Kevlar* material instead of conventional metallic hinges.

When using the Kevlar method, the strips are put in place, in-between skin layers (plies), during the wing skin construction. When "cutting free" the devices, the Kevlar strips are the only plies which fibers do not break when the resin is bent to that extent. So, after forcing the resin to break, the Kevlar strips gain full freedom of motion and the hinges becomes fully functional. It should be noted that the strips should be placed in a discrete manner and not in a continuous one in order to avoid movement restrictions due to wing twist and bending during flight.

An important remark, concerning the wing's structural components placement, is to ensure that the secondary spar has such a geometry, or is placed in such a manner, that allows for the full range of motion of these trailing edge devices.

Also concerning the wing structure, it should be noticed, that even though flaps and ailerons are part of the wing and their surface areas are responsible for some percentage of the resultant aerodynamic loads acting on the wing, they do not play a significant hole in terms of contributing to the wing's capability

to withstand maximum loads. The non-rigid connection (in this case a Kevlar hinge) between the main wing structure and the flaps or the ailerons is the main reason.

4.5 Wing Design Recommendations and Guidelines

Although every structural design problem is different, there are general guidelines that suggest how to avoid pitfalls and goals to strive for when laying out an aircraft's wing structure:

1. "Never attach anything to the skin alone. Even thick aluminium skin has relatively little strength against point loads perpendicular to its surface. Pylons, landing gear, control surfaces, etc. must be attached through the skin to major structural components (spars, ribs, etc.) within the structure.
2. (…)
3. Major load-bearing members such as spars should carry completely through a structure. Putting unnecessary joints at boundaries of fuselage, nacelles, etc. weakens the structure and adds weight.
4. Whenever possible, attach engines, equipment, landing gear, systems, pylons, etc. to existing structural members. Adding surfaces to beef up attachment points adds weight. Plan the positions of structural members so that as many systems as possible can be attached to them, and so the structures can carry as many different loads as is practical.
5. Design redundancy into your structures so that there are multiple paths for loads to be transmitted. In this way, damage or failure of a structural member will not cause loss of the aircraft.
6. Mount control surfaces and high-lift devices to a spar, not just the rear ends of ribs" [18].
7. Plan carefully the geometry and placement of holes and access panels.
   a) "There is an optimum corner radius for square and rectangular openings as functions of load factors and geometries. For example, a square opening in uniaxial tension parallel to a side should have a corner radius to width ratio between one-fourth and three-eighths.
   b) When multiple openings are required, they should be aligned in the same direction as the major component of the applied load, rather than in an arrangement perpendicular or askew to the load.
   c) When the centers of two openings are located more than two diameters (of the larger openings) apart, consider each as an isolated opening.
   d) When the centers of two circular openings are located between one diameter and two diameters (of the larger) apart and the smaller is between one-fifth and one-tenth the radius of the larger, the reinforcement of the smaller should be increased to 45 percent" [47].
8. "Structural layout is a very creative process. Innovation can often save complexity, weight, and cost" [18].

4.5.1 Holes and Access Panels

Access panels are cut-outs in the wing or fuselage skin that allow for easy access to the internal structure of the aircraft. Their geometry is usually quadrangular or rectangular. They are usually covered with panels of the same material and thickness as the skin.

Holes have a much smaller diameter and can be either drilled or embedded in structural components for bolting purposes or to allow the passage of cables. Their geometry is usually circular.

Embedded holes are usually found in composite materials with continuous fibers and their maximum diameter is usually dependent on the number of fibers per cross-sectional area: the smaller the ratio the larger the hole can be without causing a big distortion of the fibers orientation. See Figure 24.

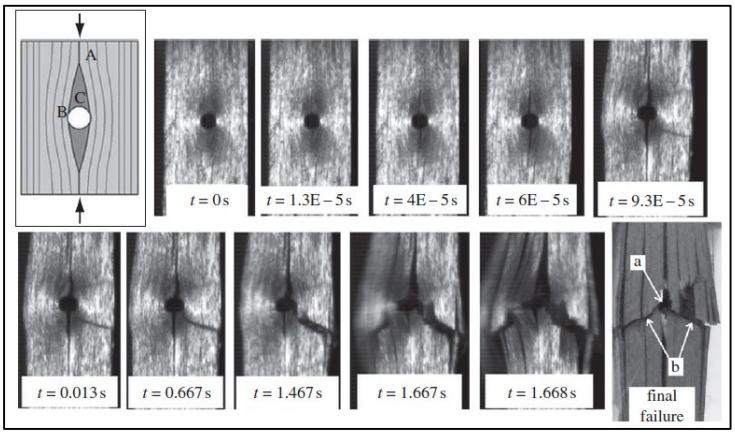

Figure 24 - Axial compression of carbon fiber reinforced polymer (CFRP) with embedded hole [48].

Embedded holes are a good solution for avoiding to cut the fiber strands and consequently decreasing the material's strength. Nevertheless, they should be avoided for materials with only unidirectional fibers because axial compression loads will lead to cracking and failure as concluded by [48]. See Figure 24.

According to the solid mechanic's equation for stress $\sigma = \frac{F}{A}$ (introduced in section 4.2.1), where A is the area transverse to the force F, if a finite plate in one directional tension or compression suffers a removal of material and the force is maintained, the stress in the remaining area will increase - Figure 25.

Because - for the same cut-out cross sectional area - a square geometry has a higher concentration of stresses (higher maximum stress value) in comparison to a circular geometry, its use should be avoided or the edges rounded in order to decrease the local stress concentration. See Figure 25). This was also observed by [47].

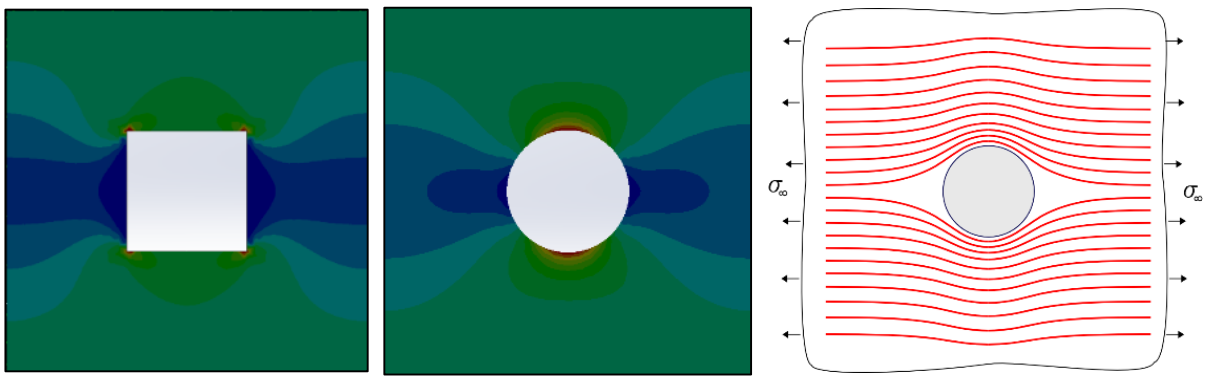

a) b) c)

Figure 25 – a) and b): Finite element analyses (FEA) model for two finite solid plates of equal dimensions and properties. Cut-outs with the same projected cross-sectional area (height of the square is equal to the circle diameter). Boundary conditions: roller/slider constraint for the top, bottom and left outer-surfaces and for the frontal surface; forced horizontal displacement for the right outer-surface. Red indicates highest stress values and blue the lowest. Models show only stress distribution. Strain is not represented (un-deformed models). From the values obtained: $\sigma_{max_{square}} \approx 1.11 \cdot \sigma_{max_{circle}}$. (Study details in Annex 3); c) Stress lines of tension/compression in the horizontal direction. Highest stress concentration where lines are closest.

An interesting fact is that WWII aircraft windows were designed with a square geometry as can be see Figure 23. Because crack initiation and propagation was consistently observed in the corners of the windows, the phenomena was studied and, consequently, square windows had their vertices rounded or were replaced by oval ones.

The optimum corner radius for square and rectangular openings can be found in Figures 26 and 27 as function of load factor and geometry [47] [49].

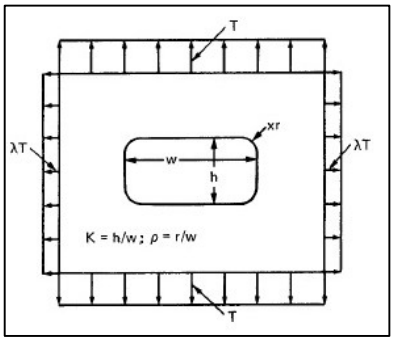

Figure 26 - Geometry and notation of a rectangular opening under loading [49].

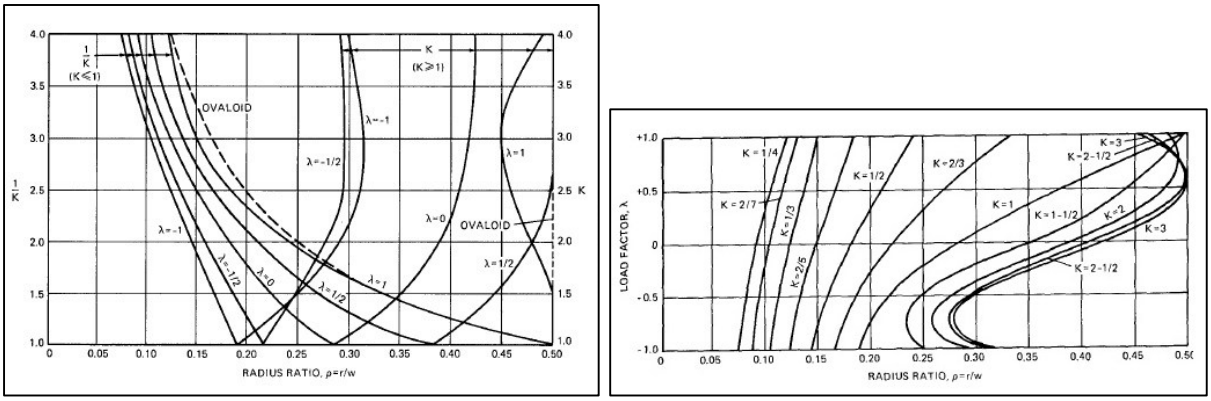

a) b)

Figure 27 – a) Most favorable radius ratio for various openings in contours of load factor; b) Most favorable radius ratio in contours of aspect ratio [49].

The necessity to reinforce the areas around the holes/cut-outs, where maximum stresses are observed, is usually defined by the material's tensile strength but, for some materials, the shear strength can become the limiting factor.

One such case are the unidirectional laminate composite materials. For this type of materials the tension of a broken fiber is transmitted to the adjacent fibers by pure shear (three-dimensional homogeneous flattening of a body [50]) through the matrix. See Figure 28.

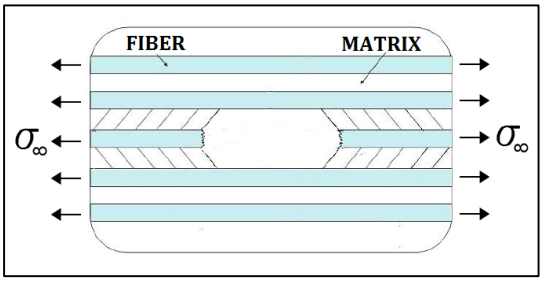

Figure 28 – Tension of a broken fiber transmitted to adjacent fibers through the matrix [51].

As explained in section 4.2.2 stress can also be given by: $\sigma = E \cdot \varepsilon = \tau = G \cdot \gamma$. Because the modulus of rigidity (G) of the matrix is usually much higher than the fiber's, for the same composite shear displacement (strain, γ), the matrix shear stress will be higher than the fiber's.

Because $\sigma = \tau$ and the ultimate tensile strength (σ_u) of the matrix is usually much less than the fiber's, the matrix material will start to fail well before any fiber and so the phenomenon of delamination will occur.

4.5.1.1 Holes / Cut-outs Reinforcement Solutions

The reinforcement method used depends, mostly, on the material and the thickness of the surface where the hole/cut-out is made.

In general, the solution usually consists of adding material in the areas where the highest stress concentration is observed. This is usually the case for isotropic materials. Possible configurations of reinforcements can be observed in Figure 29.

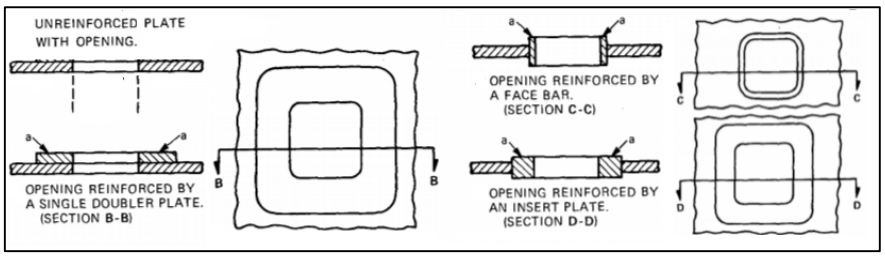

Figure 29 – Types of reinforcements [52].

For laminate composite materials NASA studied the effect of ply orientation in the intensity and distribution of the stresses around holes/cut-outs, concluding that it is possible to optimize it in order to reduce the maximum stress value obtained [53]. The use of this method translates into the need for a localized optimization of the laminate around the hole/cut-out.

For optimized structures with continuous fiber reinforced laminate composites, the components, usually, already have their plies oriented for overall optimal structural strength and rigidity and so the plies cannot be reoriented locally. Therefore, a reinforcement solution is to add extra plies locally and in an optimized manner, in a similar fashion as for the isotropic materials (as shown in Figure 29). For best results and also avoid delamination, the additional plies should be laid-up in an alternate and symmetric fashion in regard to the laminate center [44].

4.5.1.2 Delamination when Drilling / Cutting laminates

When drilling/cutting laminate materials delamination is likely to occur. The delamination is divided into *peel-up* and *push-down*, for tool entrance or exit, respectively. These mechanisms are explained in detail by [54] [55]. See Figure 30.

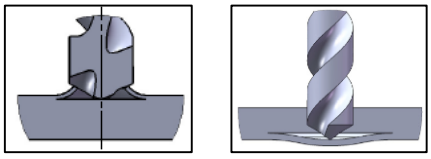

a) b)

Figure 30 – Delamination mechanisms: a) Peel-up delamination at entrance; b) Push-down delamination at exist [54].

For continuous fiber reinforced laminate materials the occurrence of delamination when drilling/cutting is very high and the damage depends not only on the material properties but also on the tool and technique used [54] [56] [57] [58] [59] [60] [61] [62] [63] [64].

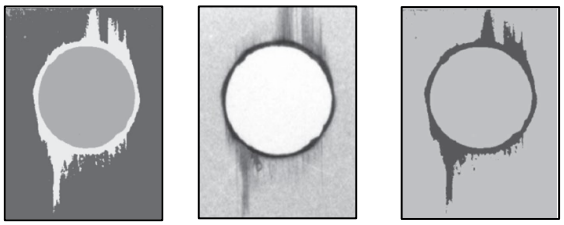

a) b) c)

Figure 31 – Delamination of unidirectional fiber reinforced laminate: a) Original image; b) Image segmented by using neuronal network; c) Identification of the delamination region [54].

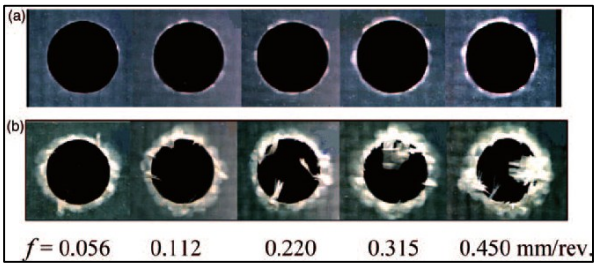

Figure 32 - Effect of feed on delamination in drilling glass fiber reinforced composites: a) peel-up delamination; b) push-down delamination.

Despite being possible to determine the damage area/radius for a specific material with experimental methods, one should be able to estimate a theoretical safety damage margin for conceptual structural design purposes.

Based on the visual analysis of images from two different case studies from different authors, Figure 31 and 32, it was concluded that the greatest damage occurs for unidirectional fiber reinforced laminates when the tool is cutting orthogonally to the fiber direction and that the damage intensity seems to be proportional to the cutting radius.

Therefore, based on the above, the present thesis will use the following assumptions:

- For unidirectional fiber reinforced laminates the maximum damage distance from the cut border will be considered to be equal to 1/2 of the cutting tool diameter for the longitudinal fiber direction ($D_{damage_{Uni\_0^o}} = 2 \cdot D_{cutting\_tool}$) and 1/9 of the cutting tool diameter for the transverse direction ($D_{damage_{Uni\_90^o}} = \frac{11}{9} \cdot D_{cutting\_tool}$);
- For bidirectional fiber reinforced laminates the maximum damage distance from the cut border will be considered to be equal to 1/3 of the cutting tool diameter ($D_{damage_{Bi}} = \frac{5}{3} \cdot D_{cutting\_tool}$).

4.6 Wing Structure Initial Model

4.6.1 Materials Selection and Properties Definition

Wanting to minimize the weight of the structure while still being able to maintain a high structural strength and stiffness, the obvious choice of ideal material are carbon fiber laminate composites since they are the type of material with the best structural efficiency (best strength-to-weight ratio $\sigma_u/(\rho \cdot g)$ and best stiffness-to-weight ratio $E/(\rho \cdot g)$ - see section 4.1).

Furthermore, knowing that the aircraft, to which the present wing belongs to, is expected to operate in a high salinity environment (maritime surveillance), the use of composite materials is also ideal due to their non-metallic nature which translates into the avoidance of corrosion problems. It should be understood that, for metallic structures, corrosion problems are a major structural problem and that the protection of metallic surfaces against it has high monetary costs and also, in some cases such as chromium

bath solutions (aluminium anticorrosion treatment), can pose serious health issues for humans and the environment.

One of the limitations of the present work was to use the materials available at the *Centro de Investigação, Desenvolvimento e Inovação da Força Aérea* (CIDIFA). Fortunately, there is a good variety of materials to choose from. From the materials available, the following were selected to be used in the structure (see Figure 33):

- Bidirectional Carbon Fiber, 3K, High Strength (HS), 160 $[gr/m^2]$, P (plain weave);
- Unidirectional Carbon Fiber, 3K, HS, 215 $[gr/m^2]$, 15 [cm] tape;
- Epoxy Resin: SR 1500 + Hardener: Sicomin SD 2505 (100 [g] Epoxy - 33 [g] Hardener);
- Airex C70.75, thickness 3 [mm], (isotropic material);
- Kevlar 49, 195 denier, bidirectional, plain weave.

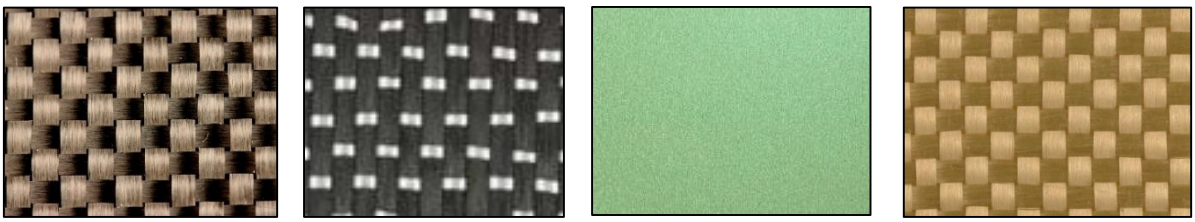

a) b) c) d)

Figure 33 – a) Bi Carbon Fiber; b) Uni Carbon Fiber; c) Airex C70.75; d) Kevlar 49 (aramid fiber).

Many combinations of laminate composite materials could have been obtained from the materials selected, each one, with unique mechanical properties.

In order to simplify the design process, and create a starting point for future material optimization studies, all the laminates created had all their plies oriented in the same direction (0º).

Also, the percentages of resin and hardener as well as the curing conditions were kept the same for all materials: 100 [g] Epoxy - 33 [g] Hardener, 20ºC Cure, dry heat air conditioning, -0.5 [bar] vacuum, 24H duration.

Furthermore, in order to obtain a perception of how the physical characteristics of a composite change with the number of plies (thickness), different configurations were created. This was a crucial step because it allowed to understand the limitations of the materials in terms of their minimal thickness possible and associated porosity and permeability. These notions were essential for the translation of the theoretical project into a feasible one.

According to the information provided above, the following composite materials were manufactured using the hand-lay-up method:

- Epoxy + Bi Carbon Fiber (Bi CF): $[C_1^{0º}]$; $[C_2^{0º}]$; $[C_4^{0º}]$; $[C_{10}^{0º}]$; $[C_{11}^{0º}]$; $[C_{12}^{0º}]$; $[C_{13}^{0º}]$; $[C_{14}^{0º}]$;
- Epoxy + Uni Carbon Fiber (Uni CF): $[C_1^{0º}]$; $[C_2^{0º}]$; $[C_9^{0º}]$; $[C_{10}^{0º}]$; $[C_{11}^{0º}]$; $[C_{12}^{0º}]$;
- Epoxy + Bi Carbon Fiber + Airex: $[C_1^{0º}/A_1/C_1^{0º}]$;
- Epoxy + Airex: $[A_1]$;
- Epoxy + Kevlar: $[K_2^{0º}]$;
- Epoxy + Bi Carbon Fiber + Kevlar: $[C_1^{0º}/K_2^{0º}/C_1^{0º}]$;

Some of the physical and mechanical properties of the available materials as well as some of the properties of the materials manufactured are listed in the Tables 2, 3 and 4. Material costs were also determined.

Table 2 – Properties of the Available Materials.

	Epoxy Resin SR 1500 + Hardener Sicomin SD 2505 (100 [g] Epoxy - 33 [g] Hardener) (20ºC Cure, Dry heat air conditioning, -0.5 [bar] vacuum, 24H)	**Carbon Fiber, 3K, HS, Bidirectional, 160 P (plain weave) (160 [gr/m^2])**	**Carbon Fiber, 3K, HS, Unidirectional, 215 [gr/m^2], 15 [cm] tape**	**Airex C70.75**	**Kevlar 49, 195 denier, bidirectional**
Thickness "per ply" (dry – no resin) [mm]	-	0.16	-	3	0.1
Mass Density (dry) [g/mm^3]	1.00E-03	-	-	8.90E-05	1.44E-03
Yield and Ultimate Tensile Strength (0º) [MPa]	-	-	-	2	-
Yield and Ultimate Tensile Strength (90º) [MPa]	-	-	-	2	-
Compressive Strength (0º) [MPa]	-	-	-	1.45	-
Compressive Strength (90º) [MPa]	-	-	-	1.45	-
Shear Strength (τu) [Mpa]	-	-	-	1.2	-
Tensile Modulus E [MPa]	-	-	-	66	-
Compression Modulus E [MPa]	-	-	-	104	-
Elastic Modulus (Average between tensile and compressive) [MPa]	-	-	-	85	-
Shear Modulus (G) [MPa]	-	-	-	30	-
Poisson's Ratio	-	-	-	0.3	-
Thermal conductivity at room temperature (20ºC) [W/m.K]	-	-	-	0.033	-
Thermal expansion coefficient [/K]	-	-	-	4.39E-05	-
Cost [€/mm^2]	-	2.10E-05	-	3.07E-05	6.32E-05
Cost [€/g (dry)]	0.1015	-	-	-	-

Table 3 – Properties of the Manufactured Materials.

	Epoxy + Bi Carbon Fiber $[C_{10}^{0º}]$	**Epoxy + Uni Carbon Fiber** $[C_9^{0º}]$	**Epoxy + Bi Carbon Fiber + Airex** $[C_1^{0º}/A_1/C_1^{0º}]$	**Epoxy + Airex** $[A_1]$	**Epoxy + Kevlar** $[K_2^{0º}]$
Approximate Liquid Relations:	100 [g] Carbon fiber - 85 [g] Epoxy + Hardener	100 [g] Carbon fiber - 80 [g] Epoxy + Hardener	-	-	-
Fiber Volume Percentage [%]	-	-	-	-	44
Resin Mass Percentage (after curing) [%]	37 (for laminate with 10 Plies)	34.5 (for laminate with 9 Plies)	-	78.9	47
Average Ply thickness [mm]	0.19 (for laminate with 10 Plies)	0.222 (for laminate with 9 Plies)	-	3	0.13 (for laminate with 2 Plies)
Mass Density [g/mm^3]	1.30E-03 (for laminate with 10 Plies)	1.45E-03 (for laminate with 9 Plies)	-	4.22E-04	1.20E-03
Tensile Modulus in X (E1) [MPa]	44792.61	95069.96	-	-	-
Tensile Modulus in y (E2) [MPa]	53192.65	9172.87	-	-	-
Tensile Modulus in Z (E3) [MPa]	9172.87	9172.87	-	-	-
Longitudinal Tensile Modulus in 45º (E1') [MPa]	17433.91	10028.54	-	-	-
Poisson's Ratio in XY (ν12)	0.06	0.262	-	-	-
Poisson's Ratio in YZ (ν23)	0.388	0.396	-	-	-
Poisson's Ratio in XZ (ν13)	0.388	0.262	-	-	-
In-plane Shear Modulus in XY (G12) [MPa]	5000	5000	-	-	-
Out-of-plane Shear Modulus in YZ (G23) [MPa]	2889	3470	-	-	-
Out-of-plane Shear Modulus in XZ (G13) [MPa]	2889	5000	-	-	-
Yield Tensile Strength in X (0º) (σc) [MPa]	622.598	1500	-	-	410
Ultimate Tensile Strength in X (0º) (Stu or σu) [MPa]	622.598	1500	-	-	-
Yield Tensile Strength in Y (90º) (σc) [MPa]	508.568	22.467	-	-	-
Ultimate Tensile Strength in Y (90º) (Stu or σu) [MPa]	508.568	22.467	-	-	-
Yield Tensile Strength in Z (σc) [MPa]	22.467	22.467	-	-	-
Ultimate Tensile Strength in Z (Stu or σu) [MPa]	22.467	22.467	-	-	-
Yield Compressive Strength in X (0º) (σc) [MPa]	570	1200	-	-	199
Ultimate Compressive Strength in X (0º) (Stu or σu) [MPa]	570	1200	-	-	-
Yield and Ultimate Compressive Strength in Y	570	250	-	-	-

(90º) (σc) and (Stu or σu) [MPa]					
Yield and Ultimate Compressive Strength in Z (σc) and (Stu or σu) [MPa]	250	250	-	-	-
Yield Shear Strength 45º (σc) [MPa]	57.66	49.413	-	-	-
Ultimate Shear Strength 45º (Stu or σu) [MPa]	115.33	49.413	-	-	-
Yield In-plane Strength (τ12c) [MPa]	45	70	-	-	-
Ultimate In-plane Shear Strength in XY (τ12u) [MPa]	90	70	-	-	-
Thermal Expansion Coefficient in X (0º) [/K]	2.1	-0.3	-	-	-
Thermal Expansion Coefficient in Y (90º) [/K]	2.1	28	-	-	-
Thermal Expansion Coefficient in Z [/K]	28	28	-	-	-

Table 4 – Material's physical characteristics Vs number of Plies.

Material	**Nº of Plies**	**Density [g/mm^3]**	**Fiber Mass Percentage [%]**	**Laminate thickness [mm]**	**Thickness per Ply [mm]**
Epoxy + Bi CF	1	0.000762	75	0.35	0.35
	2	0.001088	71.4	0.49	0.245
	4	0.001255	66	0.85	0.213
	10	0.0013	63	1.9	0.19
	11	-	-	2.02	0.184
	12	-	-	2.15	0.179
	13	-	-	2.3	0.177
	14	-	-	2.45	0.175
Epoxy + Uni CF	1	-	-	0.45	0.4
	2	-	-	0.65	0.325
	9	0.00145	65.5	2	0.222
	10	-	-	2.2	0.22
	11	-	-	2.4	0.218
	12	-	-	2.6	0.217
Epoxy + Kevlar	2	0.0012	53	0.26	0.13

The properties presented in the tables 2, 3 and 4, are all that were needed for the development of the present work.

Due to the importance of accuracy of the properties of the created materials, experimental procedures were conducted in accordance with regulations from the American Society for Testing Materials (ASTM). See Annex 4.

All the necessary properties that could not be obtained via experimental means were obtained from statistical data or, as a last resort, using theoretical methods. The Tables 12-15 in Annex 6 contain various sets of data from the different sources/methods and the final selected and/or calculated values, attributed to the materials.

It should be noted that for all cases where experimental data was obtained, it was compared to the values of both the two other sources in order to verify that no substantial experimental errors had occurred.

It will now be explained the methodology used to determine the materials' final properties from the experimental, statistical and theoretical methods and sources.

4.6.1.1 Experimental Procedures and Data Acquisition

For the determination of a specific material's property, e.g. tensile strength in the x direction, the ASTM regulations require the use of "at least 5 specimens per test". However, due to time restrictions, only one specimen was used for each test.

Nevertheless, for materials that needed extensive characterization, namely, Epoxy + Bi CF [$C_{10}^{0^o}$] and Epoxy + Uni CF [$C_9^{0^o}$], at least 5 specimens of each type were manufactured (see Table 5) and, after inspection, the one with the best finish was selected. This was the only occasion when rules/ procedures were not fully met.

For consistent properties throughout the specimens of the materials, the specimens were all obtained from the same flat plate, which was manufactured with materials from the same batch.

The flat plate was obtained by hand-lay-up lamination method followed by a curing process using a vacuum bag at -0.5 [bar] during 24H, at a room temperature of 20ºC, with the air-condition system set to dry heat (low humidity environment). The specimens were then obtained by cutting them from the plate using the *computer numerical control* (CNC) machine available at the CIDIFA and their final finish was obtained by hand sanding with a fine grit (180) sandpaper. All specimens of the type, for each material, were simultaneously sanded so that their final dimensions would be the same.

Specimens for compression testing suffered an additional step as tabs, of the same material and with the same fiber orientation, were glued (with epoxy resin) to their extremities. Figures 34-42 show some of the steps of the specimen's manufacturing process. Table 5 shows the specimens' final dimensions.

a)

b)

Figure 34- Materials cut to length, ready for hand-lay-up lamination process: a) Bidirectional Carbon Fiber, 3K, HS, 160 [gr/m^2], plain weave cloth; b) Unidirectional Carbon Fiber, 3K, HS, 215 [gr/m^2], 15 [cm] wide tape.

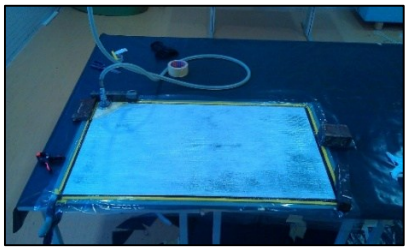

Figure 35 – Curing process of the laminate: vacuum bag at -0.5 [bar] during 24H, at a room temperature of 20ºC, with the air-condition system set to dry heat (low humidity environment). Plies were laid-up over a polished glass and covered with Compoflex® 150 SBRF [250 g/m^2] which acts as a peel-ply and breeder allowing for the excess resin to be removed. All materials were then covered with a plastic sheet and sealant tape was used to allow for the vacuum to be created. Note: the polished glass was treated with a de-molding substance (wax) to keep the composite from sticking to it.

Figure 36 – Composite flat plate mounted on the CIDIFA CNC machine, ready to be cut. The plate was fixed to the table using wood screws.

Figure 37 – Milling tool used to cut the composite: 4 IZAR 4600 N HSS E/Co8 Stg.21.8 (diameter: 4 [mm]).

a)

b)

Figure 38 – Detail: Flat plates after cutting – a) Bidirectional carbon fiber; b) unidirectional carbon fiber. As expected, greater delamination damage on the unidirectional material.

Figure 39 – Obtained specimens: Intermediate stage - types: 1,2 and 5 complete (see Table 5).

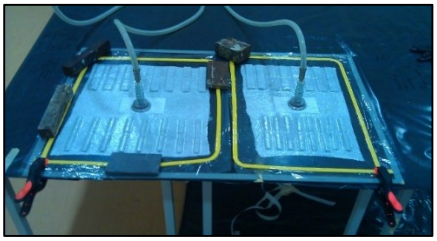

Figure 40 – Tabs being glued to the compression specimens of each of the two materials.

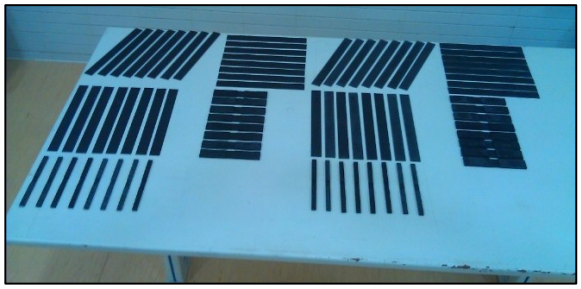

Figure 41 - Obtained specimens: Final stage - types: 1,2,3,4 and 5 complete (see Table 5).

a)

b)

Figure 42 – Detail: a) Type 3 specimen: Compression, 0º Bi; b) Type 4 specimen: Compression, 90º Bi.

Table 5 – Manufactured Specimens

Specimen Type	Test Type	Fibers' Direction	Quantity	Lenght [mm]	Width [mm]	Thickness [mm]	"Tab" Lenght [mm]	"Tab" Thickness [mm]
1	Tension	0º Uni	8	251±0.5	26±0.25	2±0.08	-	-
1	Tension	0º Bi	8	251±0.5	26±0.25	1.9±0.08	-	-
2	Tension	90º Uni	8	251±0.5	26±0.25	2±0.08	-	-
2	Tension	90º Bi	8	251±0.5	26±0.25	1.9±0.08	-	-
3	Compression	0º Uni	8	151±0.5	11±0.10	2±0.08	65±0,5	2±0,02
3	Compression	0º Bi	8	151±0.5	11±0.10	1.9±0.08	65±0,5	1.9±0,02
4	Compression	90º Uni	8	151±0.5	26±0.25	2±0.08	65±0,5	2±0,02
4	Compression	90º Bi	8	151±0.5	26±0.25	1.9±0.08	65±0,5	1.9±0,02
5	Tension	45º Uni	8	251±0.5	26±0.25	2±0.08	-	-
5	Tension	45º Bi	8	251±0.5	26±0.25	1.9±0.08	-	-

It should be noted that although tension and compression specimens were manufactured, compression data could not be obtained experimentally due to the lack of equipment (specific machine grips need). That data had to be obtained from statistical sources [65]. Other data, such as the Poisson's ratio in YZ (ν23) and the In-plane Shear Modulus, also had to be obtained from statistical sources or theoretical methods [66] as shown in Annex 6.

For both Epoxy + Bi CF [$C_{10}^{0º}$] and Epoxy + Uni CF [$C_{9}^{0º}$], during the tensile tests, two different types of extensometers (strain gauges) were used. This was done so that the strain values from more than one source could be compared and so that the properties of the materials could be determined more accurately. Both sensors were unidirectional strain gages but used different attachment methods. Figure 43 shows both types of strain gauges:

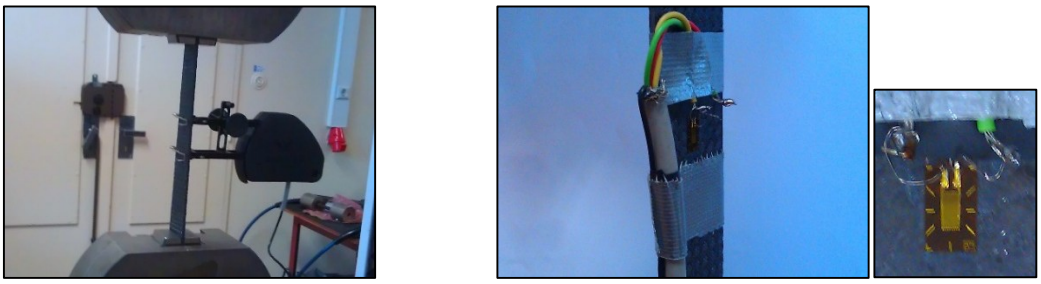

a) b)

Figure 43 – a) Gauge Name: INSTRON 2630-106. Specs: Type: STATIC; Resistance: 350 Ω; Travel: +12.5 mm/-2.5 mm; Gauge length: 25 mm; Gauge length accuracy: ±0.5 % of the gage length. Attachment method: Surface attachment by a combination of pressure and friction; b) Gauge Name: HBM 1-LY16-3/120. Specs: Resistance: 120 Ω ±0.35 %; K-Factor: 1.98 ±1.0 %; Max. rms bridge excitation voltage: 0.5 V; Temperature coefficient 93 ±10 [$10^{-6}/K$]; Attachment method: glued with Loctite Super COLA 3.

The data acquired from a) consisted of graphs of Load [N] vs Strain obtained directly from the computer software associated to the extensometer and to the test machine. The graphs obtained are presented in Annex 5, Figure 79 a)-f).

From b), two sets of data were acquired: stresses obtained directly from the computer software associated to the machine; and strains obtained from the extensometer/s mounted on a *Wheatstone Bridge*. The data obtained consisted of: Stress vs Load (N) and Strain vs Data point number (#), respectively.

The Wheatstone Bridge was configured as a *quarter-bridge* when only one extensometer was glued to the specimen being tested and, configured as a *half-bridge* when two extensometers were glued to the specimen being tested. See Figure 44.

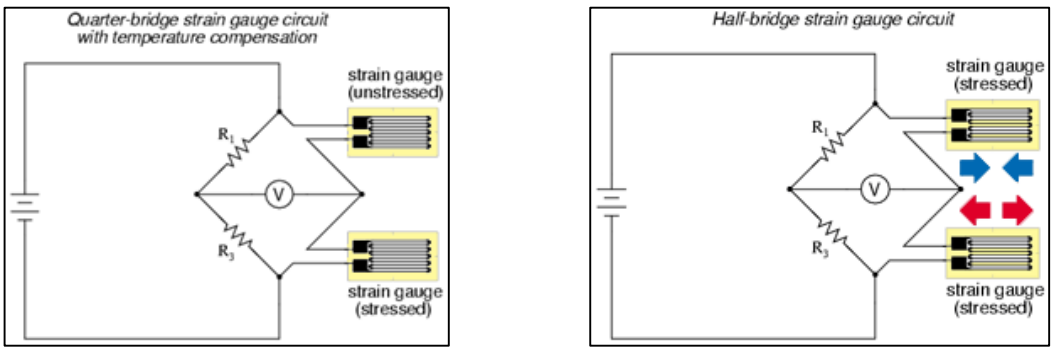

a) b)

Figure 44 - Wheatstone Bridge configurations: a) Quarter-bridge with temperature compensation; b) Half-bridge.

In the quarter-bridge configuration an extensometer glued on another specimen of the same material was connected to the circuit to serve as temperature compensation strain gage. This specimen was left over a wooden table and was never touched or handled during the test.

The rates of data acquisition from the computer and the bridge were different so two separate types of graphs were created for each specimen: Stress vs Data point # and Strain vs Data point #. The latter was either: Longitudinal Strain vs Data point # or Transverse Strain vs Data point #.

The transverse strain was obtained by gluing a second extensometer in the transverse direction on the opposite face of the specimen (see Figure 45 a)). For this test, both extensometers were connected to the bridge and all the data was obtained simultaneously. The longitudinal oriented extensometer suffered tension while the transverse suffered compression due to reduction of the specimen's cross section due to the Poisson's effect.

The data points numbers (#) were synchronized so that stress and strain could be obtained from different graphs for the same loading condition (same data point). All the graphs created are presented in Annex 5, Figure 80 a)-n).

It should be noted that synchronization was only possible because the carbon fiber composites failed (ruptured) in a brittle manner and so, when the failure occurred the strain also plummeted to lower values thus becoming easy to identify the data point for which failure had occurred.

The only situation where there was some difficulty in synchronizing data points was for the Bidirectional carbon fiber specimens with fibers oriented in the 45º direction. For this case, yield was substantial before material failure and the extensometer showed signs of debonding from the specimen's surface. In addition, the extensometer suffered extensive plastic damage and it stopped working properly (constant value being measured) as can be seen in Figure 80 n) in Annex 5. Because the final value measured was close to the one obtained by the simply attached extensometer, it leads to believe that its true strain might be greater than the one obtained. Nevertheless, the final strain value was within the theoretical range and so, it was considered valid. See Figure 45 b).

It should also be noted that the specimen of the unidirectional carbon fiber material could not be broken by the machine because not enough strength was available (max load available: 5000 [kg]; load required: 8320 [kg] (estimated)). The slight inflection on the correspondent strain graph corresponds to when the machine was stopped and started to alleviate the applied load. See Figure 80 a)-c) in Annex 5.

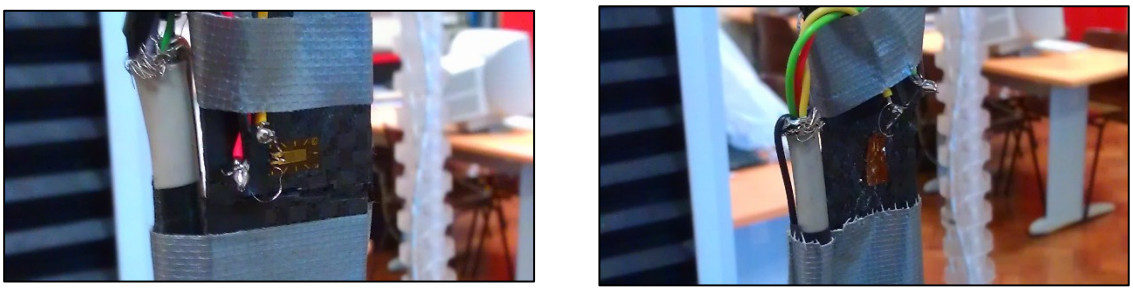

a) b)

Figure 45 – Comparison between specimens' failure modes and the correspondent final shapes of the strain gages attached: a) 0º or 90º Bi CF specimen. Transversely oriented strain gage is shown. Gage remained glued and does not show any visible plastic deformation (although not shown, the same was observed for the longitudinal gage); b) 45º Bi CF specimen. Longitudinally oriented strain gage. Gage with substantial plastic deformation and detached from the specimen's surface.

Concerning the experimental data obtained, it should be noted that no average was performed between values of a) and b) for E1 and E2. Comparing these values (Tables 12 and 13 in Annex 6) it is evident that in a), due to the attachment method, the gauge suffered slippage, not being able to record the true (larger) strain (ε) of the material and consequently leading to a higher value of E (E=σ/ε). The selected values were therefore, the ones obtained in b).

Also, for both materials, the values of E3 and the ultimate tensile strength in z were considered to be equal to the values of E2 and the ultimate tensile strength in y of the unidirectional material. The logic behind this approximation is that the resin, in itself, is an isotropic material. Since the unidirectional material has no fibers oriented in the y direction then, its y properties approximately corresponds to the resin's [66] [67]. Those properties can therefore, also be applied to the z direction of the unidirectional and bidirectional materials.

Regarding the theoretical data, it should be explained that the values presented in that section of the tables were obtained from the source [66] and that, in this regard, no calculations were performed during this thesis. The decision to directly use those theoretical values was made for the following reasons: because the fiber properties were almost completely unknown (apart from its planar density) and because the theoretical values proposed by the source were very similar to the data obtained experimentally. Nevertheless, an in depth verification of the methods utilized to obtain such values was performed. The values presented for the unidirectional carbon fiber composite were obtained from the "rule of mixtures" [68] and, for the bidirectional composite, were obtained by formulas from [69]. Additionally, the source also used experimental data from [67] to compare and validate its calculations.

Despite the fact some of the data was obtained via statistical or theoretical means, the level of trust on the overall final properties of the materials is high since the most important properties namely E1, E2, σ1, σ2 and ρ were obtained experimentally and are in concordance with theoretical and statistical values, being within the expected range of generic-carbon fiber composites of the same type.

The Epoxy + Bi Carbon Fiber + Airex [$C_1^{0^\circ}/A_1/C_1^{0^\circ}$] "sandwich" material also need extensive characterization, however, its mechanical properties could not be obtained via experimental testing due to the recurrent problem of the foam failure by buckling, under the pressure of the machine grips, during testing. Furthermore, due to its specific combination of materials and thicknesses, no statistical data was available and no apropriate theoretical models were found.

The solution used was to determine the properties of the foam and the carbon-epoxy laminate, separately. This way, if the structural analysis is conducted using a computational tool, the material could be defined (created) layer by layer in the software. The final properties of the sandwich material will depend on the accuracy of the software algorithm to simulate the reality.

Most of the foam's properties were obtained from the manufacturer [70] or other statistical sources [71] except for its density that was obtained experimentally.

The carbon-epoxy laminate was assumed to have the same mechanical properties as the Epoxy + Bi CF [$C_{10}^{0^\circ}$], including the same thickness per ply. This will be further explained in section 4.6.1.2.

No mechanical properties were determined for the material Epoxy + Airex: [A_1] since it was created with the main objective to observe how the epoxy resin interacts with the surface of the Airex foam. More specifically, how much and how deep does the resin impregnate the foam surface due to its porosity.

The properties obtained for the material Epoxy + Kevlar: $[K_2^{0^o}]$ were also minimal since it does not play a structural role. As mention previously in section 4.4 its function will be, to be used as the articulate connection between the wing structure and the flaps and ailerons. This being said, only its yield tensile and yield compressive stresses were obtained in order to be possible to evaluate if a laminate that includes Kevlar will resist a certain applied load without failing.

4.6.1.2 Data analysis / Important Remarks

As explained previously, several laminate configurations of a single material (same material but different number of plies) were created so that the limitations of the materials in terms of their minimal thickness possible could be determined and their associated porosity and permeability could be understood. In fact, it was observed that composites composed of a single ply show high porosity not being suitable for applications where impermeability is needed, e.g. wing skin. However, for two plies with or without an additional core, porosity is almost nonexistent.

The various laminate configurations were also created with the objective to determine the equivalent number of plies between the bidirectional and the unidirectional carbon fiber materials that allowed them to have equal thickness, so that it would be possible to directly use the mechanical properties from the y direction of the unidirectional material to describe / determine the mechanical properties in the z direction of the bidirectional material.

Additionally, from the analysis of Table 4 it was concluded that laminate composites obtained via hand-lay-up and cured using a vacuum bag, suffer an increase of density with the increase of the number of plies. Nevertheless, the rate of increase decreased with the increase of the number of plies. This could be explained by the reduction of the material's internal voids due to a larger percentage of resin "trapped" between the fibers of each ply.

It was also observed that, although density increased, the thickness per ply decreased. This could be explained by a better compaction of the fibers between the various plies therefore, reducing the average ply thickness.

About using the mechanical properties obtained to define the properties of different configurations (same material but different number of plies):

Two equal materials with the same number of plies (same quantity of fibers) but with different thicknesses (different quantities of resin) should fail for approximately the same applied load (N) because the fibers are the component that gives the material its strength.

Also, for two equal materials with the same number of plies and same thickness but different densities, the less dense material will fail before the denser one. This is because of the weaker bonds between the fibers due to the larger number of void spaces inside the laminate. This situation correlates to the proverb that *"it is easier to break a single stick than a bunch of them together"*. In fact, although the fibers are still close to one another, the voids cause the lack of an intermediate material to distribute the loads of a single fiber to the adjacent ones (see Figure 28 in section 4.5.1) and so, after a single fiber breaks, a "chain reaction" can occur and if enough fibers break, the material will fail.

Therefore, from the analysis of Table 4, if the mechanical properties determined are used for a configuration with a higher number of plies, no structural problems should arise. However, if a fewer

number of plies is used, attention should be paid to the correspondent configuration density in order to evaluate if there would be the risk of premature material failure.

This being said, from Table 4 it can be concluded that, as long as no laminate is created using a single ply, the density will remain approximately constant and so the mechanical properties determined, can be safely applied to stacks of different number of plies of the same material (as long as the fibers orientation is maintained, in this case 0º).

It should be understood that the specimens from which mechanical and physical properties were determined didn't have smaller thicknesses also due to the ASTM regulations. The other two reason were: the need to find the equivalent number of plies between the unidirectional and the bidirectional material as explained previously, and the need to accurately predict the structure's mass.

About the prediction of the structure's mass:

In order to exactly determine the mass of the final structure it would be necessary to fabricate each and every one of the components material's configuration in order to experimentally obtain their densities.

Nevertheless, by simply using the densities of the material's configurations already tested, a good estimation can be achieved. That prediction will be conservative if the configuration has an inferior number of plies and, be kept almost constant, for a configuration with a larger number of plies.

4.6.2 Design

Based on all the information presented prior to this section, an initial wing structure was idealized in order to meet all the aircraft's structural and operational requirements.

Because Flaps and Ailerons have a minimal contribution to the wing's overall capability to withstand maximum loads (as mentioned previously), they were considered not to be part of the wing structure. They are still part of the wing, as payload or servo motors also are, but are not part of its structure. Their individual structures will be addressed later, in section 6.1.

The non-inclusion of these trailing edge devices is a conservative approximation because their inclusion would further, slightly, increase the wing structural rigidity and decrease the maximum stresses.

It should be noted that although this devices are not part of the designed structure, nor are the payload pod or the servo motors, their forces and moments are still present and applied to the wing structure, as described in section 3.

According to the above, for the half-wing without the aileron or the flap, the components that make up the structure, as well as their respective locations, were defined as follows:

- **Skin:** Plain geometry; Constant thickness throughout the span.
- **1st Spar:** Located at $0.28 \cdot c(z)$; Along the full length of the wing (3.250 [m]) plus a root extension (0.250 [m]) for attachment purposes (wing to fuselage); Constituted by 2 Caps and 5 Webs:

  From $-0.250 \leq z \leq 0$ $[m]$ (root extension)

  - Caps and Webs:
    - Constant thickness;
    - Constant section (no tapper).
  - Caps:

- Constant twist angle of 4.4º (equal the wing root ($z = 0\ [m]$));
- Constant width: 80 [mm].

▪ Webs:

- Not equally spaced along the Caps width:1 at each extremity, 1 at the middle, 1 at 1/3 and 1 at 2/3 of the Caps' width;
- Kept in a vertical position (no twist).

From $0 \leq z \leq 3.250$ $[m]$ (half-wing span)

▪ Caps and Webs:

- Constant thickness throughout the span;
- Same tapper as the wing ($\lambda = 0.8$).

▪ Caps:

- In permeant contact with the inner skin surface;
- Same twist as the wing skin;
- Width at the root ($z = 0\ [m]$): 80 [mm];
- Width at the tip ($z = 3.250\ [m]$): 64 [mm].

▪ Webs:

- Not equally spaced along the Caps width:1 at each extremity, 1 at the middle, 1 at 1/3 and 1 at 2/3 of the Caps' width;
- Kept in a vertical position throughout the span (no twist).

o **2nd Spar:** Located near to the hinge axis of the trailing edge devices (flap and aileron) (distance < 16 [mm]): $0.65 \cdot c(z)$; Along the full length of the wing (3.250 [m]) plus a root extension (0.100 [m]) for attachment purposes (wing to fuselage); Constituted by 2 Caps and 2 Webs arranged in a "box" configuration (quadrangular cross-section):

From $-0.100 \leq z \leq 0$ $[m]$ (root extension)

▪ Caps and Webs:

- Constant thickness;
- Constant section (no tapper).

▪ Caps:

- Constant twist angle of 4.4º (equal the wing root ($z = 0\ [m]$));
- Constant width: 40 [mm].

▪ Webs:

- Kept in a vertical position (no twist).

From $0 \leq z \leq 3.250$ $[m]$ (half-wing span)

▪ Caps and Webs:

- Constant thickness throughout the span;
- Same tapper as the wing ($\lambda = 0.8$).

▪ Caps:

- In permeant contact with the inner skin surface;
- Same twist as the wing skin;

- Width at the root ($z = 0\ [m]$): 40 mm;
- Width at the tip ($z = 3.250\ [m]$): 32 mm.

▪ Webs:

- Kept in a vertical position throughout the span (no twist).

○ **9 Ribs:** Plain geometry; All with the same thickness; Placed at the following locations:

▪ Wing root ($z = 0\ [m]$);
▪ Payload location ($z = 0.240\ [m]$);
▪ $z = 0.4815\ [m]$ (to close skin gap);
▪ Motor 1 attachment area inner border ($z = 1.03375\ [m]$);
▪ Motor 1 attachment area outer border ($z = 1.23375\ [m]$);
▪ Motor 2 attachment area inner border ($z = 2.33825[m]$);
▪ Motor 2 attachment area outer border ($z = 2.53825\ [m]$);
▪ $z = 3.0905\ [m]$ (to close skin gap);
▪ Wing tip ($z = 3.25\ [m]$).

Additional design features:

Holes: Holes were made on the skin and ribs. It was decided that both the Ribs and the Skin would be made of bidirectional composite laminate material (due to the various stress directions that they are expected to withstand) therefore, the holes on the skin, also due to their small diameter, could either be embedded or drilled. The holes on the ribs could only be drilled due to their large diameter. Drilled holes have a true diameter (material removed) and a correspondent damage diameter (associated delamination surrounding area). Since drilling would be the worst case scenario, all holes were designed for that case and thus, the "laminate drilling damage factor for bidirectional composites" of $\frac{5}{3}$ was used (section 4.5.1.2) and the holes were designed as having a diameter equal to the damage diameter instead of their true diameter.

The purpose of performing the above procedure is to approximate as much as possible the model to the reality when running structural simulations. By removing the material from the damaged areas around the holes, the material damage is being simulated in a conservative manner. It should be noticed that for the same forces acting on a structure, if area (material) is removed stresses will increase.

Ribs:

▪ 2 holes per Rib were drilled in order to allow for the passage of electrical wires. These are also useful for water drainage or internal structural inspection. The Rib at the wing root and the Rib at the wing tip have holes with true diameters of 20 [mm] and 15 [mm] and damage diameters of 33.33 [mm] and 25 [mm], respectively. The intermediate Ribs have holes with the following true diameters: 19.63, 18.41, 18.10, 16.40 and 16.10 [mm] and correspondent damage diameters of: 32.72, 30.68, 30.17, 27.33 and 26.83 [mm].

Skin:

▪ 12 holes were drilled in the payload attachment area to allow for the bolted connection; 8 holes were drilled in each of the servo motors attachment areas to allow for bolted connections; All the holes have a true diameter of 5 [mm] and a correspondent damage diameter of 8.33 [mm].

Cut-outs: "Cut-outs" can be created by either cutting away material or by not adding material to that area during a component's construction (in the case of composite laminate materials). For the latter, the damage area was considered non-existent.

Skin:

- Two cut-outs were created in the center of both servo motors attachment areas. These were dimensioned to be large enough (100 x 100 [mm]) to allow for the servo motor to pass through the opening and to be installed inside the wing structure. Due to the quadrangular geometry of the cut-outs, their vertices were rounded in order to minimize maximum stresses on the edges of the openings. According to section 4.5.1 the corner radius was determined as follows:
  - Because the bottom skin surface is under tension during the critical flight condition identified (section 3.2.3.1) and, for that same loading condition, the skin stresses around a square hole were characterized (see Annex 3), it was then known that T > λT. However, magnitudes were not known. Therefore, it was decided to use a load factor (λ) value of 0.5: $\lambda = \frac{T_{ortogonal}}{T_{longitudinal}} = \mathbf{0.5}$. See Figure 26 and 27.

    The other parameters were obtained from the geometric parameters defined previously and from the graphs shown in Figure 26: $K = \frac{h}{w} = \mathbf{1}$; $\rho = \frac{r}{w} = \mathbf{0.38}$.

    Finally the radius was obtained: $r = w * 0.38 = 100 * 0.38 = \mathbf{38}$ $[\boldsymbol{mm}]$**.**

Attachment Areas: In order to comply with regulation's specifications [47], the attachment areas of both the payload and the servo motors were dimensioned so that the distance from their border to any hole border would always be larger than the hole true diameter (5 [mm]).

Additional Information:

- The Spars are continuous and hollow, in other words, ribs don't pass through them;
- The 1st and 2nd Spar root extensions should be as long as possible so that the area through which the wing stresses are transmitted to the fuselage can be large and, therefore, result in a decrease of maximum stresses at the connection points/surfaces between the wing and the fuselage. This being said, the 1st Spar root extension was limited to 0.250 [m] due to the maximum fuselage width being 0.5 [m]. The 2nd Spar root extension could have also been extended to 0.250 [m] but, because the main wing stresses are transmitted by the main spar and structural weight is a concern, it was decided to limit it to 0.100 [m] - enough to properly attach it to the fuselage and to enable the wing-to-fuselage connection to properly resist the torsional loads (pitching moment) applied to the wing.
- Regarding the payload and servo motors attachment areas, the necessity to add reinforcements to them will be addressed, further ahead, in sections 5.2.1 and 5.3.4.

According to the parameters defined above, the wing structure initial model was represented using the 3D modeling capabilities of the software *SolidWorks 2016 x64 Edition* (SW), as shown in Figure 46 a)-g). The figures show the components modeled as shells with no thickness and with no material attributed.

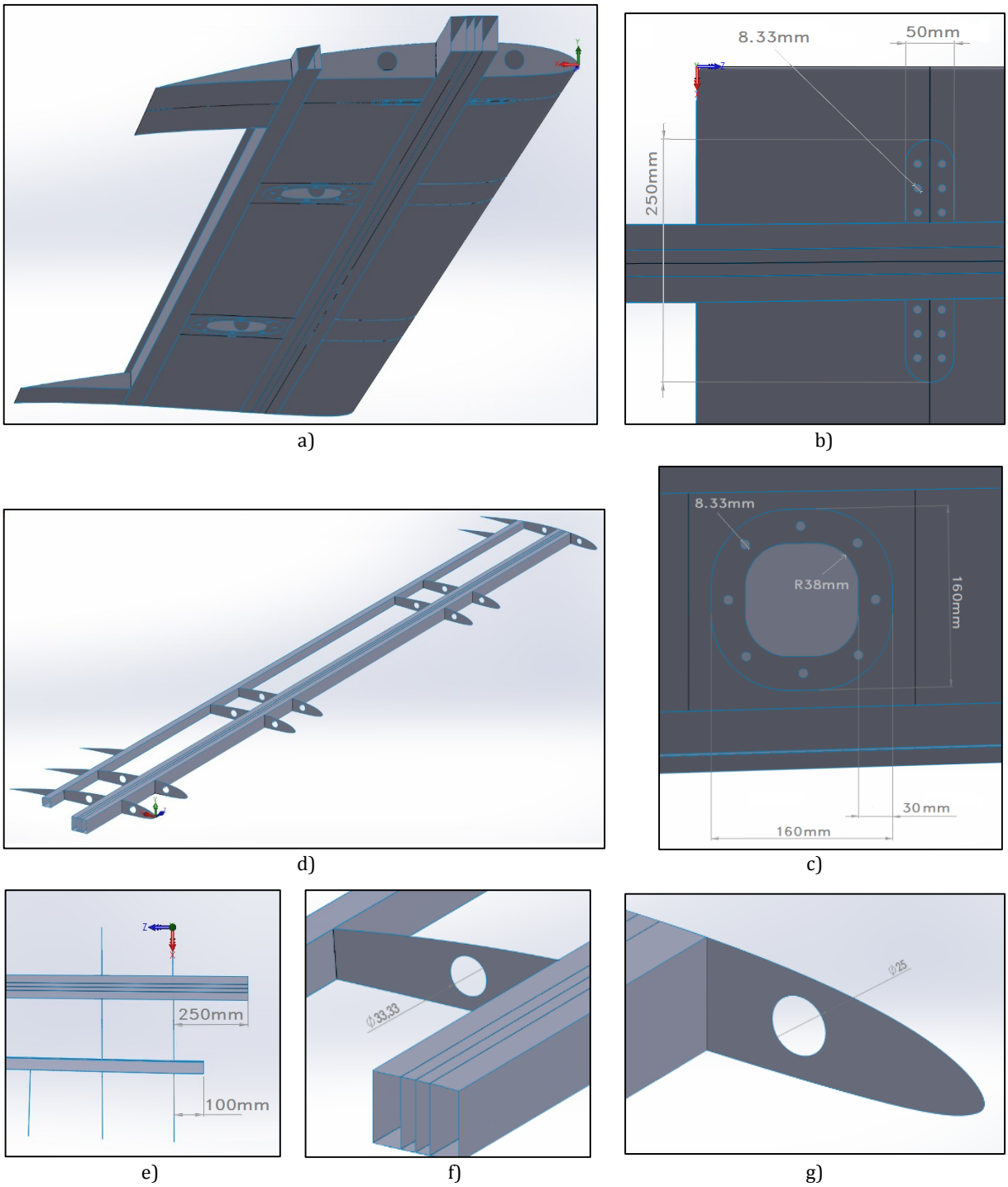

Figure 46 – Wing structure initial model: a) Bottom view of the external surface (skin) with holes and cut-outs for the payload and servo motors; b) Detail: holes and surrounding contact area for payload bolted attachment; c) Detail: holes and surrounding area for servo motor 1 bolted attachment; d) Wing internal structure: two Spars and nine Ribs; e) Detail: root extension of the spars; f) and g) Detail: hole diameter of the rib at the root and tip, respectively.

5 Wing Structure Analysis and Optimization

In this section, a simplified model of the wing structure was created and its structural response simulated and analyzed. This model and its structural characteristics, served as the starting point for a structural optimization that would culminate in a final structure that fulfilled all the structural, operational and mass requirements.

Due to the complexity of the structure it was decided to resort to a computational numerical analysis method more specifically, to finite element analysis (FEA).

5.1 Finite Element Analysis (FEA)

"This form of analysis uses the power of modern computers to predict stresses and deflections in very complex structures. The basic method involves dividing the structure into thousands, even millions of tiny structural elements" (finite elements (FE)) "that are linked to each other at nodes or junctions at their corners. Hook's law is written in matrix form for each element, and the condition is enforced that the displacement of a node shared by two elements must be the same in the statement of Hook's law for both elements. In this way, a huge matrix of equations describing the stress-strain relationships and enforced equalities of displacements for shared nodes is constructed. For most complex structures, this matrix does not have a single solution. The methods of calculus of variations (optimization theory) are used to determine a solution to the matrix that minimizes the total strain energy of the structure.

Finite element analysis is the method of choice for structural design. It has given engineering vast new capabilities for optimizing structures, saving weight, and saving money. It can truly be said that without this powerful tool current and future generations of aircraft would be less capable, more expensive, and more susceptible to unexpected structural failures" [18].

5.2 Initial Model Structural Analysis

After the materials' properties were obtained, it was then possible to perform the first structural analysis resorting to a discretization of the model into finite elements (FE).

The software used for the structural analysis was the *Dassault Systemes SolidWorks 2016 x64 Edition* (SW). The choice to use SW software, instead of another more powerful, more precise but also, more complex and less "user friendly", e.g. *ANSYS*, was mainly due to the need to considerably reduce the total design and simulation time and also, to be able to use the same software for both the geometric modelation and simulation, therefore, avoiding incompatibility problems or further model alterations (e.g. need to add connectors) thus saving time.

Time was given such a big importance due to the large number of simulations that would have to be performed during the optimization process.

Regarding the amount of time that a computer takes to perform a structural simulation, it should be understood that it also greatly depends on the specifications of the machine (computer) being used to run that simulation, especially the CPU model, the RAM memory available and the Graphics Card. The computer used for all the simulations performed during this work was an ASUS G73J with a 4 core i7 CPU

@ 1.60 GHz, with 6 GBytes of RAM and with a ATI Radeon HD 5870 Graphics Card, running the Microsoft Windows 7 Ultimate x64.

It should be noted that during the present work, a comparison between the modelation, meshing and simulation capabilities of various software was made, namely: *SOLIDWORKS 2016*, *Siemens NX 9.0*, *ANSYS 16.0 (Workbench)* and *HyperMesh*.

From these, it was determined that the SW was the one with the best modelation capabilities and overall ease of use. However, in terms of meshing capabilities, it was found to be very limited in comparison to any of the other software tested - no FE selection available (triangular FE only), minimal options for mesh manipulation, etc. Nevertheless, those simple meshing capabilities were enough for the purpose of the present work. Regarding the SW solver, it uses the industry proven *Nastran FEA* [72], therefore, the accuracy of the results mostly depend on the user inputs during the meshing and boundary conditions definition stages.

In addition to the reasons presented above, the SW was also chosen because, during his academic path, the author had already gained considerable experience with this software (mostly in its modelation aspect) due to its use in various occasions. Also, the author's knowledge of ANSYS, NX and HyperMesh was very basic therefore, the risk for erroneous user inputs was high, and if so, those would compromise all the data obtained. As the expression goes: "bad in, bad out".

5.2.1 Geometric Model Simplification

For structures which components are made up of thin sheets of material (as is the present case) it is usual to find them modeled as 2D shells (no thickness) – the material and the thickness are later defined in the simulation tool within the software [19]. This is a valid approximation as long as the thickness is considerably less than any other dimension. By applying this approximation, it was observed that the computational time of the analysis was reduced from several minutes to only a few (the duration depended on the complexity of the model being analyzed). Also, by using this simplification, any design modifications became much simpler and quicker to perform.

As expected, the results obtained from 2D and 3D were not coincident but were still within the same order of magnitude thus, the approximation was accepted. Furthermore, the 2D approximation was observed to be conservative for the maximum stress value, even for the worst case scenario were the structural model would still include the flap and aileron surfaces therefore maximizing the amount of trailing edge overlap of the top and bottom skins. See Figure 81 in Annex 7.

The geometric model used for the first structural analysis was the one presented in section 4.6.2 and shown in Figure 46 (structure modeled as 2D shells).

Nevertheless, simplifications were made to that model in order accelerate the FE discretization and simulation times and also, with the objective of having an initial structure as simple as possible for the purpose of creating a starting point for the subsequent step-by-step logical optimization of each structural component.

The simplifications performed were the following: suppression of holes and cut-outs in the skin (since additional reinforcements to the attachment areas would later be added thus causing a lowering of the stress values to the original, or even lower than if the skin had not suffered any modification),

suppression of holes and cut outs in the ribs (this holes and cut-outs were suppressed while optimization of components, either than the ribs, was being performed – this holes and cut-outs were reintroduced before rib optimization was executed), suppression of the root extensions (were replaced by equivalent boundary conditions at the wing root). See Figure 47.

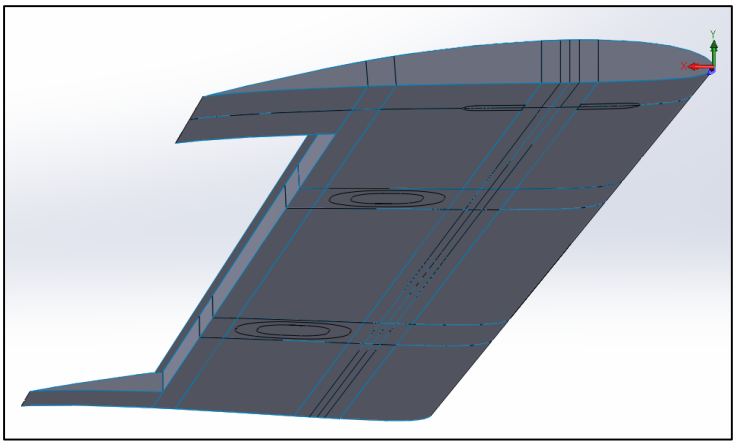

Figure 47 – Simplified Initial Model.

5.2.2 Material Attribution

In order for the "Simplified Initial Model" to become the starting point for the optimization process, a single material and a single thickness were attributed to all the 2D shells that make up the structure. The material and the thickness were the following: Epoxy + Bi CF [$C_{10}^{0º}$] and thickness of 1.9 [mm].

Since this material did not exist in the SolidWorks material's library, a new material, type: "Linear Elastic Orthotropic", was created / defined with the properties previously determined for the Epoxy + Bi CF [$C_{10}^{0º}$]. See Figure 82 in Annex 8.

When attributing the material to each shell, it was defined as "type: laminate" and all the shells were defined as being made of 2 plies of 0.95 mm.

The material was defined as "laminate" because it was the only option that allowed for the material to be oriented in a specific direction. This option would also later allow for the introduction of additional core plies of another material.

Regarding the number of plies, a component made up of a single material should ideally be defined using a single ply in order to avoid simulation errors introduced by the software incapability to fully predict the interactions between various plies. Nevertheless, because SW only allows for 2 or more plies (maximum 50), each shell had to be defined with the minimum of 2 plies. Both plies were given the same thickness in order to maintain symmetry within the laminate.

During the attribution of the material to the shells, special attention was paid when orienting the 0º direction of this composite laminate material in order to make sure it was coincident with the expected directions of the main loads – based on the theory, main loads are expected to be oriented spanwise (section 3.2.3.3).

The attributed directions were as follows (see Figure 48):

- Skin: 0º; 1st Spar Caps: 0º; 2nd Spar Caps: 0º ≡ (coincident with) "SW: Planar Mapping: Current view: Plane parallel to zx and with the direction of the 1st Spar axis ($\neq z$)";

- 1st Spar Webs: 0º; 2nd Spar Webs: 0º ≡ "SW: Planar Mapping: Current view: Plane perpendicular to zx and with the direction of the 1st Spar axis ($\neq z$)";
- Ribs: 0º ≡ "SW: Planar Mapping: Current view: xy Plane (perpendicular to z)" – x axis direction.

It should be noticed that the 2nd Spar does not have its material oriented along its own axis but rather along the 1st Spar axis direction. This was done for two reason:

- The first: in order to favor the overall structural strength and rigidity of the wing since it is expected that the aerodynamic and inertial loads will be concentrated around the 1st Spar location and acting in a perpendicular direction (y direction);
- The second: due to the manufacturing process of the spars, associated with the material thickness attributed, results in the plies that make up the webs being the same plies that make up the caps therefore, the directions attributed to the caps and the webs must be perpendicular to each other in order to ensure the bidirectional cloth fiber's continuity (heavily distorting the material to fit two non-perpendicular directions at the same time is not feasible in this case).

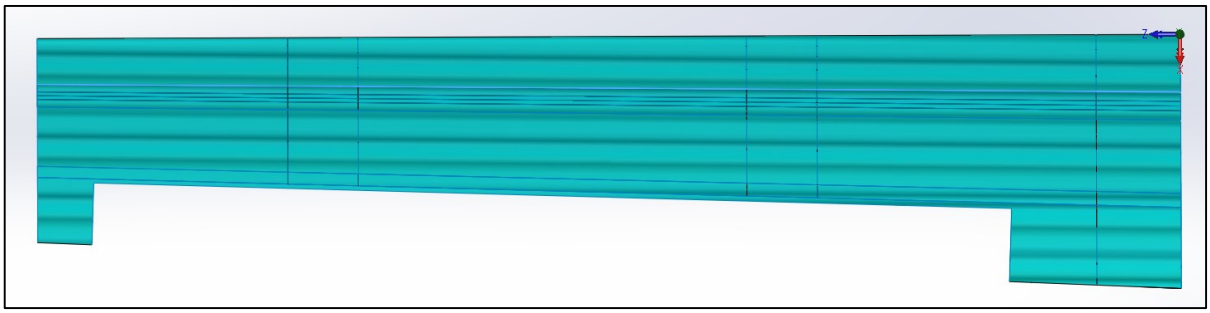

a)

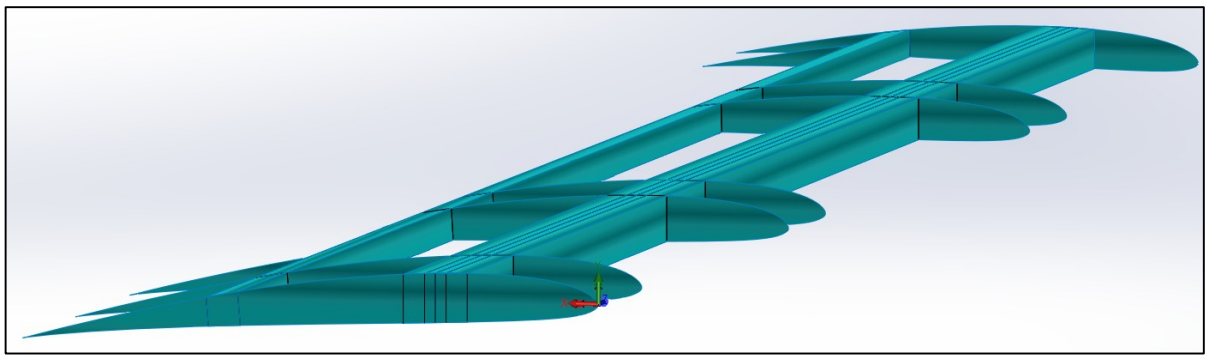

b)

Figure 48 – Material 0º Direction: a) Simplified model: Skin and Caps; b) Simplified model: Ribs and Webs.

Regarding the thickness, many 2D shells (surfaces) did not have their thickness symmetrically attributed since those were not "mid-plane" surfaces but rather "top" or "bottom" surfaces. The thickness distribution for each component and sub-component was as follows (see Figure 50):

- Skin: Thickness attributed inward in relation to the Skin 2D shell (acting as "top" surface);
- Spars Caps: Thickness attributed inward in relation to each Cap shell ("top" surface);
- Spars Webs: Thickness attributed symmetrically in relation to the Web shell ("mid" surface);
- 1st, 3rd, 8th and 9th Ribs: Thickness attributed inward in relation to the Rib shell ("top" surface);
- Remaining Ribs: Thickness attributed symmetrically in relation to the Rib shell ("mid" surface).

5.2.3 Mesh Definition and Mapping

All the surfaces were discretized in FE of the type "triangular" with a "standard mesh" and the option "Draft Quality Mesh" was selected. The initial mesh parameters were defined as: "Global FE size" of 100 [mm] with a "Tolerance" of 5 [mm]. See Figure 83 in Annex 9.

The general shape of the mesh was checked and the coincidence between the nodes of the meshes belonging to intercepting surfaces was also checked. See Figure 49.

It should be explained that in order to obtain acceptable quality meshes without needing to use any mesh manipulating tools, special care was taken when designing the geometry of each component and subcomponent shells. Each major shell was in fact designed as various single shells which were later joint together using the command "knit surfaces". Individual shells were delimited by where two different components intercepted each other or by well-defined areas. A visible example of this situation are the attachment areas of the payload and servo motors (Figure 49 c) and d)).

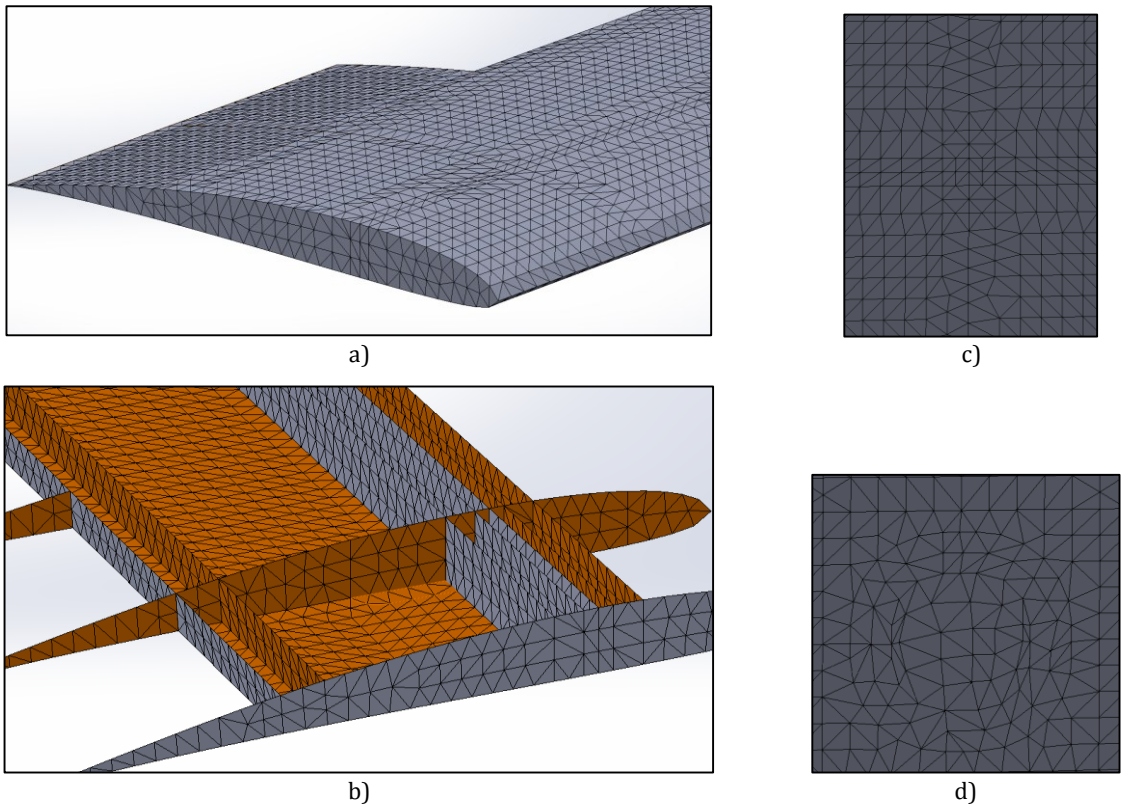

Figure 49 - Various components' meshes and respective nodes coincidence: a) Detail: coincidence between Skin and Rib nodes; b) Detail: coincidence of multiple nodes belonging to: Skin, Spars, Ribs, payload attachment area; c) Detail: payload attachment area; d) Detail: Servo motor attachment area. The mesh shown corresponds to a "Global FE size" of 20 [mm] with a "Tolerance" of 1 [mm].

During a 2D meshing of a 2D shell the SW software randomly selects the face in which the mesh will be created, afterwards being necessary for the user to manually correct that selection in order to ensure the continuity of two adjacent shell surfaces (using the command "Mesh: Flip Shell Elements"). This was particularly important when the thickness attributed to a shell was not symmetrically distributed.

After all those corrections were done, by selecting the option "Render shell thickness in 3D", it was possible to visualize how the thicknesses of each surface had become distributed and to check if all was as expected. See Figure 50.

The procedure described above had to be performed for every single new simulation, which corresponded to a considerable amount of time spent.

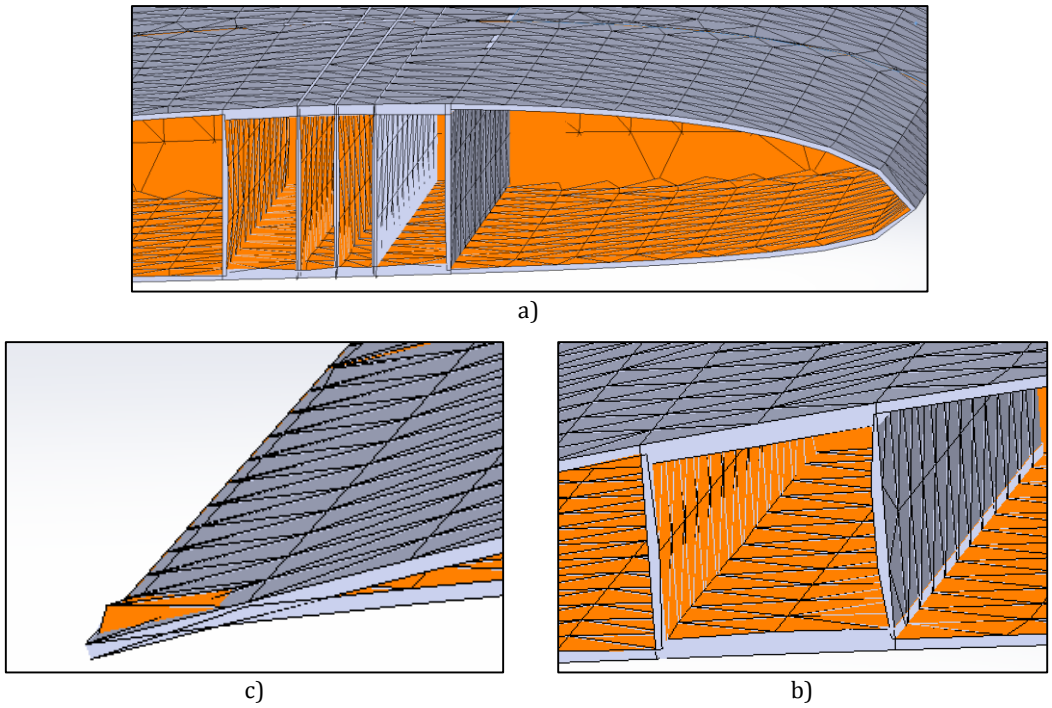

a)

c) b)

Figure 50 – Thicknesses attributed to the components (Rib at the root has been hidden). Grey color represents the Top Surface of the shell; Orange color represents the Bottom Surface of the shell. Detail: a) Leading edge and 1st Spar Caps and Webs; b) 2nd Spar Caps and Webs; c) Trailing edge overlap.

5.2.4 Boundary conditions

The structure was placed under a cantilever boundary condition as follows (see Figure 51):

- The root edges of the both Spars were "fixed"- no rotation and no displacement - in order to simulate the wing attachment to the fuselage (usually to a bulkhead mounted on the interior of the fuselage);
- The outer surface of the Rib at the root ($z = 0$) was put under a "roller-slider" condition in order to simulate the sliding contact between the Rib at the root and the fuselage skin.

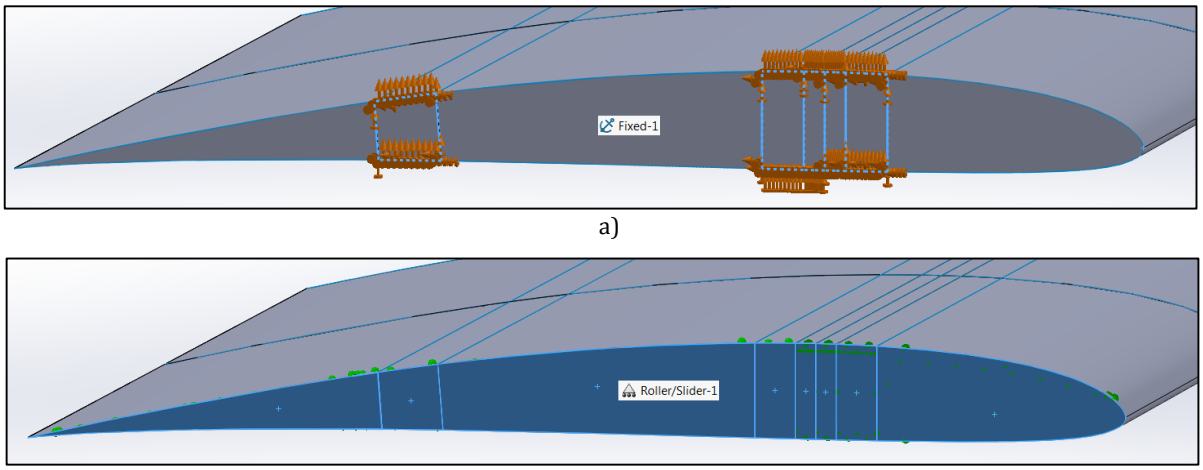

a)

b)

Figure 51 – Cantilever boundary condition.

5.2.5 Forces and Moments

The force $F_{root-cantilever}$ identified in section 3.2.3.2 was applied to the structure via the cantilever boundary condition applied to the root of the wing (in section 5.2.4). The aerodynamic loads, pitching moment, inertial loads and weight, also previously identified in section 3.2.3.2 and further described and calculated in section 3.2.3.3, were applied to the structure as follows (see Figure 52):

- The Lift distribution function was applied on both caps of the 1st Spar in the positive y direction with a total intensity of 6401.5 [N].
- The Pitching Moment distribution function was applied on both caps of the 1st Spar with total negative value of 371.411 [N], using the 1st Spar axis as the reference torsional axis.
- The Payload Body Force of 877.366 [N] was applied to its delimited "attachment area" on the skin in the negative y direction.
- The Motor_1 and Motor_2 Body Forces of 17.5473 [N] were applied to their delimited "attachment area" on the skin in the negative y direction.
- Previously in section 3.2.3.3, the total body force (BF) for the half-wing structure was determined. It consisted of the sum of the weight of the structure and the inertial force for the specific critical condition identified, and was given by:

$$BF_{wing\_structure} = n \cdot W_{wing\_structure}$$

$$BF_{perpendicular\_half-wing} = n_{design} \cdot W_{half-wing\_structure} \cdot \cos(\alpha) \cdot \cos(\Gamma)$$

$$BF_{perpendicular\_half-wing} = a_y \cdot m_{half-wing\_structure}$$

For the "Initial Wing Geometry: Trapezoidal Wing with constant taper and twist; Constant thickness of structural components; and Ribs equally spaced along the wing", its BF distribution was determined based on a prediction of how the weight of the structure might be distributed thus, being a very crude approximation which was also not suitable for optimization purposes since the mass distribution of the structure would vary for each new geometric configuration.

Therefore, since SW allows to apply an acceleration to structure, with a user-defined value and direction, and since material and a thickness had already been attributed to the structure's shells, by applying an acceleration, the software automatically translated it into a body force.

From the previous expression the acceleration in the y direction was calculated:

$$a_y = n_{design} \cdot g \cdot \cos(\alpha) \cdot \cos(\Gamma) = 9 \cdot 9.81 \cdot \cos(6.1) \cdot \cos(2) = 87.737\ [m/s^2].$$

This acceleration was applied to the structure in the y negative (downward) direction, thus replacing the $BF_{perpendicular\_half-wing}$ value and distribution (previously determined in section 3.2.3.3).

It should be noticed that the body forces of neither the payload nor the servo motors could have not been defined using the acceleration "method" because they were not physically (geometrically) represented in the SW model, therefore, what does not have mass cannot be accelerated. These additional "masses" were introduced to the structure directly as additional external forces.

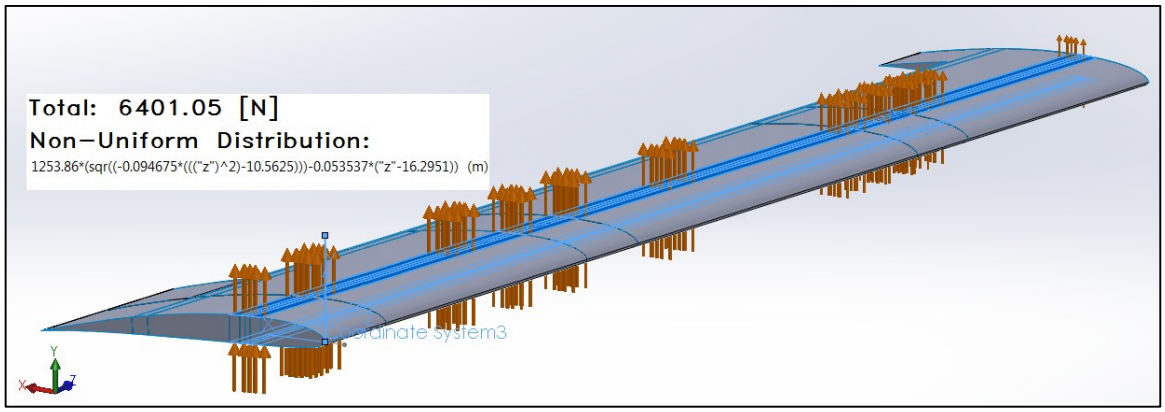

a)

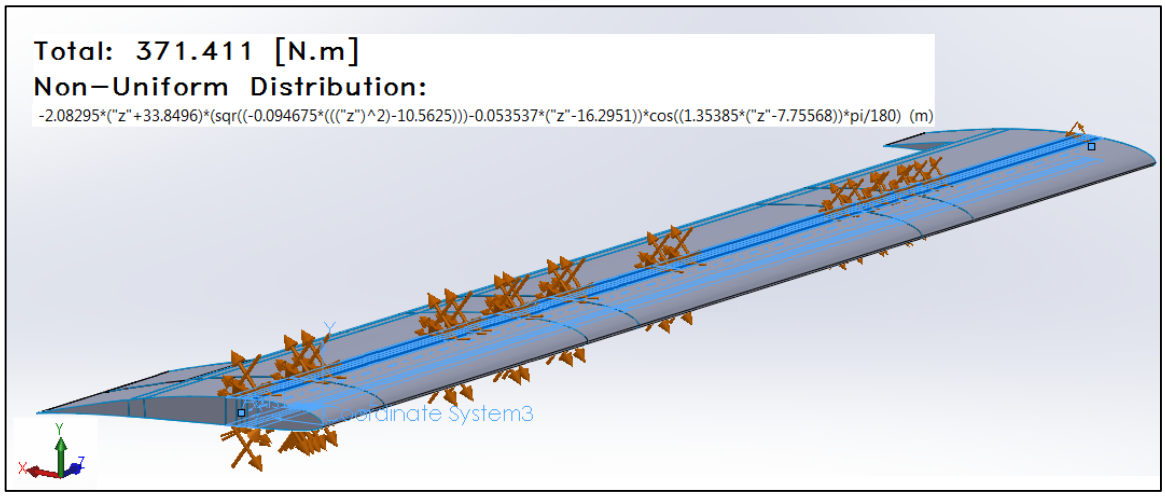

b)

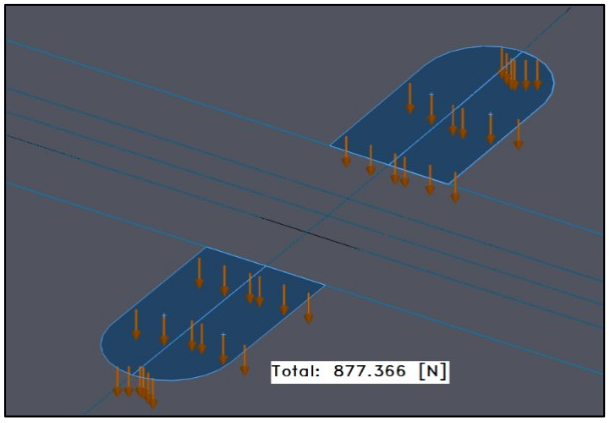

c)

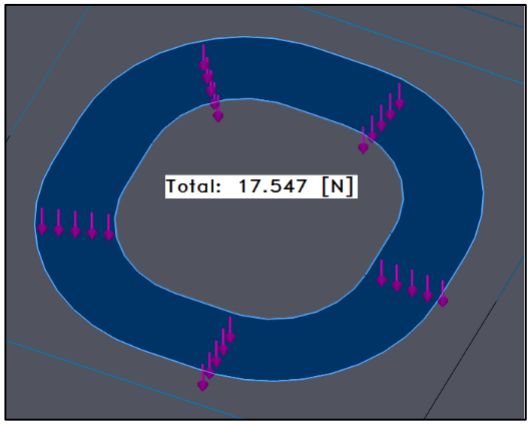

d)

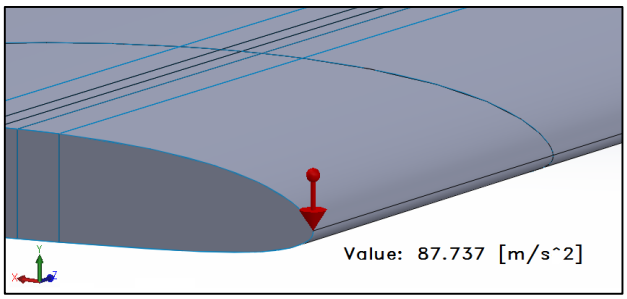

e)

Figure 52 – Forces and Moments applied on the structure: a) Lift; b) Pitching Moment; c) Payload Body Forces; d) Motor 1 or 2 Body Forces; e) Structure’s Acceleration.

5.2.6 Structural Analysis

A structural analysis of the type "Static" was performed and the outputs "Von Mises Stress" and "Displacement" were selected. From these, the maximum stress and maximum displacement were recorded.

The next step consisted of a convergence analysis of the finite elements (FE) size. In order to obtain a large analysis spectrum, the FE size as well as the tolerance were sequentially reduced until they reached such a small value that it became too heavy to compute. See Table 6.

Table 6 – Convergence analysis of the Mesh Parameters of the Simplified Initial Model.

Convergence Analysis							
Standard mesh; Triangular FE; Draft Quality Mesh							
Global FE Size [mm]	100	70	50	40	30	**20**	10
Tolerance [mm]	5.00	3.50	2.50	2.00	1.50	**1.00**	0.50
Max Stress [MPa]	138.9	140.8	155.2	148.8	125.2	**93.06**	112.0
Max Stress Variation relation	-	6.33E+04	7.20E+05	-6.40E+05	-2.36E+06	**-3.21E+06**	1.89E+06
Max Displacement [mm]	324.9	322.3	328	323.9	217.7	**117.3**	48.05
Max Displacement Variation relation	-	-0.09	0.28	-0.41	-10.62	**-10.04**	-6.93
						Convergence Exists	**Heavy to Compute**

Convergence started to exist around the FE size of 40 [mm] with the tolerance of 2 [mm]. Nevertheless, in order to obtain a good mesh for the present "simplified model" as well as for the "final model" where small diameter holes exist, the FE size of 20 [mm] with the tolerance of 1 [mm] was selected – this was the FE size than allowed for the best mesh definition around the small holes (D = 8.33 [mm]), without the mesh becoming "too heavy". See Figure 53.

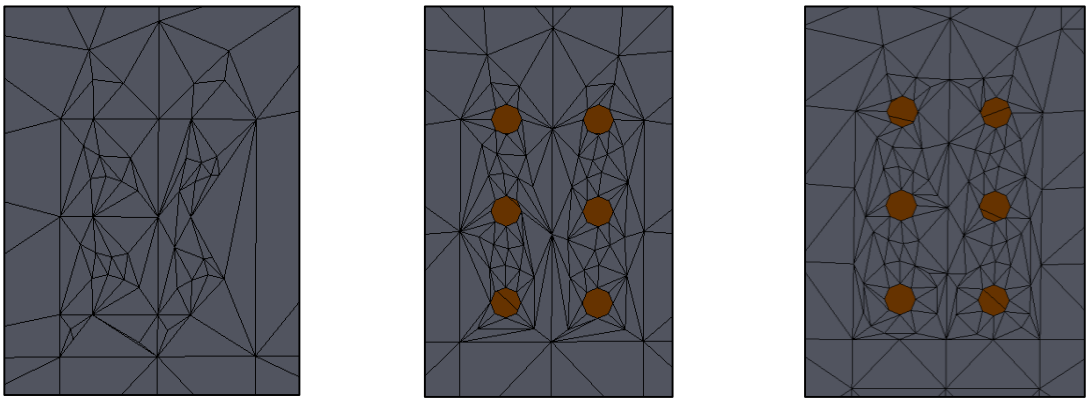

a) b) c)

Figure 53 – Small holes meshed with different FE sizes: a) FE size of 70 [mm], tolerance of 3.5 [mm]; b) FE size of 30 [mm], tolerance of 1.5 [mm]; c) FE size of 20 [mm], tolerance of 1.0 [mm].

For the simplified initial model with the FE size of 20 [mm] and tolerance of 1[mm], the total computational time was approximately 2 minutes. For FE sizes equal or inferior to 10 [mm] the computation became too "heavy" and the time became superior to 6 minutes. In addition, trying to manipulate (zoom in, zoom out, rotate, etc.) the views of the meshed model with such a small FE size became quite impractical since the computer started to "lag" considerably. This manipulation was very important and necessary for

the purpose of verifying if the meshes had all been correctly mapped, and to modify them if needed (as explained in section 5.2.3).

Based on the above, and considering the amount of simulations needed to perform during optimization process, the size of the FE was fixed at 20 [mm] and the tolerance was fixed at 1 [mm] for all the meshes and correspondent simulations from here forth.

Also, maintaining the FE dimensions constant throughout the optimization simulations was crucial because, only by doing so, would it be possible to directly compare the maximum stress and maximum displacement values for every single new geometric configuration of the structure. A change of the FE size would cause an alteration of the stress and displacement values therefore compromising conclusions during the optimization process.

From the simulation of the "Simplified Initial Model" the following maximum Von-Mises stress and maximum displacement values were obtained: $\sigma_{max} = 93.06\ [MPa]$ and $d_{max} = 117.3\ [mm]$. See Figures 54 and 55.

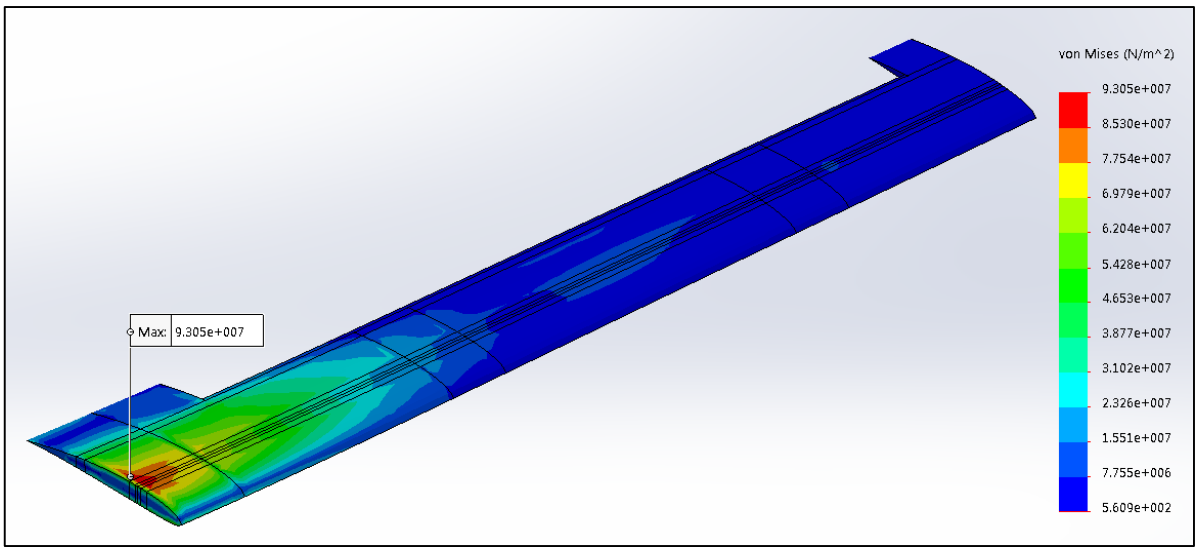

Figure 54 –Von Mises Stresses across all plies. Maximum Stress localized at the wing root.

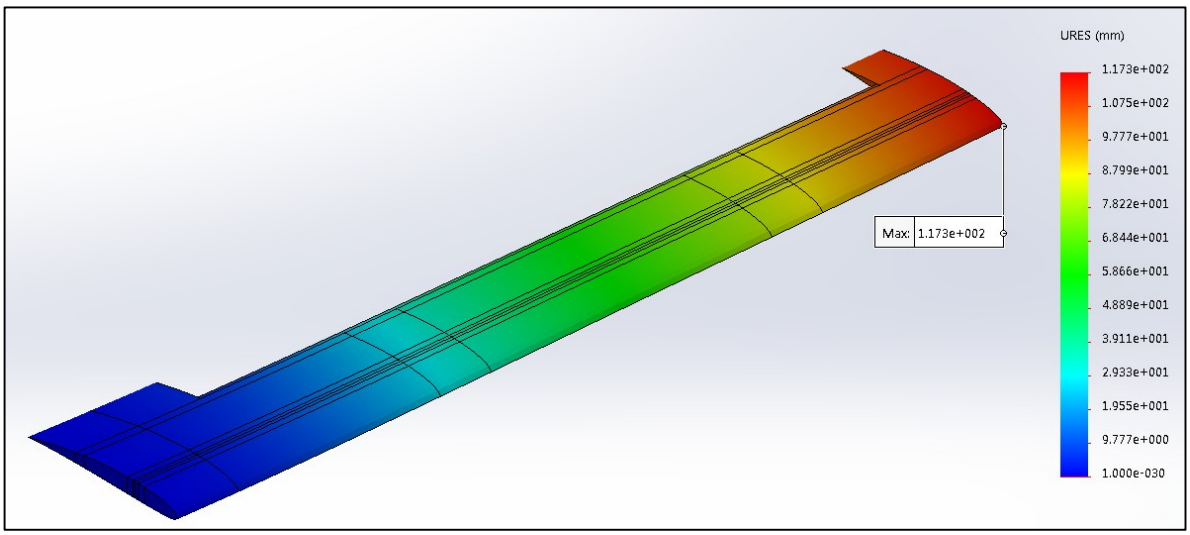

Figure 55 – Wing Displacement. Maximum Displacement localized at the wing tip.

The structural mass was also estimated / calculated in a conservative manner, based on the total surface area, the attributed thicknesses and the material density. The mass of the "Simplified Initial Model" was estimated to be 12.853 [kg]. See Table 16 in Annex 10.

Comparing the obtained values with the structural and mass requirements set for the wing, it was concluded that the Simplified Initial Model satisfied all the structural requirements in terms of strength and stiffness however, in terms of mass, knowing that the UAVision's estimation for the half-wing total mass also includes the flap and the aileron, the final mass of the present half-wing model would be higher than the target value:

- $\sigma_{max} = 93.06\ [MPa] < 570.0$ [MPa] - Ultimate (and yield) compressive strength in x (0º) of the material Epoxy + Bi CF [$C_{10}^{0º}$];
- $d_{max} = 117.3\ [mm] < 162.5$ [mm] - Structural stiffness requirement stated that the wing tip displacement should be inferior to 5% of the wing's half span; (See structural stiffness importance in section 4.1);
- $mass_{simplified\ model} = 12.853\ [kg] \rightarrow mass_{half-wing} > 13.1$ [kg] - UAVision's mass estimation for the half-wing.

As mentioned previously, one of the main goals when designing an aircraft structure is to minimize its weight. There are two main reasons for this:

- The direct and immediate reduction of the manufacturing and material acquisition costs due to the use of less material;
- The indirect, but much more important in the long run, reduction of the aircraft's fuel consumption which translates into a reduction of operational costs and the increase of the operational range and also the increase of the payload that the aircraft can carry.

Therefore, in order to significantly reduce the mass of the structure while guaranteeing the fulfillment of the structural requirements, an optimization process was undertaken.

5.3 Wing Structure Optimization

As mentioned previously, the objective of the current optimization was to reduce, as much as possible, the mass of the wing structure while respecting the structural requirements.

For a same geometry, by lowering the mass of all components in an equal manner, the structure's maximum stress value will increase until it reaches the material's limit stress (in this case 570 [MPa] - compression).

By optimizing the geometry of a structure, it is possible to reduce the initial maximum stress thus, allowing to reduce the mass further than before, until the limit stress is reached.

For a complex structure such as this, in which components are all interconnected, if the geometry of one is changed the mechanical response of all others will also change.

Also, because each component of a wing has a well-defined structural purpose (see section 4.3), the order in which each component is optimized was considered to be relevant. With this in mind, the order in which each component was optimized was decided based on where forces were applied to the structure and how each component resisted and transferred those forces to other components.

Therefore, a "chain top-down" approach was created and used in order to optimize the structure by individually optimizing each component in the following order (from first to last): Skin, 1st Spar, 2nd Spar, Ribs. - "Chain" because the optimization of each component was conducted over each new structural geometry, resulting from the optimization of the previous component. - "Top–down" due to the order in which the components were optimized, which followed the same path as the forces when applied to this structure: Forces applied to the skin, directly transmitted to the 1st Spar (main structural component), at the same time also transmitted to the 2nd Spar and, finally, redistributed by the Ribs, between components. It should be noticed that Ribs also play a very important role in reinforcing the Skin, however, because of having a "reinforcement" role they were the last components to be optimized.

The chain top-down approach could be described as a "hierarchic decomposition method" and it was inspired by the logic behind the "topological optimization method" - which uses stress lines as the guides for the shape optimization of a given material volume (see section 1.5).

The optimization process consisted of four main steps:

Step 1:

- Definition of the best cross-section geometric configuration for each component, which minimized the structure's maximum stress (σ_{max}).

  Restrictions:

  - Components' locations maintained;
  - Components with constant thickness throughout the span;
  - Components' mass kept constant.

  The constant mass restriction was essential in order to allow for the direct comparison between geometric configurations, in terms of maximum stress (σ_{max}) and maximum displacement (d_{max}), thus allowing to conduct the optimization process in a logical manner. The only exceptions were: the case of the Skin where an additional foam material was introduced to its core therefore, increasing its mass, and the case of the Ribs, where the geometry was simplified by removing material and by adding the necessary holes.

Step 2:

- Definition of each component's mass relevance for the minimization of the σ_{max}.

Step 3:

- Redistribution and minimization of the total mass of the structure. Restrictions:
  - Fulfillment of the structural requirements;
  - Feasibility of manufacturing – one of the factors being the material's minimum possible thickness.

Step 4:

- Reintroduction of the Skin holes and cut-outs and dimensioning of their reinforcements;
- Study of the possibility of replacing materials in order to further reduce the structure's total mass;
- Reintroduction of the root extension;

5.3.1 Step 1

Using the "chain top-down" approach the best geometric configuration - which minimized the structure's maximum stress (σ_{max}) – was determined for the Skin, 1st Spar, 2nd Spar and Ribs. For each component, the best configuration was selected from among various others and was highlighted with the color green, in the Tables 7-10 as follows:

Skin cross-section geometry:

Table 7 – Skin Cross-Section Geometry Evaluation.

Skin Cross-Section Geometric Configuration	σ_{max} [MPa]	d_{max} [mm]	$mass$ [kg]	Evaluation
Wing skin solid ("simplified initial model") – no foam core.	**93.06**	117.3	**12.853**	-
Wing skin with core – Airex C70.75 foam core (3 [mm]) for all the skin.	71.41	31.01	13.717	Not Possible*
Wing skin with core "corrected" – no foam core on the sections of the skin above the Caps.	104.5	**106.3**	13.530	Increased stiffness

* Because foam was also placed in the sections of the skin above the caps, high stress values were observed in the foam and those surpassed its strength (1.45 [MPa] – Airex C70.75 compressive strength), therefore, the structure would fail - configuration not possible! See Figure 56.

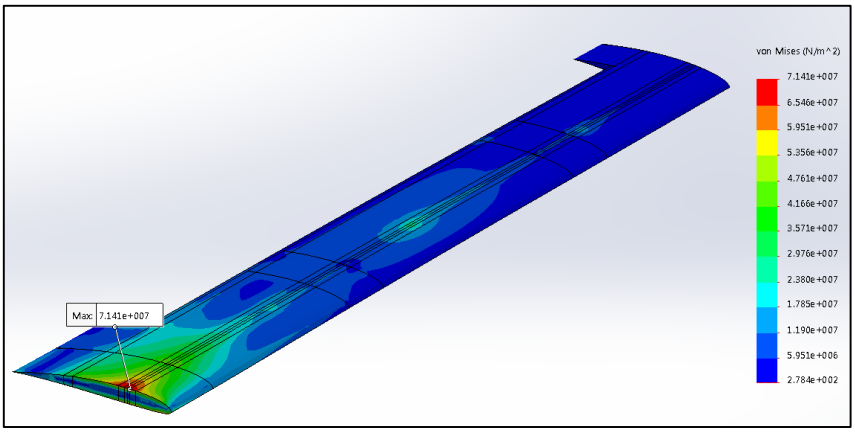

a)

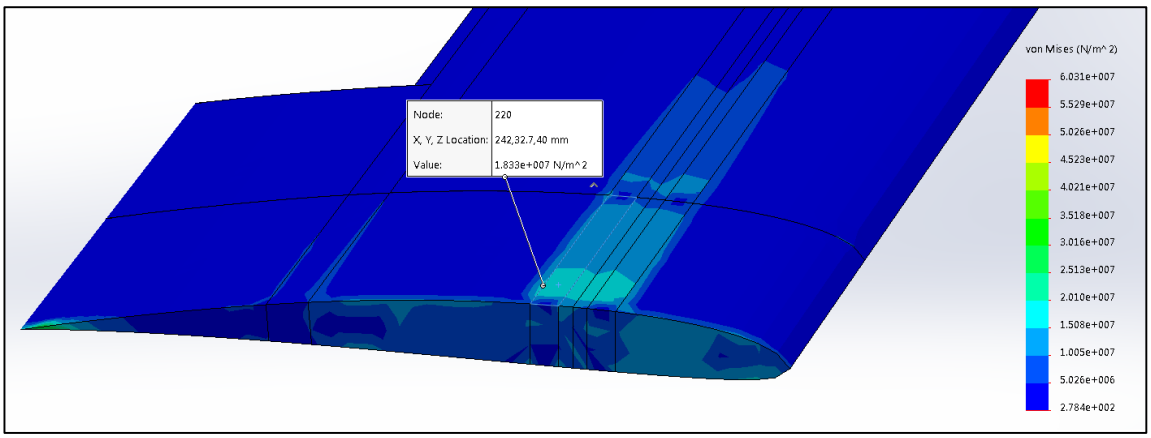

b)

Figure 56 - Wing skin with core – Airex C70.75 foam core (3 [mm]) for all the skin: a) Von Mises maximum stress across all plies; b) Von Mises maximum stress for the 2nd Ply. Note: skin laminate configuration: 1 ply CF (0.95 [mm]) / 1 Ply Foam (3 [mm]) / 1 ply CF (0.95 [mm]).

By removing the foam core from skin areas above the Spars' Caps, the foam's maximum stress problem was solved, see Figure 57. It should be noticed that the high stresses that can be observed in the transition areas (transition from skin without foam to skin with foam or vice-versa) would not be a problem since, during manufacturing, those transitions would be accomplished by a slope with an angle < 45º thus, successfully reducing the stress values in the foam to acceptable ones.

Nevertheless, because the "corrected" foam solution did not favor the maximum stress reduction, no foam would be added to the skin at this point. However, later on (in section 5.3.3 – Step 3), its use would be needed in order to increase the skin planar rigidity due to its low thickness.

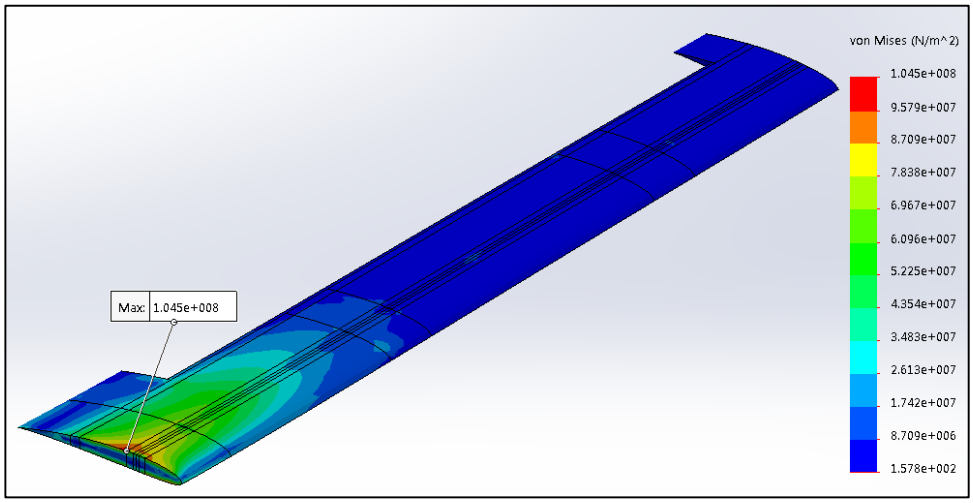

a)

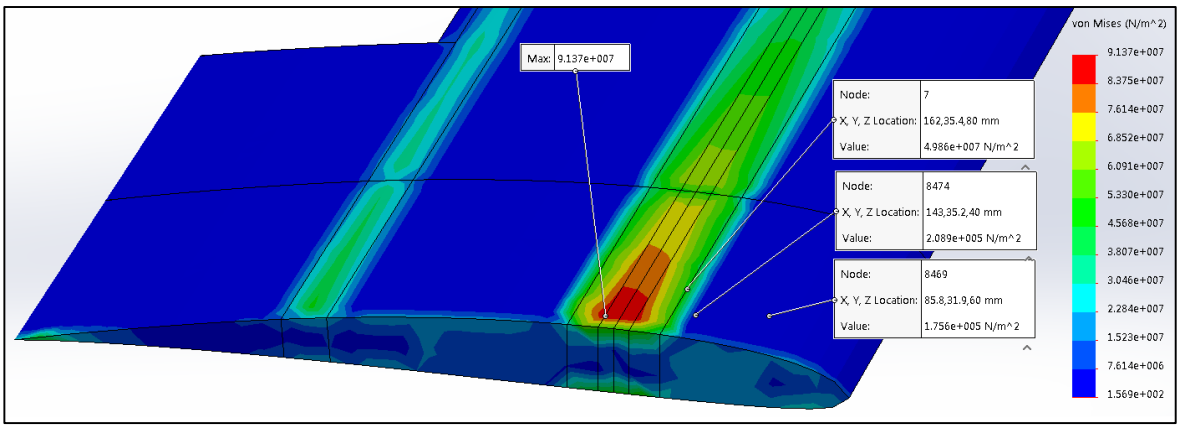

b)

Figure 57 - Wing skin with core "corrected" – no foam core on the sections of the skin above the Caps: a) Von Mises maximum stress across all plies; b) Von Mises maximum stress and other probed stresses for the 2nd Ply. Note: skin laminate configuration: Over the Caps: 2 plies CF (0.95 [mm]); other areas: 1 ply CF (0.95 [mm]) / 1 Ply Foam (3 [mm]) / 1 ply CF (0.95 [mm]).

1st Spar cross-section geometry:

Table 8 – 1st Spar Cross-Section Geometry Evaluation.

1st Spar Cross-Section Geometric Configuration	σ_{max} **[MPa]**	d_{max} **[mm]**	$mass$ **[kg]**	**Evaluation Rank #**
Wing skin solid + 1st Spar IIIII - "simplified initial model"	93.06	117.3	12.853	3rd
Wing skin solid + 1st Spar IIII	94.19	107.9	12.853	4th

Wing skin solid + 1st Spar III configuration 1	**80.52**	**72.67**	**12.853**	**1st**
Wing skin solid + 1st Spar III configuration 2	101.3	121.8	12.853	6th
Wing skin solid + 1st Spar II configuration 1 (pi)	88.22	82.53	12.853	2nd
Wing skin solid + 1st Spar II configuration 2 (box)	114.0	183.1	12.853	Not Possible*
Wing skin solid + 1st Spar II configuration 3 (cc-inverted)	102.8	124.2	12.853	5th
Wing skin solid + 1st Spar II configuration 4 (cc)	110.4	138.4	12.853	7th
Wing skin solid + 1st Spar I configuration 1 (I)	125.1	146.7	12.853	8th
Wing skin solid + 1st Spar I configuration 2 (c-inverted)	120.4	198.5	12.853	Not Possible*
Wing skin solid + 1st Spar I configuration 3 (c)	139.5	247.8	12.853	Not Possible*
Wing skin solid + 1st Spar III configuration 1 with Feasible Configuration (Thickness per Web = 3.04 [mm])	**82.05**	**76.14**	**12.771**	-

* Maximum displacement condition in not respected (d_{limit} = 162.5 [mm]).

Figure 58 shows all the 1st Spar configurations that were evaluated.

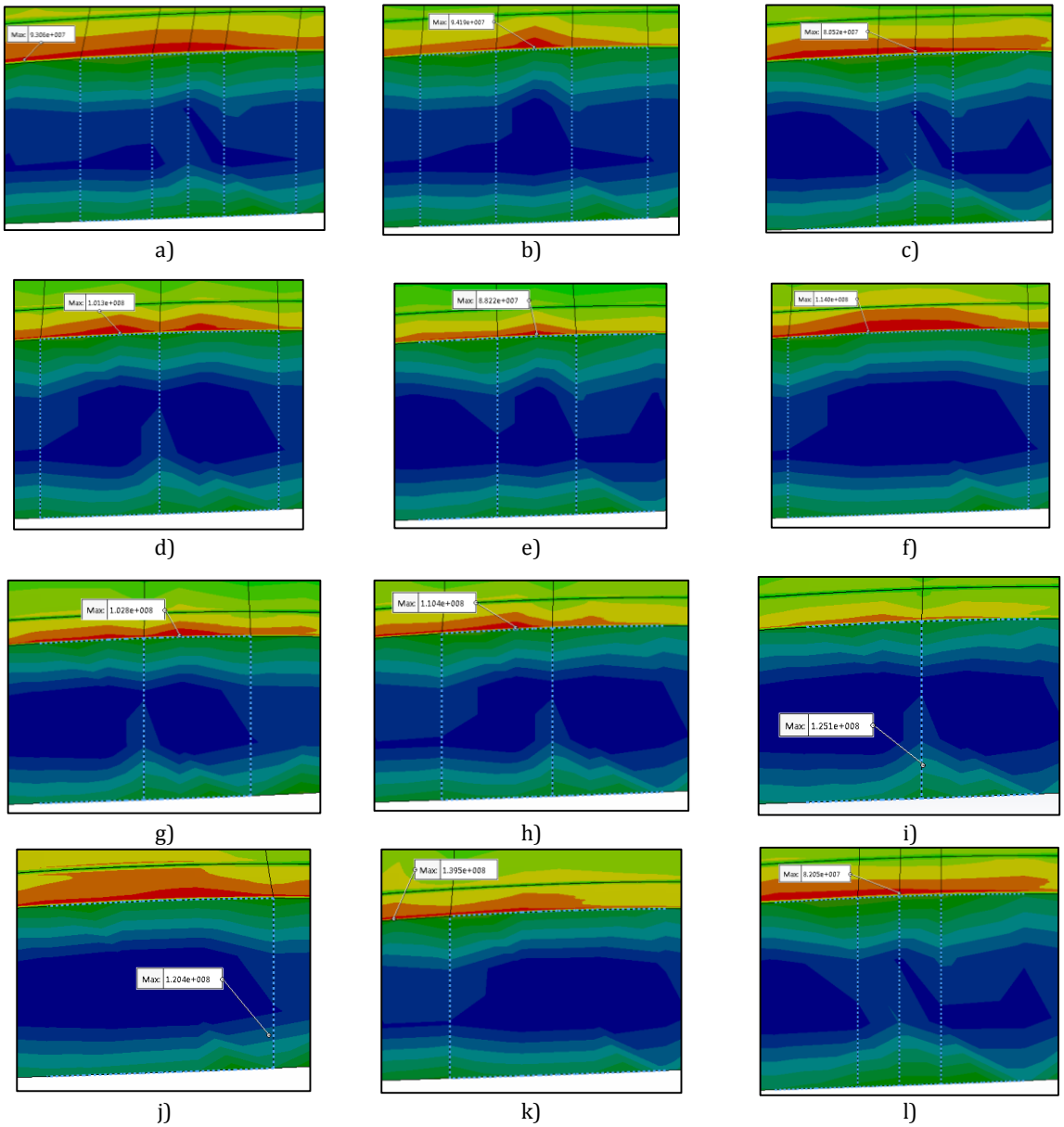

Figure 58 - 1st Spar Cross-Section Geometric Configurations: a) IIIII; b) IIII; c) III config. 1; d) III config. 2; e) II config. 1 (pi); f) II config. 2 (box); g) II config. 3 (cc-inverted); h) II config. 4 (cc); i) I config. 1 (I); j) I config. 2 (c-inverted); k) I config. 3 (c); l) III config. 1 Feasible Configuration.

2nd Spar cross-section geometry:

Table 9 – 2nd Spar Cross-Section Geometry Evaluation.

2nd Spar Cross-Section Geometric Configuration	**σ_{max} [MPa]**	**d_{max} [mm]**	**$mass$ [kg]**	**Evaluation Rank #**
Wing skin solid + 1st Spar III configuration 1 (FC) + 2nd Spar II (box) - initial	**82.05**	**76.14**	**12.771**	**1st**
Wing skin solid + 1st Spar III configuration 1 (FC) + 2nd Spar I (c)	82.91	77.17	12.771	2nd

Figure 59 shows the two 2nd Spar configurations that were evaluated.

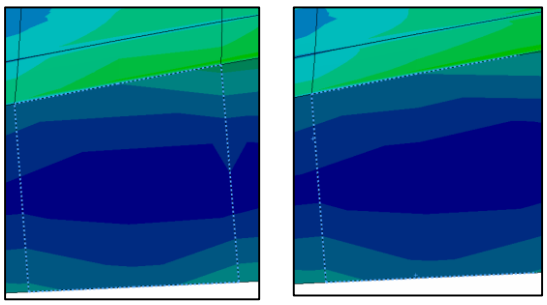

a) b)

Figure 59 - 2nd Spar Cross-Section Geometric Configurations: a) II (box); b) I (c).

Ribs cross-section geometry:

Table 10 – Ribs Cross-Section Geometry Evaluation.

Ribs Cross-Section Geometric Configuration	**σ_{max} [MPa]**	**d_{max} [mm]**	**$mass$ [kg]**
Wing skin solid + 1st Spar III configuration 1 (FC) + 2nd Spar II (box) + Ribs - initial	82.05	76.14	12.771
Wing skin solid + 1st Spar III configuration 1 (FC) + 2nd Spar II (box) + Ribs with necessary holes	**82.30**	**76.27**	12.763
Wing skin solid + 1st Spar III configuration 1 (FC) + 2nd Spar II (box) + Ribs with holes and simplified geometry	82.47	76.65	**12.717**

Even though the simplified Rib geometry slightly increased both the stress and displacement maximum values, it was successful at reducing the mass which has greater importance. Also, by introducing this simplification, the manufacturing and assembly processes would be greatly simplified thus reducing time and costs. See Figure 60.

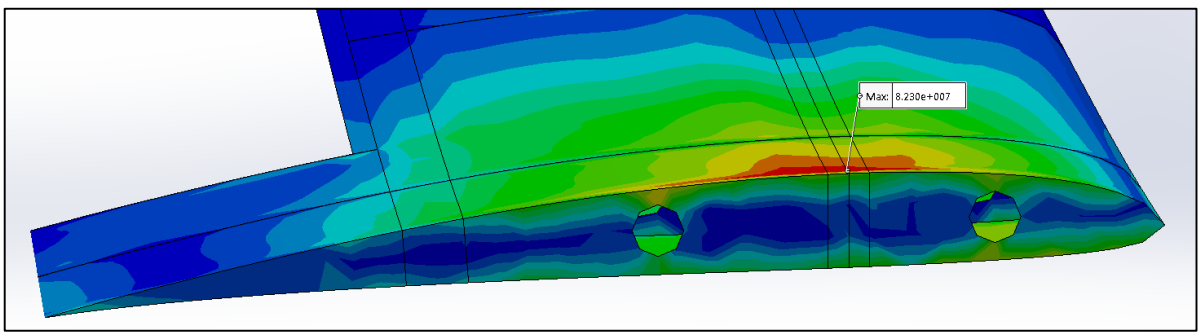

a)

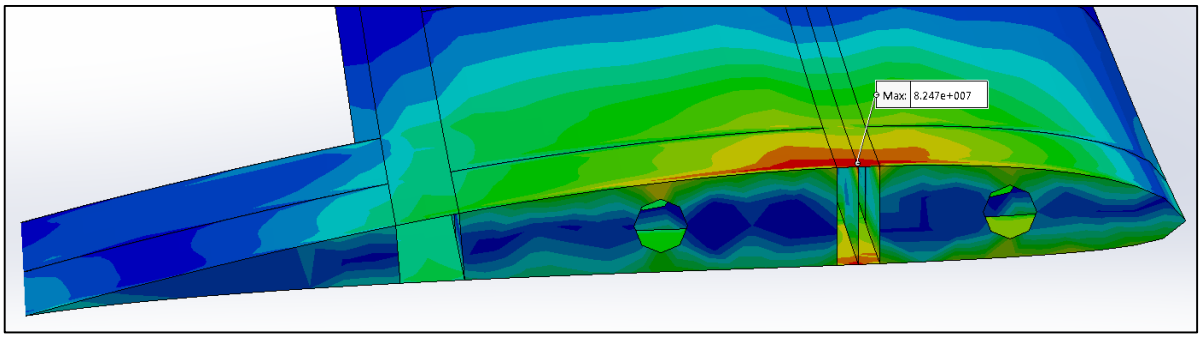

b)

Figure 60 - Ribs Cross-Section Geometric Configurations: a) Necessary holes; b) Necessary holes and simplified geometry.

5.3.2 Step 2

From Step 1 the resulting geometric configuration consisted of: "Wing skin solid + 1st Spar III configuration 1 (FC) + 2nd Spar II (box) + Ribs with holes and simplified geometry" and its mechanical and mass characteristics were: $\sigma_{max} = 82.47\ [MPa]$, $d_{max} = 76.65\ [mm]$ and $mass = 12.717\ [kg]$.

In order determine each component's mass relevance for the minimization of the σ_{max}, the masses of the Skin, 1st Spar Caps, 1st Spar Webs, 2nd Spar Caps, 2nd Spar Webs and Ribs, were individually increased 5% over the total structure's mass – final structural mass of 105% - and, for each of those, a new simulation was run (6 in total). From those six simulations, the structure's maximum stress and maximum displacement values were recorded and their difference calculated in relation to the initial model.

Each component's importance was determined by dividing their "stress variation" by the sum of "stress variation" of all components. This way, the sum of the "importance" of all components was equal to 1 (100%), see Table 11.

Table 11 – Components Importance Definition.

	Max Stress [MPa]	Max Displacement [mm]
Initial	**82.47**	**76.65**

Component mass variation (+ 5%)	Max Stress [MPa]	Stress Variation	Component importance	Max Displacement [mm]	Displacement Variation
Skin	79.92	-2.55	**0.074801995**	75.1	-1.57
1st_spar_caps	64.51	-17.96	**0.526840716**	42.3	-34.34
1st_spar_webs	76.20	-6.27	**0.183924905**	66.2	-10.45
2nd_spar_caps	79.67	-2.80	**0.082135524**	69.1	-7.51
2nd_spar_webs	80.08	-2.39	**0.070108536**	72.4	-4.22
Ribs	80.35	-2.12	**0.062188325**	73.6	-3.02
TOTAL		-34.09	**1**		

By multiplying a component's importance by the total mass of the structure (100%) it was then possible to determine how much mass should be attributed to that component.

Since the geometry of all the components had already been defined, their new thicknesses were obtained by diving their attributed masses by their respective surface areas. The new thicknesses were then

introduced into the previous geometric model and a new simulation was run and the following maximum stress and displacement values were obtained: $\sigma_{max} = 70.17\ [MPa]$ and $d_{max} = 14.42\ [mm]$.

Nevertheless, a slight Skin buckling was observed. See Figure 61. This material failure would be dealt with in Step 3. This buckling was caused by a combination between the point loads (payload / servo motors) and the compression loads on the bottom skin due to a slight wing deflection in the positive x axis direction.

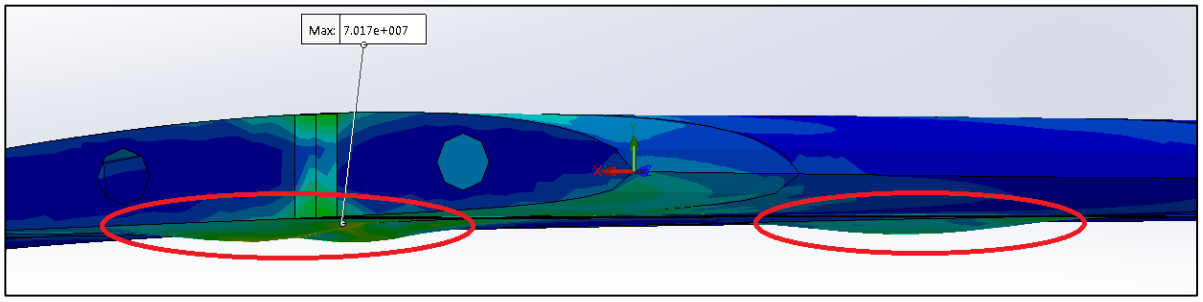

Figure 61 – Skin failure due to its reduced thickness (only 0.226 [mm]).

5.3.3 Step 3

Using the new mass distribution based on the determined component's importance, six new simulations were performed for six different structure's mass values: 2.5, 5, 6, 7.5, 10 and 12.5 [kg]. From these, the maximum stress and maximum displacement values were recorded and two graphs were created: Max Stress vs Mass and Max Displacement Vs Mass. See Figure 62.

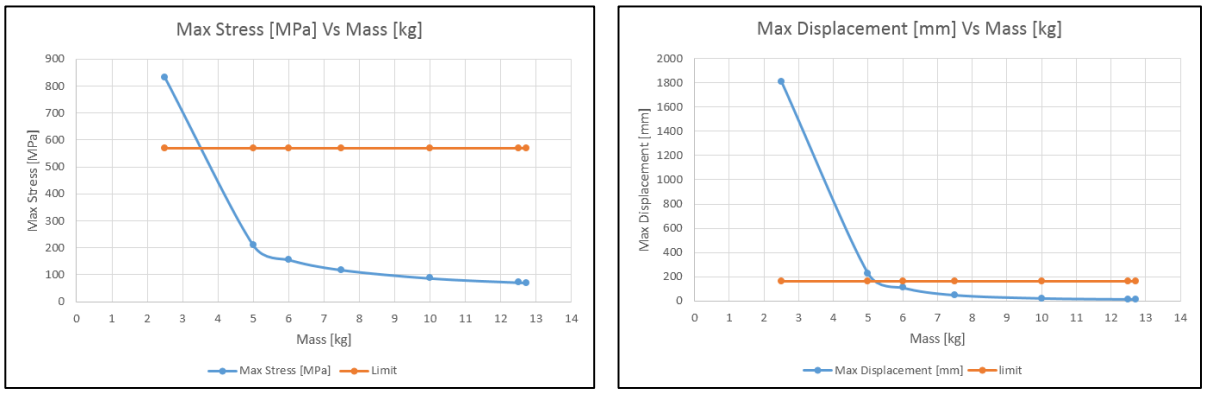

a) b)

Figure 62 – a) Graph: Maximum Stress [MPa] Vs Mass [kg]; b) Graph: Maximum Displacement [MPa] Vs Mass [kg];

From these, it was possible to approximately determine the structure's minimum mass that still fulfilled the structural requirements: ≈ 6 [kg]. This mass value was limited by the maximum wing tip displacement (162.5 [mm]) instead of the maximum stress (570 [MPa]).

It should be noticed that skin buckling was observed in all the simulations however, it was assumed that it would not significantly affect the conclusions obtained from the graphs.

The thicknesses of each of the components and sub components was then corrected in order for the manufacturing of the structure to be feasible (feasible number of plies). Also, in order to eliminate the Skin buckling, a 3 [mm] ply of Airex C70.75 foam was introduced as core to the Skin, except in sections above the Caps (best practice as concluded in section 5.3.1).

The corrected geometric configuration presented the following characteristics: $\sigma_{max} = 133.3\ [MPa]$, $d_{max} = 99.86\ [mm]$ and $mass = 7.567\ [kg]$.

It should be noticed that in order for the "corrected model" to be created, the mass percentage attributed to each component had to be slightly modified and this lead to the increase of the resulting structural mass. Because the obtained mass ($7.567\ [kg]$) could not be further reduced without also further changing the mass distribution, the "corrected model" was the geometric configuration used for the next optimization step.

It should also be noticed that the σ_{max} in any of the foam plies across the structure was less than 1.45 [MPa] (Airex compressive strength, see section 4.6.1) therefore, no damage would occur in any foam core.

5.3.4 Step 4

- Reintroduction of the Skin holes and cut-outs and dimensioning of their reinforcements:

The holes and the cut-outs were reopened and their respective reinforcements were dimensioned keeping in mind how these would interact with other components as well as their manufacturing and or assembly processes:

- The payload reinforcement was incorporated into the 1st spar lower cap, becoming part of it – as recommended in section 4.3;
- Each servo motor reinforcement was embedded into the bottom wing skin. The skin foam core in each "motor attachment area" was replaced by a solid stack of Bi CF. The number of plies attributed to the reinforcement was such as to approximate, as best as possible, the thickness of the reinforcement to the thickness of the foam in order to facilitate the skin lamination, minimizing fiber deformations (bulges or depressions), stress concentration and / or delamination problems.

It should be noted that bolted connections on sandwich materials with a foam core usually suffer damage due to the collapse of the foam – same situation that happened when trying to fix foam core specimens to the grips of the test machine. Therefore, the reinforcements were designed in such a way that they would be able to effectively support high compression loads due the bolted connections by being constituted by solid stacks of Bi CF and with fibers oriented perpendicularly to the load direction in order to maximize the composite strength.

At this point the wing model had the following characteristics: $\sigma_{max} = 132.8\ [MPa]$, $d_{max} = 99.75\ [mm]$, $mass = 7{,}697\ [kg]$.

- Study of the possibility of replacing materials in order to further reduce the structure's total mass:

Wanting to further reduce the mass of the structure, the effect of replacing two plies of Bi CF material by one ply of Uni CF in each of the 1st spar caps was studied. The replacement ply was placed in the center of the lamination stack in order to maintain the laminate's symmetry. From this substitution: $\sigma_{max} = 257.7\ [MPa]$, $d_{max} = 106.8\ [mm]$, $mass = 7.627\ [kg]$.

The replacement resulted in a mass reduction of only 72 [g] and the wing tip displacement was not maintained (the Uni CF E1 was more than double the Bi CF E1 however, it did not prove to be enough for

the structure's stiffness to be maintained). The increase of the maximum stress was expected since the cross section area was reduced ($\sigma = F/A$).

Considering that the $mass$ reduction was minimal compared to the significant increase of the σ_{max} and the slight increase of the d_{max}, associated to an additional increase in the complexity of the manufacturing process due to the introduction of a new material, it was decided not to perform this material replacement.

Regarding the 2nd spar, no replacement was possible because of laminate configuration reasons: For the webs, no unidirectional material should be used due to the direction of the stresses that occur there (see section 4.3.1). Therefore, because there were 8 plies in each cap and 7 plies in each web, 7 of the 8 plies that make up the web are also the same plies that make up the caps, therefore, no replacement of Bi by Uni can be performed for the caps without weakening the webs (of the 2nd spar).

- Reintroduction of the root extension:

Last but not least, the root extensions of the 1st and 2nd Spars were reintroduced (250 and 100 [mm], respectively) and the root boundary conditions were corrected as follows (see Figure 63):

- The root surfaces of the both Spars were "fixed"- no rotation and no displacement - in order to simulate the wing attachment to the fuselage;
- The outer surface of the Rib at the root ($z = 0$) was put under a "roller-slider" condition in order to simulate the sliding contact between the Rib at the root and the fuselage skin.

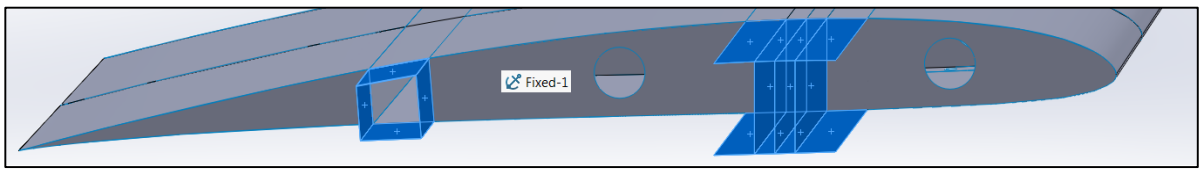

a)

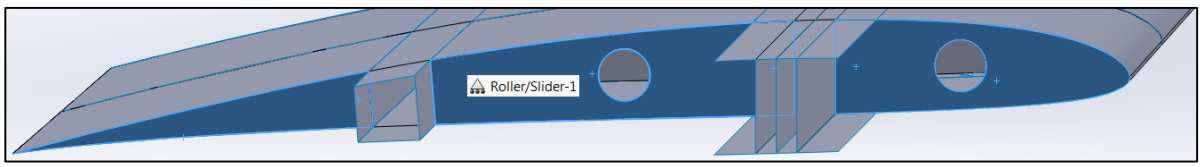

b)

Figure 63 – "Corrected" Cantilever boundary condition.

As mentioned previously, one of the objectives of the geometric simplification, which included the root extension simplification, was to expedite the geometric modification process of the structure. However, it was also mentioned that that the root extension simplification was an approximation.

Therefore, after the wing root extension was reintroduced to the model, the following stress, displacement and mass values were obtained: $\sigma_{max} = 133.3\ [MPa]$, $d_{max} = 100.8\ [mm]$, $mass = 8.106\ [kg]$ - slight increase of all values. Figure 64 a)-f) shows the FEA simulation results for the final geometric configuration of the wing (Global FE size = 20 [mm], Tolerance = 1 [mm]).

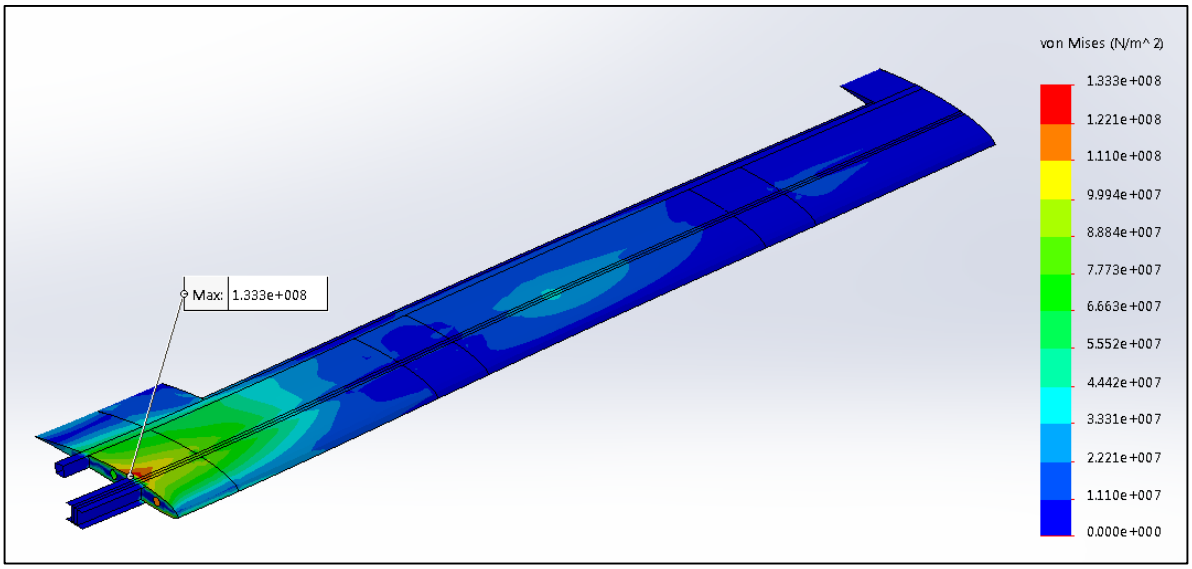
von Mises (N/m^2)
1.333e+008
1.221e+008
1.110e+008
9.994e+007
8.884e+007
7.773e+007
6.663e+007
5.552e+007
4.442e+007
3.331e+007
2.221e+007
1.110e+007
0.000e+000
Max: 1.333e+008

a)

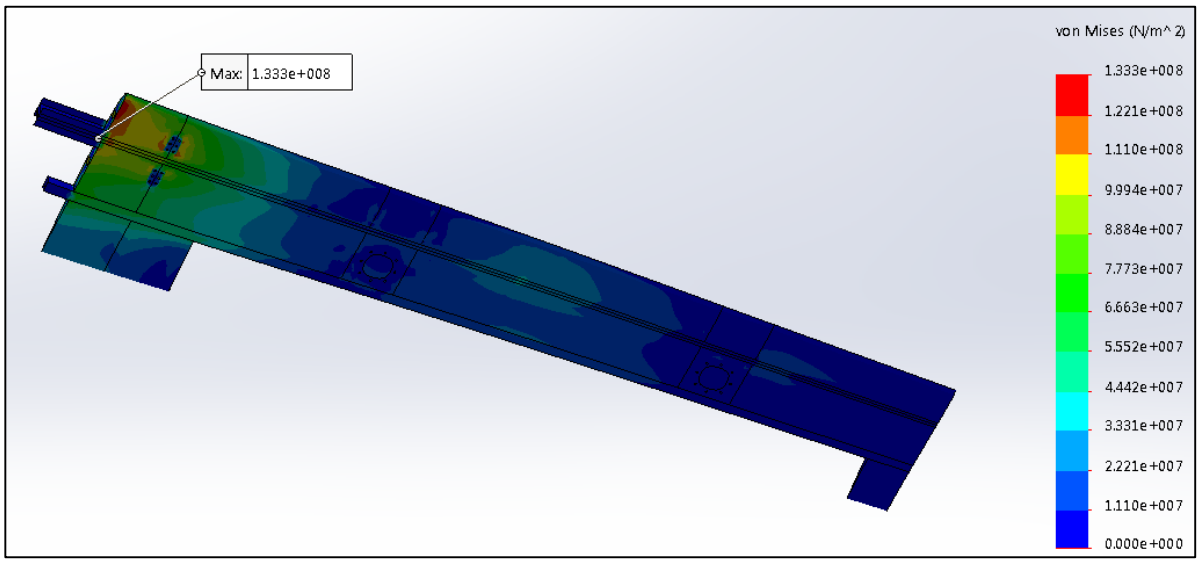
von Mises (N/m^2)
1.333e+008
1.221e+008
1.110e+008
9.994e+007
8.884e+007
7.773e+007
6.663e+007
5.552e+007
4.442e+007
3.331e+007
2.221e+007
1.110e+007
0.000e+000
Max: 1.333e+008

b)

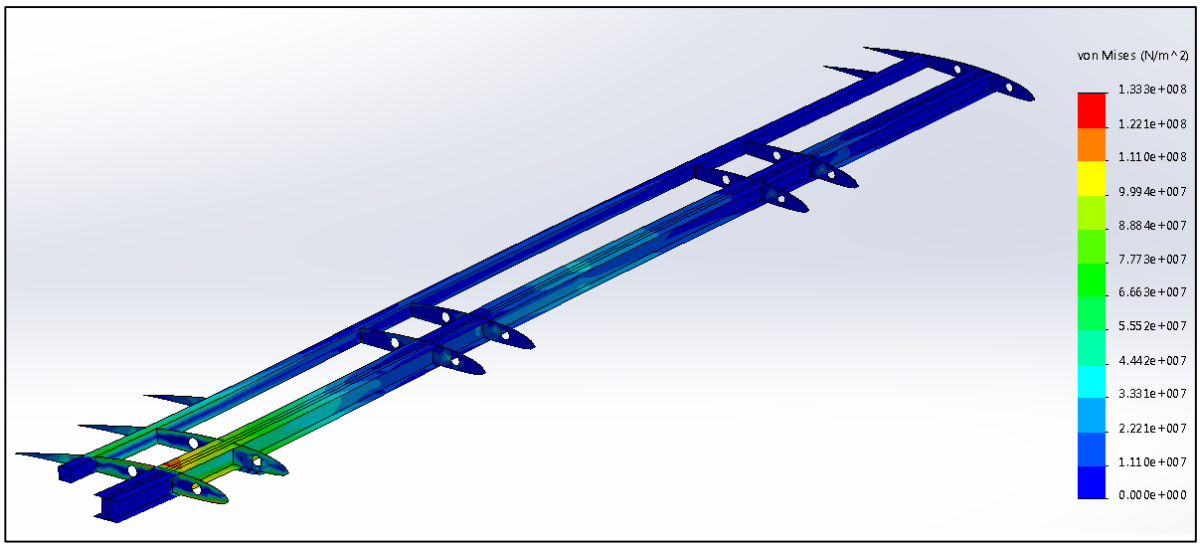
von Mises (N/m^2)
1.333e+008
1.221e+008
1.110e+008
9.994e+007
8.884e+007
7.773e+007
6.663e+007
5.552e+007
4.442e+007
3.331e+007
2.221e+007
1.110e+007
0.000e+000

c)

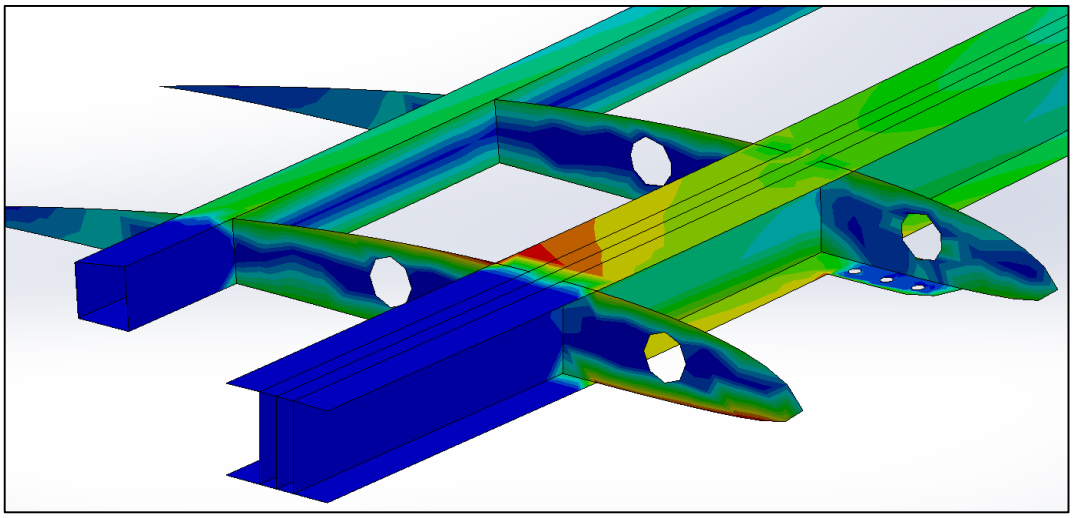

d)

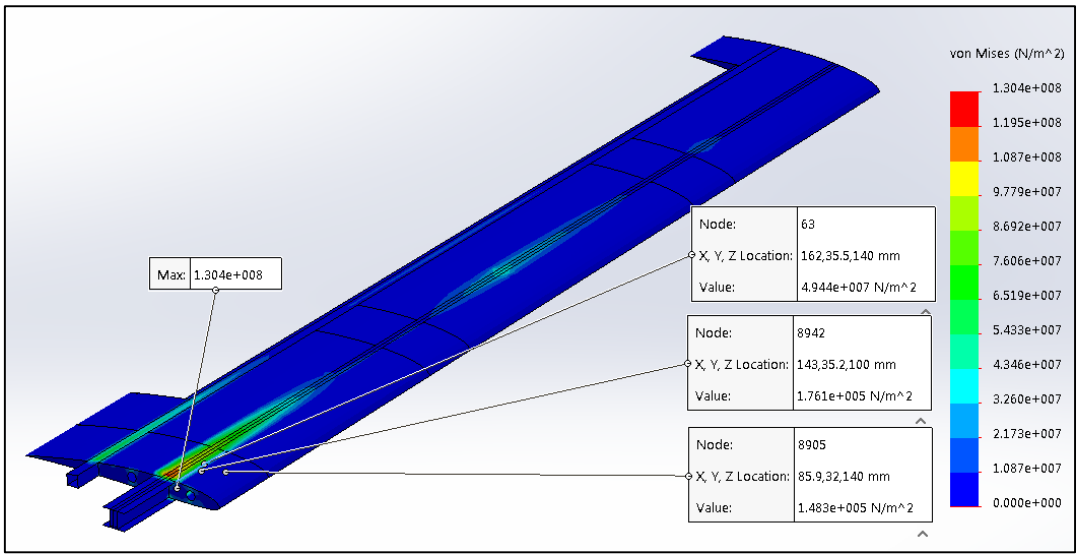

e)

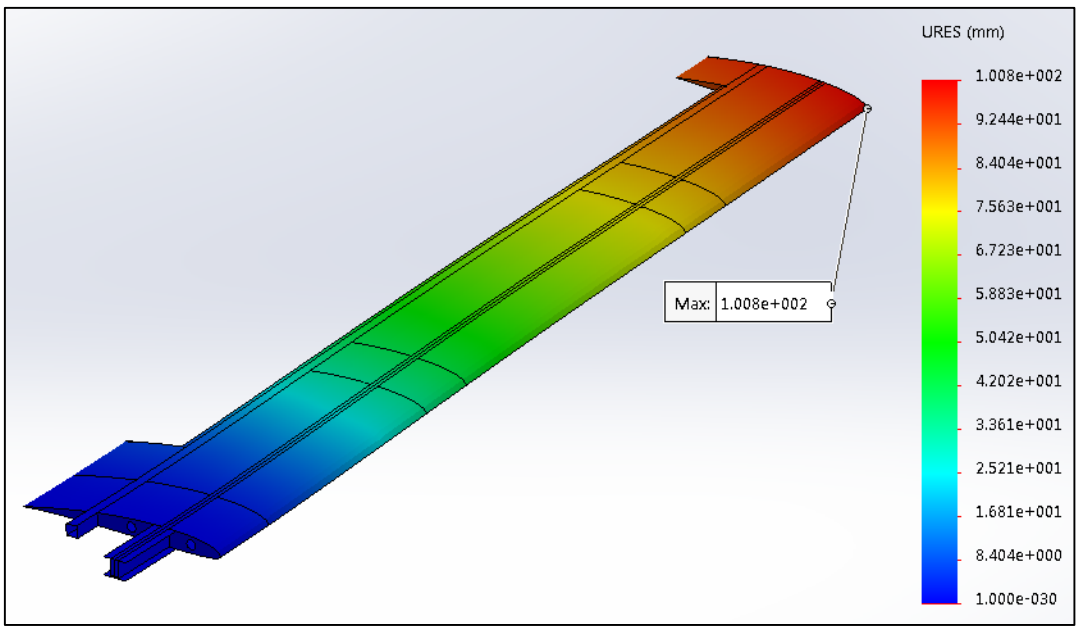

f)

Figure 64 – a), b), c), d) Von Mises Stresses across all plies; e) Von Mises stresses and other probed stresses for the 2nd Ply (foam ply); f) Wing Displacement. Maximum Displacement localized at the wing tip.

6 Wing Final Design including Flaps and Ailerons

The wing structure final design corresponded to the final geometric configuration resultant from the optimization process, and its mass was: $mass = 2\text{x } 8.106$ [kg].

Nevertheless, there was the need to obtain a "complete wing geometric configuration", which included the Flaps and the Ailerons, in order to properly estimate the full mass of the wing, thus allowing to assess if it complied with the mass requirement (< 26.2 [kg]), and to estimate the final construction cost of the complete wing.

Also, to ensure that the mechanical characteristics of the wing final structure are easily and correctly reproduced in a production phase, a detailed "map", of how and where each material should be inserted into the wing, was elaborated.

Last but not least, the structure was also evaluated in terms of its capability to withstand other pertinent loading conditions.

6.1 Wing Final Design and Weight and Cost Estimation

In order to obtain a complete wing geometric configuration, the Flaps and Ailerons structures had to be defined. Based on the premise that they could be considered "scaled down wings" (see section 4.4) their structures were defined as being constituted by: Skin, one Spar and three Ribs, although no structural study was performed for none of them.

The Flaps and Ailerons component's design, thickness and positioning were proposed based on their predictable manufacturing process (see section 4.4), resulting in the following:

- Ribs: same thickness and lamination as the Ribs of the main structure; one placed at the mid-span and one at each end;
- Spar: "C" spar with the same lamination configuration as the 2nd Spar; placed at the Flap or Aileron "leading-edge";
- Skin: Same thickness and lamination as the Skin of the main structure.

The hinged connection between the ailerons and flaps and the main wing structure would be made out of two plies of Kevlar 49 (as explained in section 4.4).

For the assembly of the whole wing, a quantity of Epoxy, equivalent to a ply with a thickness of 0.1 [mm], was estimated (based on the manufacture experience gained from the production of the material's specimens – section 4.6.1) to be necessary in order to glue the various components together.

Adding up the mass contributions of all the wing's components (Skin, Spars and Ribs) and connection agents (Epoxy 0.1 [mm] "ply"), not one but three possible final mass values were obtained for the wing. Those depended on the type of resin impregnation method chosen to be used during the manufacturing process of the Skin - sandwich composite laminate - which would directly affect the amount of resin "trapped" in the foam (Airex C70.75) porous surface.

The Airex C70.75 foam is a closed cell foam, however, its surface cells are not closed, thus allowing for resin to permeate approximately 0.5 [mm] (average) into it. If the foam surfaces are not protected (isolated / sealed), the resin will fill the voids, significantly increasing the mass of the final laminate.

To solve this problem, each of the Skin's Bi CF plies could be pre-impregnate before stacking them onto the lamination mold. This could be achieved by using the Hand-lay-up method or by using "store bought" Prepregs (see section 4.1.1).

As mentioned, when calculating the total mass of wing (using the materials properties determined in section 4.6.1), and determining the wing cost (based on the materials' prices also presented in section 4.6.1), three different results arise, depending on the manufacturing solution adopted:

- If no pre-impregnation is used, an average 0.5 [mm] Epoxy penetration into each surface of the Foam can be considered and the final total mass would be: $mass$ = 2x 12.430 [kg] which corresponds to a 5% mass reduction relative to the UAVision's prediction, and to a wing cost of approximately 2x 1315.70€.
- When using a "store bought" Prepreg (with the same characteristics of the Epoxy + Bi CF), it was assumed (based on experience) that only a negligible amount of Epoxy penetration would exist, and the wing final mass was estimated to be: $mass$ = 2x 9.035 [kg], corresponding to a reduction of 31% relative to the UAVision's prediction, and to a wing cost of approximately 2x 1451.68€.
- For the situation where each ply of Bi CF would be pre-impregnated with Epoxy by hand-lay-up before being placed onto the stack, the final total mass was assumed to correspond to an intermediate value of the above: $mass \approx$ 2x 10.732 [kg], which would correspond to an 18% reduction relative to the UAVision's prediction, and to a wing cost of approximately 2x 1107.12€. However this last result is only an estimated and will strongly depend on the manufacture process.

Regarding the structural simulations, it should be explained that they were all performed considering that no Epoxy penetration existed, which is the most conservative case in terms d_{max} and σ_{max}. For the other cases, the increase in mass would lead to an increase of the wing stiffness therefore, directly decreasing the d_{max} and consequently increasing the body forces that act contrarily to the lift thus, further decreasing the d_{max} and slightly decreasing the σ_{max}. In other words, for any of the impregnation methods, the values: $\sigma_{max} = 133.3\ [MPa]$ and $d_{max} = 100.8\ [mm]$, would never be exceeded.

6.2 Wing Final Design, Characteristics Summary

The final wing structure satisfied all structural, mass and operational requirements imposed:

- Capable of enduring: 4 and -1.5 G's;
- $\sigma_{max} = 133.3\ [MPa]$ < 570.0 [MPa] - Ultimate (and yield) compressive strength in x (0º) of the material Epoxy + Bi CF [$C_{10}^{0º}$];
- $\sigma_{\max\_foam\ plies} \approx 1 <$ 1.45 [MPa] – Airex C70.75 compressive strength. Also, $\sigma_{\text{average}\_foam\ plies} \approx$ 0.15 [MPa];
- $d_{max} = 100.8\ [mm]$ < 162.5 [mm] - Structural stiffness requirement stated that the wing tip displacement should be inferior to 5% of the wing's half span (3250 [mm]); (See structural stiffness importance in section 4.1);
- $mass_{wing}$ = 18.07 / 21.464 / 24.86 < 26.2 [kg] - UAVision's weight estimation for the full wing.

- Each half-wing capable of carrying up to 10 [kg] of suspended payload;
- Materials used (composite materials) capable of enduring high salinity environments without suffering corrosion problems;
- Long service life is expected due to the large margin between the working stress and the maximum (design) stress.

How much the initial predicted mass of 26.2 [kg] was reduced, depended on the impregnation method used on the Skin: 31% (Prepreg); 18% (Pre-impregnation by hand-lay-up) or 5% (Hand-lay-up).

The lowest manufacturing cost, based solely on material costs, corresponded to the Pre-impregnation: 2x 1107.12€, followed by the Hand-lay-up: 2x 1315.70€, and the highest, to the use of Prepregs: 2x 1451.68€.

Despite the higher manufacturing cost, the use of Prepregs on the Skin would be ideal since it significantly reduced the total mass of the wing, in comparison to any other methods, therefore significantly reducing operational costs and increasing the aircraft's operational capabilities.

All the materials needed for the manufacturing of the wing were:

- Bidirectional Carbon Fiber, 3K, HS, 160 $[gr/m^2]$, (plain weave) ("normal" hand-lay-up impregnation) ($C_n^{n^o}$). Quantity: ≈ 32.32 $[m^2]$ (if no Pre-impregnation or Prepreg is used); ≈ 23.77 $[m^2]$ (if Pre-impregnation or Prepreg is used);
- Bidirectional Carbon Fiber Pre-impregnated or Equivalent Prepreg material ($Cp_n^{n^o}$). Quantity: 8.55 $[m^2]$;
- Epoxy Resin: SR 1500 + Hardener: Sicomin SD 2505 (100 [g] Epoxy - 33 [g] Hardener). Quantity: ≈ 2.750 [kg] (if Prepreg is used); ≈ 5.740 [kg] (if no Pre-impregnation is used); ≈ 7.776 [kg] (if normal hand-lay-up method is used);
- Airex C70.75, thickness 3 [mm], (isotropic material) (A_n). Quantity: ≈ 3.40 $[m^2]$;
- Kevlar 49, 195 denier, bidirectional, plain weave ($K_n^{n^o}$). Quantity: ≈ 0.177 $[m^2]$.

From these materials the configurations created for each component were the following:

Skin:

- Areas over the spars' caps: $[C_2^{0^o}]$ or $[Cp_2^{0^o}]$ – 0.38 [mm];
- "Attachment areas" of the servo motors: $[C_{18}^{0^o}]$ or $[Cp_1^{0^o}/C_{16}^{0^o}/Cp_1^{0^o}]$ – 3.42 [mm];
- Kevlar hinged connection: $[C_1^{0^o}/K_2^{0^o}/C_1^{0^o}]$ or $[Cp_1^{0^o}/K_2^{0^o}/Cp_1^{0^o}]$ – 0.64 [mm] and $[C_1^{0^o}/K_1^{0^o}/A_1/K_1^{0^o}/C_1^{0^o}]$ *or* $[Cp_1^{0^o}/K_1^{0^o}/A_1/K_1^{0^o}/Cp_1^{0^o}]$ – 3.64 [mm];
- All other skin areas: $[C_1^{0^o}/A_1/C_1^{0^o}]$ *or* $[Cp_1^{0^o}/A_1/Cp_1^{0^o}]$ – 3.38 [mm].

1st Spar:

- Caps: $[C_{27}^{0^o}]$ – 5.13 [mm]; Webs: $[C_8^{0^o}]$ – 1.52 [mm].

2nd Spar:

- Caps: $[C_8^{0^o}]$ – 1.52 [mm]; Webs: $[C_7^{0^o}]$ – 1.33 [mm].

Ribs:

- $[C_8^{0^o}]$ – 1.52 [mm].

For all components, except the Ribs and the Kevlar hinges, the 0º orientation of the material's fibers is coincident with the direction of the 1st Spar axis ($\neq z$). For the Ribs, the 0º orientation is coincident with

the x axis, see section 5.2.2. For the Kevlar hinge, the 0º orientation is coincident with the direction perpendicular to the 2nd Spar axis.

The curing process needed to ensure the mechanical characteristics of the structure was the following: vacuum bag at -0.5 [bar] during 24H, at a room temperature of 20ºC, with the air-condition system set to dry heat (low humidity environment). See section 4.6.1.1.

6.2.1 3D Solid Designs and Detailed Mapping of the Materials

In order to better visualize the final design of the wing and to better understand how and where each material should applied (in order to guarantee the mechanical characteristics of the structure), the wing was modeled as a 3D solid. Additionally, each continuous group of plies of a same material was given a unique color. The 3D solid wing model is shown in Figures 65–75.

Because the 3D solid model was designed in a dimensionally accurate manner it could be used as a guide for manufacturing purposes and / or as the basis for future detailed designs.

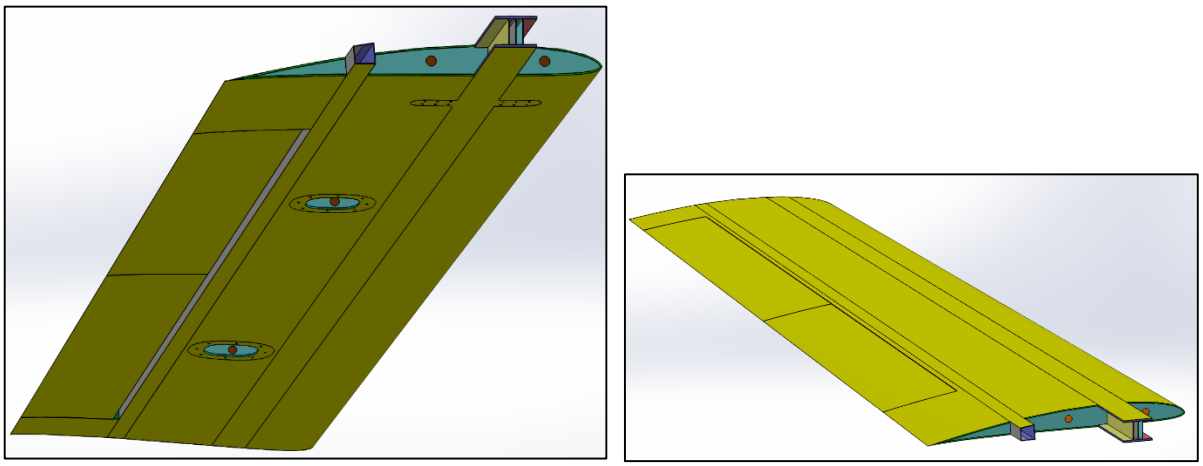

a) b)

Figure 65 - Complete Wing Geometry: a) Bottom view; b) Top view.

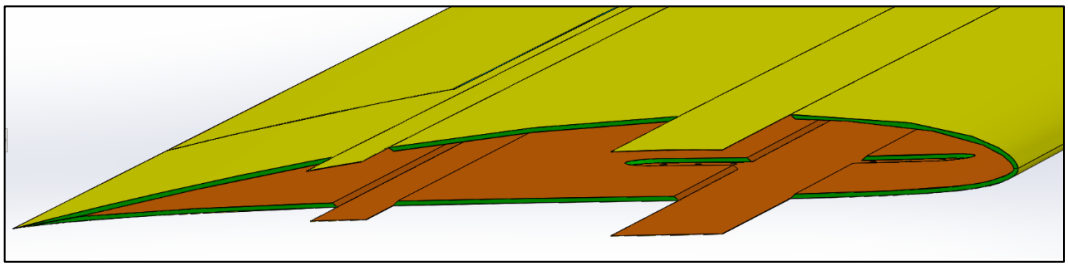

a)

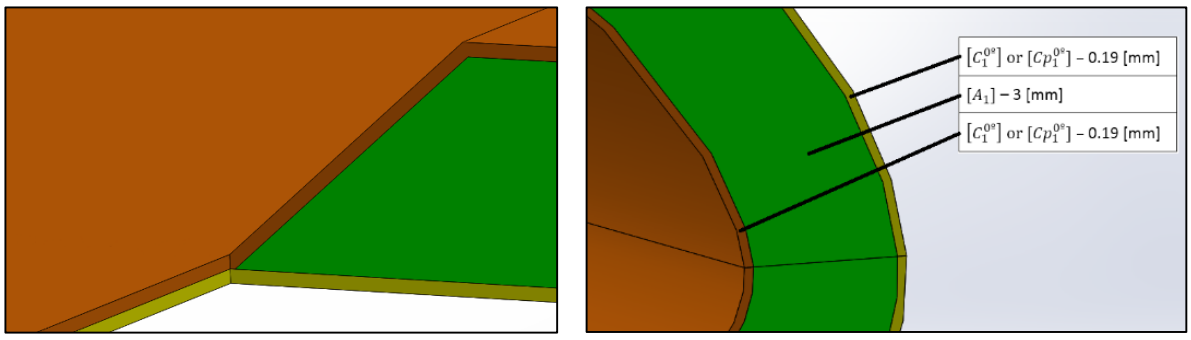

c) b)

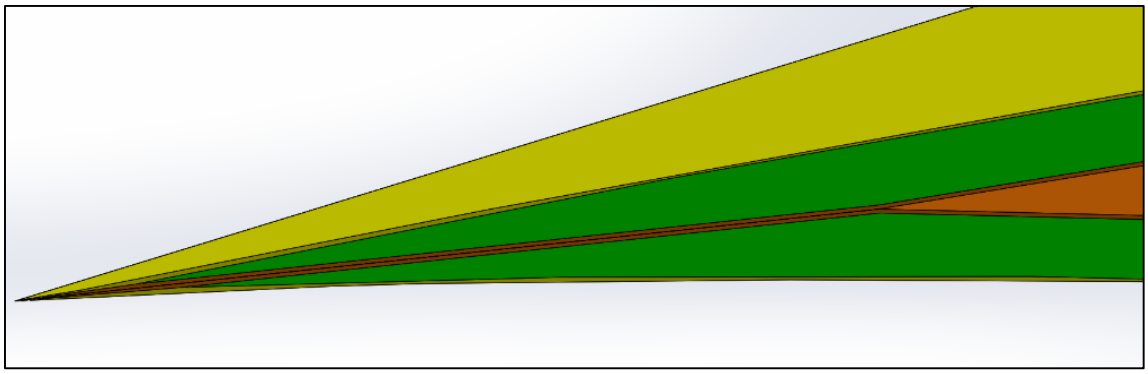

d)

Figure 66 – Wing Skin: a) Detail: root; b) Detail: leading edge; c) Detail: transition from skin without foam to skin with foam; d) Detail: trailing edge.

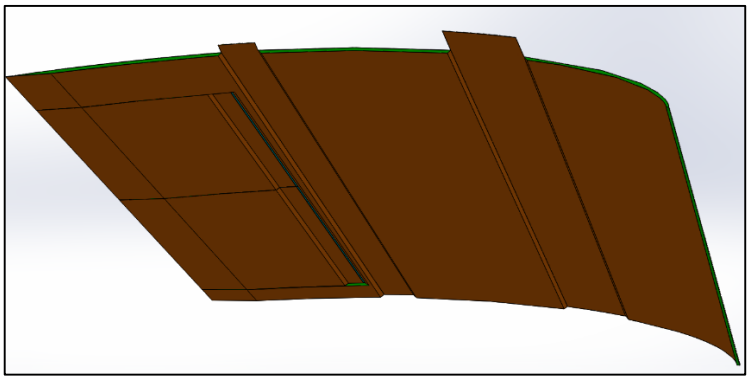

Figure 67 – Top Skin, Bottom view.

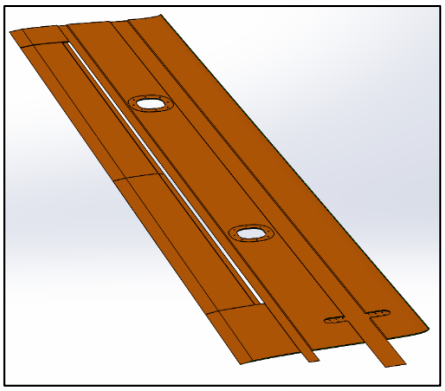

Figure 68 – Bottom Skin, Top view.

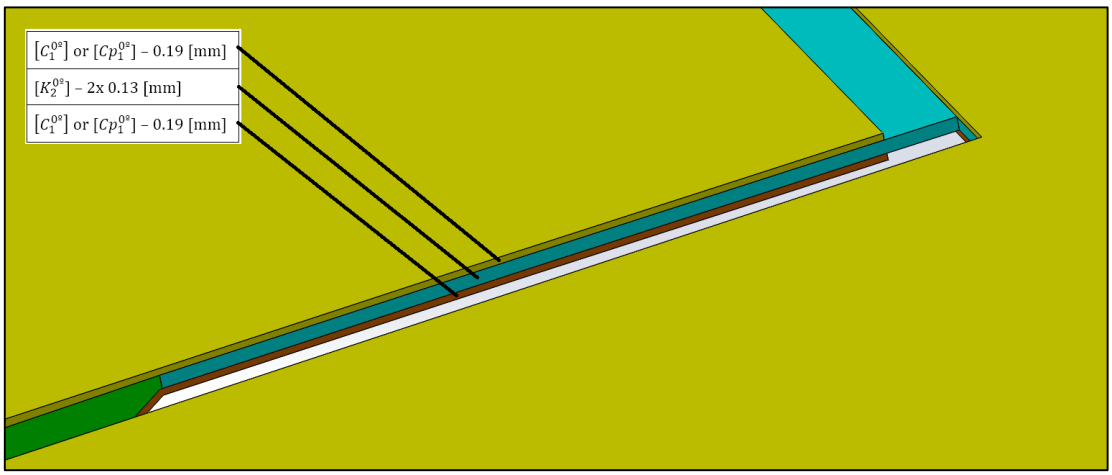

a)

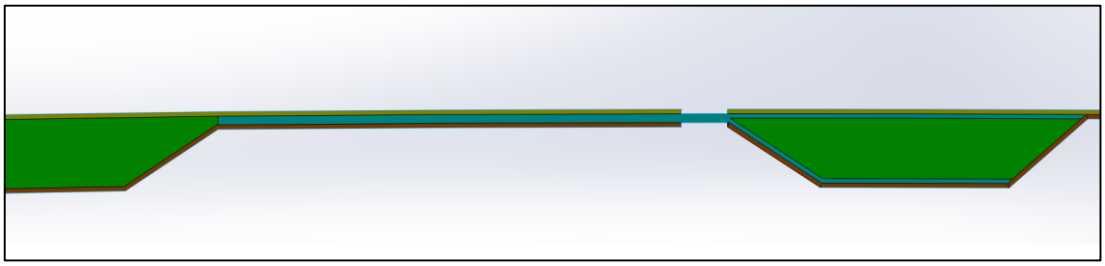

b)

Figure 69 – Kevlar Hinged Connection: a) Detail: close-up of the top skin, top view. 3 [mm] gap between the main structure and the Flap; b) Detail: close-up of the top skin, section view.

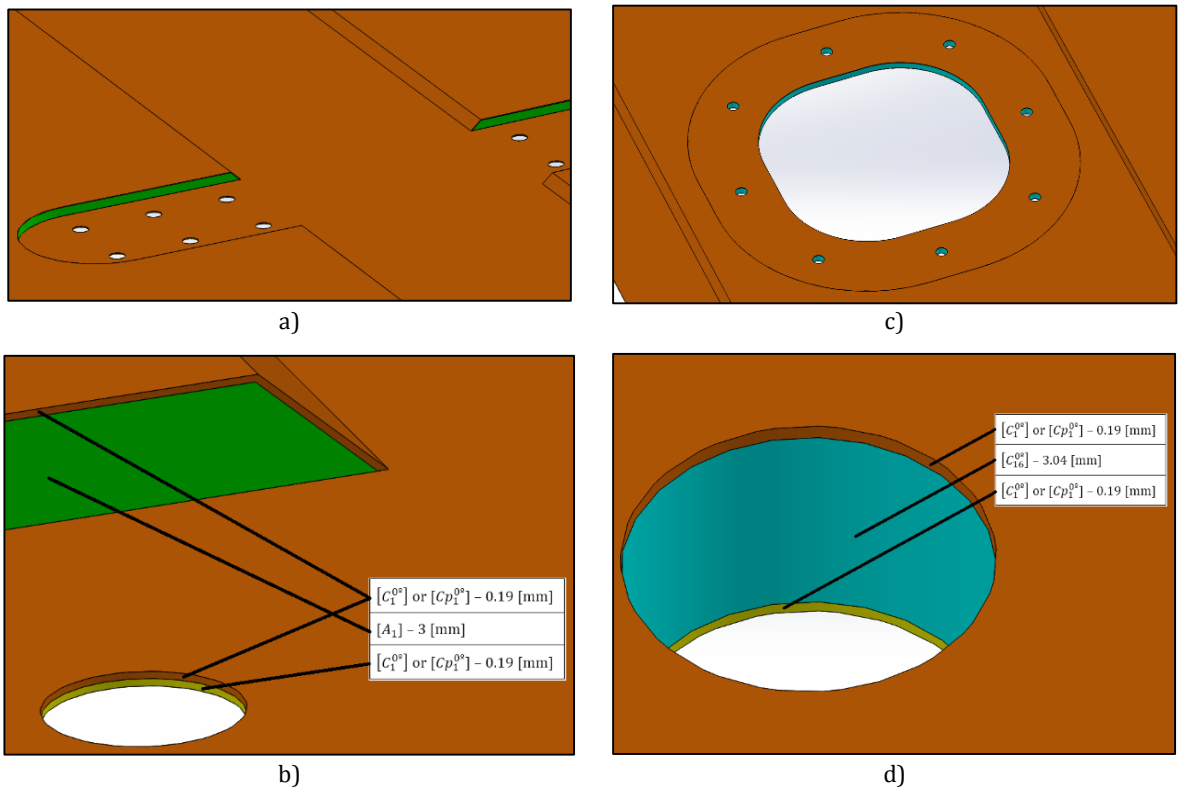

Figure 70 – Bottom skin: a) and b) Detail: close-up on the attachment area of the payload's "skin reinforcement"; c) and d) Detail: close-up on the attachment area of the servo motors' skin reinforcement;

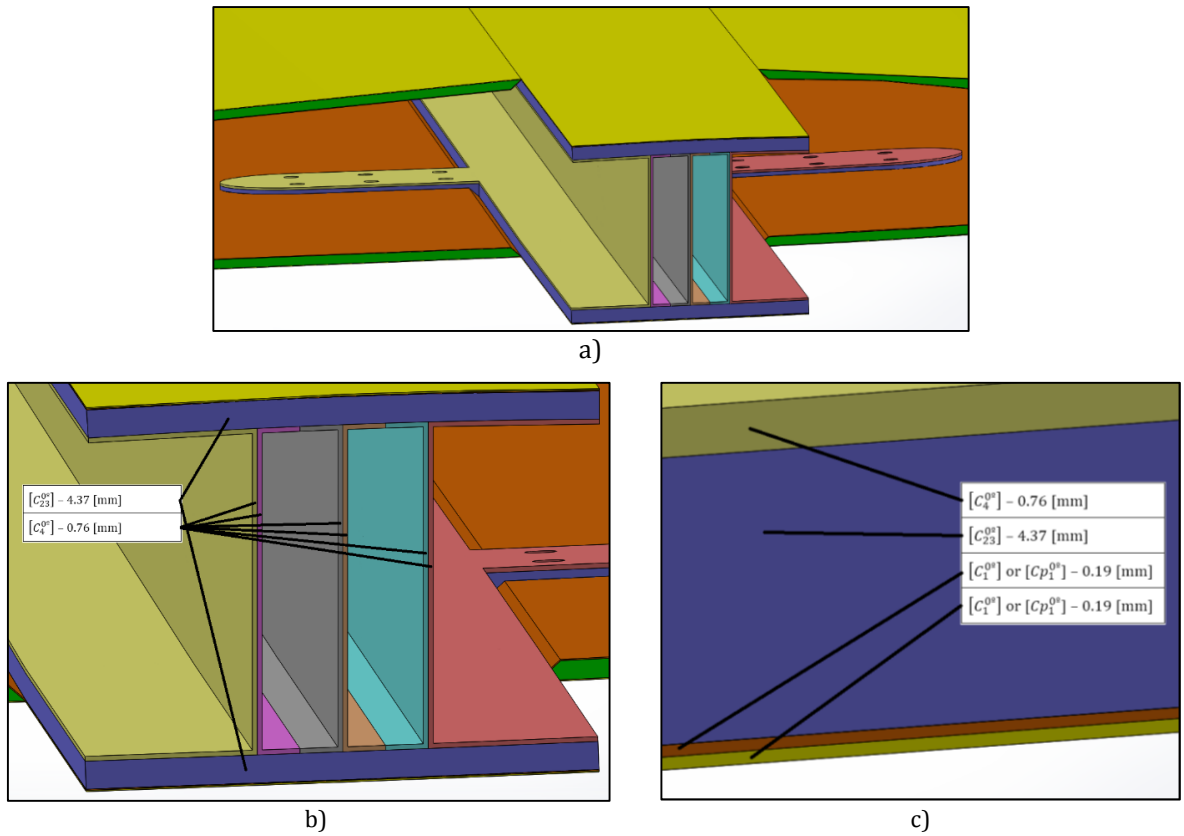

Figure 71 – 1st Spar: a) Detail: root; b) Detail: close-up on the plies that constitute the 1st Spar; c) Detail: close-up on some of the plies that constitute the 1st Spar and on the attachment to the bottom skin inner surface.

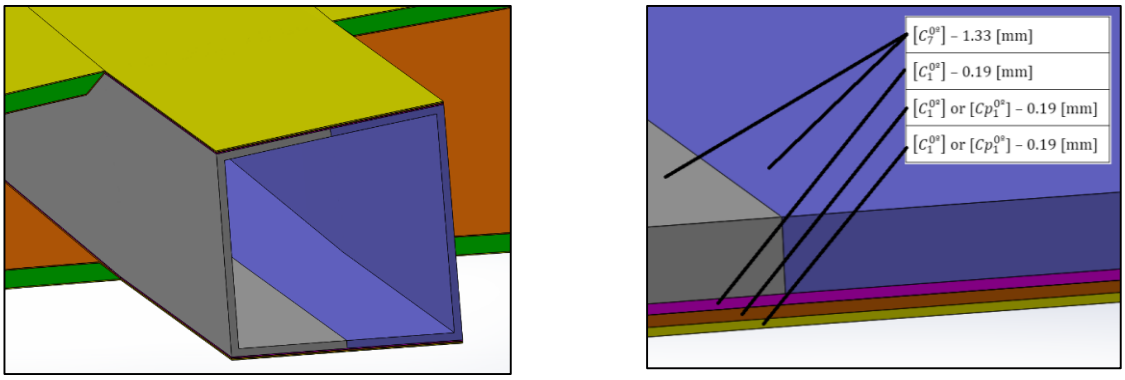

a) b)

Figure 72 – 2nd Spar: a) Detail: root; b) and c) Detail: close-up on the plies that constitute the 1st Spar and on the attachment to the bottom skin inner surface.

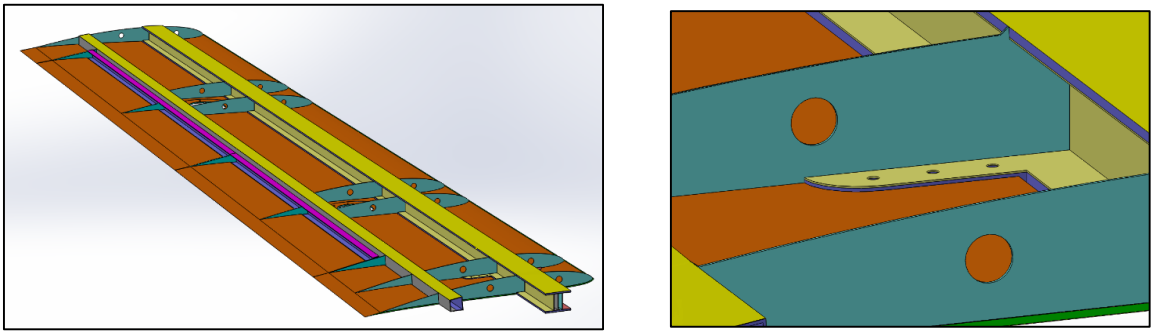

a) b)

Figure 73 – Bottom Skin of the main structure + 1st Spar + 2nd Spar + Flap Spar + Aileron Spar + Ribs: a) Top view; b) Detail: Ribs mid-section geometry.

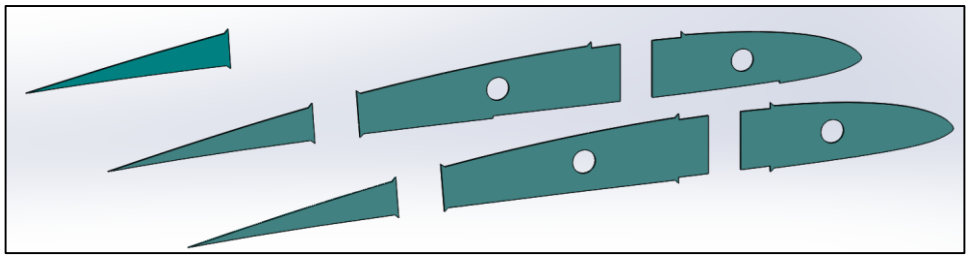

Figure 74 – Ribs geometry: Root Rib + 2nd Rib + 3rd Rib.

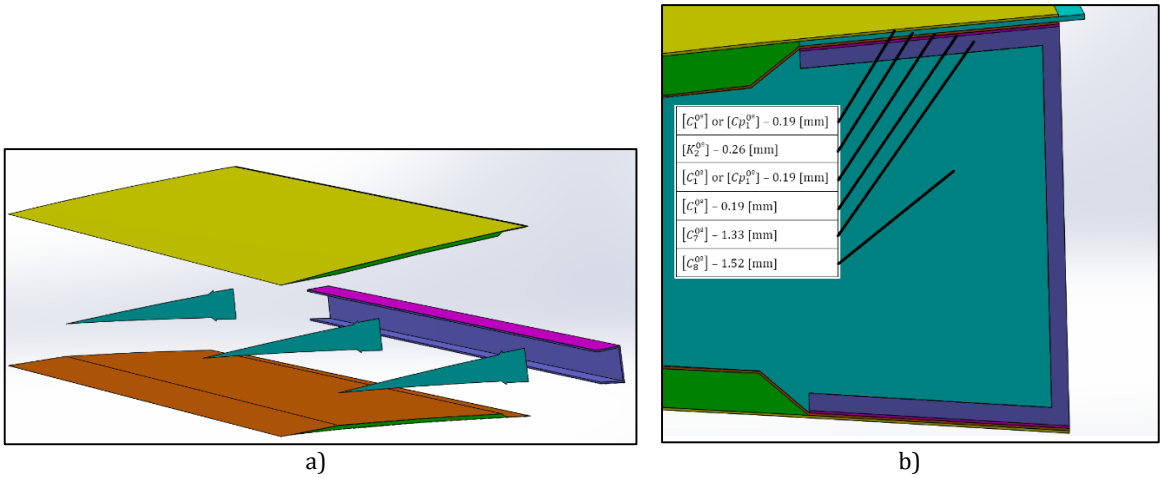

a) b)

Figure 75 – Flap or Aileron: a) Components exploded view; b) Detail: close-up on the plies that constitute each component.

6.2.2 Other Loading Conditions that the Structure Can Endure

Last but not least, it was considered relevant to further complete the present work by studying other loading conditions that may occur during transport, storage or display or even that might be needed or better suited for a particular mission.

The wing structure was capable of enduring the following loading condition without suffering any damage:

- No Payload – relevant because the weight of the payload acts in the contrary direction to the Lift therefore, reducing the maximum wing tip displacement and, consequently, the maximum stress;
- 30 [kg] Payload;
- 145 [kg] Payload - will never happen but serves to show the strength capabilities of the wing;
- Reuse of the servo motors locations for additional payload: 10 [kg] (motor 1 location only) – max stress of the foam was exceeded. However, this could be possible if an additional reinforcement of the Skin was introduced (internally and over the skin) between the existing reinforcement and the 1st and 2nd Spar bottom caps → simple modification with small cost associated (little material used). Also, accessibility exists due to the 100x100 [mm] cut-outs;
- Reuse of the servo motors locations for additional payload: 2 [kg] (motor 1 location only);
- Reuse of the servo motors locations for additional payload: 2 [kg] (2 kg for each motor 1 and 2 locations);
- Aircraft fully loaded with fuel and payload (145 [kg] – MTOW), on the ground, suspended by its wings at the payload position;
- Aircraft fully loaded with fuel and payload (145 [kg] – MTOW), on the ground, suspended by its wing tips;

7 Conclusions and Future Work

7.1 Conclusions

The design and optimization of the wing structure was a challenging project which required a proactive and iterative approach to the design by balancing three fundamental criterial: design, materials selection and manufacturing processes.

It involved determining the loads on the structure, planning the general shape and layout, choosing materials, and then shaping, sizing and optimizing its many components to give every part just enough strength without excess weight and also to reduce cost.

A successful "chain top-down" approach was used to optimize the wing structure by individually optimizing each component in a specific sequence based on how and where forces are applied to the structure and how does each component contribute to the structure's ability to resist to those forces. This approach could be described as a "hierarchic decomposition method" and it was inspired by the logic behind the "topological optimization method".

A manual pre-impregnation method was found to be successful in reducing the mass of the skin thus, the cost and weight of the wing.

The resulting wing structure which included flaps and ailerons, complied with all the structural, mass and operational criteria imposed and was estimated to have a manufacturing cost, in terms of materials, close to 3000 €.

Furthermore, the wing design and materials were carefully thought-out and selected in order to create a structure capable of being used with multiple payload configurations and able to operate in various mission scenarios and environments including high salinity ones.

Moreover, regulations, design manuals, books and scientific papers were used, as much as possible, for guiding and fundamenting every design decision so to allow for the structure's certification in terms of airworthiness.

7.2 Future work

Regarding future works that may give continuity to the present thesis, the following steps are suggested:

Step 1: Further optimization of the design by utilizing "topology optimization" which will probably result in further change to the geometries of both the Ribs and Spars.

Step 2: Optimization of the orientation of the composite materials fibers.

Step 3: With or without performing the previous steps, conduct a structural simulation of the final structure in a software such as ANSYS in order to, more precisely, determine the behavior of the structure before any manufacturing is started. Correct any design flaws that may be detected during the simulation.

Step 4: Construction of individual components of the structure or a full scale complete prototype to be used for structural integrity testing in order to evaluate if the components / full structure can endure the forces they were designed to withstand. The construction could resort to "traditional methods" or make use of advances "State of the Art" 3D printing technologies. Also, as much as possible, small drilled holes could and should be replaced by embedded holes (see section 4.5.1).

Step 5: Establish a "LEAN" manufacturing process and produce the first fully operational wing.

References

[1] "Portuguese Airspace Under Portugal Responsibility," [Online]. Available: https://www.nav.pt/en/nav/air-navigation-services-1/airspace. [Accessed 2016].

[2] "SRR (Search and Rescue Region)," Esquadra 751, 2016. [Online]. Available: http://www.emfa.pt/www/po/esquadra/link-751-013.006.001-descricao.

[3] "A Marinha ao Serviço de Portugal," Marinha Portuguesa, 2016. [Online]. Available: http://www.marinhasplp.org/PT/asmarinhas/doutrinas/Documents/A%20Marinha%20ao%20Servi%C3%A7o%20de%20Portugal_23MAR.pdf.

[4] "A Vigilância Marítima na Força Aérea," Força Aérea Portuguesa, 2016. [Online]. Available: http://www.emfa.pt/www/noticia-480-a-vigilancia-maritima-na-forca-aerea.

[5] "Busca e Salvamento Marítimo," Marinha Portuguesa, 2016. [Online]. Available: http://www.marinha.pt/pt-pt/marinha/busca-e-salvamento/Paginas/default.aspx.

[6] "Portugal, uma nação marítima," Marinha Portuguesa, 2016. [Online]. Available: http://www.marinhasplp.org/PT/asmarinhas/doutrinas/Documents/Portugal_uma_nacao_maritima.pdf.

[7] G. Oduntan, "Sovereignty and Jurisdiction in Airspace and Outer Space: Legal Criteria for Spatial Delimitation," 2011. [Online]. Available: http://landingbook.co/sovereignty_and_jurisdiction_in_airspace_and_outer_space_legal_criteria_for_spatial_delimitation_routledge_research.pdf.

[8] "SAR," Esquadra 502, 2016. [Online]. Available: http://www.emfa.pt/www/po/esquadra/link-502-005.002.003.003-sar.

[9] "PITVANT," Força Aérea Portuguesa, 2016. [Online]. Available: http://www.emfa.pt/www/po/unidades/subPagina-10D00-019.005.003.004-pitvant.

[10] "Sobre terra e sobre o mar, os UAV da Força Aérea," Revista Operacional, 2016. [Online]. Available: http://www.operacional.pt/sobre-terra-e-sobre-o-mar-os-uav-da-forca-aerea/.

[11] "ANTEX-M X00," EMFA, 2012. [Online]. Available: http://www.emfa.pt/www/conteudos/galeria/noticias/abril2012/extended_625.jpg.

[12] "UAS30," UAVision, 2014. [Online]. Available: http://www.uasvision.com/wp-content/uploads/2014/11/UAS-30.jpeg.

[13] "ANTEX-M X03," blogspot, 2012. [Online]. Available: http://4.bp.blogspot.com/-EheWDXhYipM/Vm7lTVLZmhI/AAAAAAAAXeA/XrT6fQHD-vQ/s1600/2012%2B-%2BAntex-M.jpg.

[14] J. Morgado, *Atividades de Investigação, Desenvolvimento & Inovação na área dos Sistemas Aéreos Autónomos Não-Tripulados. Boletim informativo, Cidadania e Defesa da Associação de Auditores dos cursos de Defesa Nacional, 1º semestre,* vol. 53, Centro de Investigação da Academia da Força Aérea, 2015, pp. 16-21.

[15] J. Morgado, *Sistemas Aéreos Autónomos Não-Tripulados nas Vertentes Militar, de Segurança e Civil: definição de uma Estratégia Nacional. Instituto Universitário Militar. Trabalho Individual de Pesquisa realizado no âmbito do Curso de Promoção Oficial General 2015-2016,* 2016.

[16] *Visão estratégica para sistemas aéreos autónomos não-tripulados,* Lisboa: EMFA, Força Aérea, 2013.

[17] DEP-DE, *UAV150 - Deliverable 1 - Issue 1 - Project Definition,* Ministério da Defesa Nacional, Força Aérea, Comando de Logística, 2016.

[18] S. A. Brandt, R. J. Stiles, J. J. Bertin and R. Withford, "Introduction to Aeronautics: A Design Perspective," Second Edition ed., AIAA Educational Series, 2004, pp. 74-75; 85; 90; 145; 225; 228; 230; 302; 315; 319-320; 323; 325-326; 329-332; 335; 340.

[19] J. Sobieszcznski-Sobieski and R. T. Haftka, *AIAA 96-0711 Multidisciplinary Aerospace Design Optimization: Survey of Recent Developments,* NASA Langley Research Center and University of Florida, 1995.

[20] "Topological Optimization Process," 06 2017. [Online]. Available: https://www.pinterest.pt/pin/322288917067916066/.

[21] UAVision, *MALE Prototype, Preliminary Specs,* UAVsision.

[22] "Airfoil S4110," Airfoil Tools, 2016. [Online]. Available: http://airfoiltools.com/airfoil/details?airfoil=s4110-il.

[23] T. C. Corke, "Design of Aircraft," Prentice Hall, 2003, pp. 207; 209; 213-216; 263-264.

[24] T. Megson, "Aircraft Structures for Engineering Students," Third Edition ed., Elsevier, 1999, pp. 211; 218; 220-225; 246.

[25] P. F. F. d. Albuquerque, *Structural Loads Handbook, Dissertação de Mestrado em Engenharia Aeroespacial,* Instituto Superior Técnico, 2011, pp. 3-8.

[26] NATO, *Light Unmanned Aircraft Systems Airworthiness Requirements, NATO STANDARD AEP-83,* NATO Standardization Agency (NSA) NATO/OTAN, 2014.

[27] "International Standard Atmosphere," The Engineering ToolBox, [Online]. Available: http://www.engineeringtoolbox.com/international-standard-atmosphere-d_985.html. [Accessed 2016].

[28] D. J. P. Paiva, *Optimização aerodinâmica e estrutural da asa de um UAV de nível 2 de acordo com os requisitos de missão do PITVANT,* Sintra: Academia da Força Aérea (AFA), 2011.

[29] *Conceptual Paper for establishing a harmonized European Airworthiness Regulatory Framework for military RPAS, 02000024,* European Defense Agency (EDA), 2014 , p. Annex 2.

[30] F. Cunha, *Acetatos de Estruturas Aeroespaciais,* Lisboa: Intituto Superior Técnico (IST), 2008.

[31] A. Suleman, *Acetatos de Projeto Aeroespacial,* Instituto Superior Técnico (IST), 2010.

[32] J. J. Silva, *Análise Modal de uma pá de turbina eólica com e sem carregamento axial, Trabalho 3 Mecânica Estrutural,* Lisboa: Instituto Superior Técnico (IST), 2015.

[33] *Certification Specification for Large Aeroplanes (CS-25) - Subpart C - Structure,* European Aviation Safety Agency, 2010.

[34] D. M. Neubauer and G. Günther, *Aircraft Loads,* Munich: DaimlerChrysler Aerospace GmbH, p. 14.

[35] J. N. REDDY, *Mechanics of Laminate Composite Plates and Shells - Theory and Analysis,* 2nd Edition ed., Boca Raton: CRC PRESS, 2004. ISBN 0-8493-1592-1.

[36] A. M. Moreira, *Materiais Compósitos,* Tomar: Instituto Politécnico de Tomar, 2008.

[37] S. d. M. d. C. Monte, *Previsão do Comportamento Mecânico e Otimização de um Componente Estrutural de Aeronaves em Material Compósito,* Sintra: Academia da Força Aérea, 2015.

[38] J. Cardoso, *Compósitos,* Direção de Engenharia e Programas, Força Aérea Portuguesa, 2013.

[39] C. A. M. Soares, C. M. M. Freitas and M. J. M. Soares, *Mechanics of Composite Materials and structures,* Kluwer Academic Publishers, 1999. ISBN 0-7923-5870-8.

[40] *Stress - strain curve of a ductile material,* ResearchGate, 2017.

[41] *Stress Strain Curves,* General Composites PVT. LTD., 2017.

[42] G. Czél and M. R. Wisnom, *Demonstration of pseudo-ductility in high performance glass/epoxy composites by hybridization with thin-ply carbon prepreg,,* Compos. Part A Appl. Sci. Manuf., vol.52, 2013, pp. 23-30.

[43] V. d. Berderote, Fundamentos de Aerodinâmica Incompressível, Intituto Superior Técnico (IST), 1997, p. 489.

[44] L. C. Dorworth, G. L. Gardiner and G. M. Mellema, *Essentials of Advanced Composite Fabrication & Repair,* Newcastle, Washington: Aviation Supplies & Academics (ASA), Inc., 2009, pp. 73-81; 118-119.

[45] "Panels," PANELITE, 2017. [Online]. Available: http://www.panelite.us/products/interior-bonded-series/bonded-series-overview/resource-efficiency/.

[46] "Junkers JU-52 3M Walk Around," Prime Portal, 2017. [Online]. Available: http://data3.primeportal.net/hangar/domeric_barbot/ju-52_3m/images/ju-52_3m_20_of_32.jpg.

[47] J. Sikora, *A Summary of Stress Concentrations in the Vicinity of Openings in Ship Structures,* Naval Ship Research and Development Center, Bethesda, Md. 20034, 1973, pp. 7-8.

[48] C. Y. Huang, R. S. Trask and I. P. Bond, *Characterization and analysis of carbon-reinforced polymer composite laminates with embedded circular vasculature,* Journal of The Royal Society, 2010.

[49] S. R. Heller, "Stress Concentration Factors for a Rectangular Opening with Rounded Corners in a Biaxially Loaded Plate," *Journal of Ship Research,* September 1969.

[50] N. E. Reish and G. H. Girty, *Definition and Mathematics of Pure Shear,* San Diego State University, 2011.

[51] J. Shi, *Stress Fields Near Holes or Cut-outs in a Unidirectional Fiber Reinforced Composite lamina,* Cornell University, January 2008.

[52] A. M. D'Arcangelo, *A Guide to Sound Ship Structures,* Cornell maritime Press, Cambridge, 1964.

[53] W. L. Ko, *Stress Concentration Around a Small Circular Hole in the HIMAT Composite Plate,* National Aeronautics and Space Administration (NASA), December 1985.

[54] L. M. P. Durão, J. M. R. Tavares, V. H. C. d. Albuquerque, J. F. S. Marques and O. N. Andrade, *Drilling Damage in Composite Material,* Materials Journal, 2014, pp. 3809-3014.

[55] H. Hocheng and C. Dharan, *Delamination during drilling in composite laminates,* 1990, pp. 236-239.

[56] H. Hocheng and C. Tsao, *Effects of special drill bits on drilling-induced delamination of composite materials,* Int. J. Mach. Tools Manuf., 2006, pp. 1403-1416.

[57] H. Hocheng and C. Tsao, *Comprehensive analysis of delamination in drilling of composite materials with various drill bits.,* J. Mater. Process. Technol, 2003, pp. 335-339.

[58] C. Tsao and H. Hocheng, *Parametric study on thrust force of core drill,* J. Mater. Process. Technol, 2007, pp. 37-40; 192-193.

[59] C. Tsao and H. Hocheng, *Effects of exit back-up on delamination in drilling composite materials using a saw drill and a core drill,* Int. Mach. Tools Manuf., 2005, pp. 1261-1270.

[60] L. M. P. Durão, D. J. S. Gonçalves, J. M. R. S. Tavares, V. H. C. d. Albuquerque, A. A. Vieira and A. Marques, *Drilling tool geometry evaluation for reinforced composite laminates,* Compos. Struct., 2010, pp. 1545-1550.

[61] V. Schulze, C. Becke, K. Weidenmann and S. Dietrich, *Machining strategies for hole making in composites with minimal workpiece damage by directing the process forces inwards,* Compos. Struct., 2011, pp. 1545-1550.

[62] R. Zitoune, V. Krishnaraj and F. Collombet, *Study of drilling of composite material and aluminium stack,* Compos. Struct., 2010, pp. 1246-1255.

[63] V. Krishnaraj, R. Zitoune and J. P. Davim, *Drilling of polymer-matrix composites,* Springer: Heidelberg: Springer Briefs in Applied Sciences and Technology, 2014.

[64] W. Chen, *Some experimental investigations in the drilling of carbon fibre-reinforced plastic (CFRP) composite laminates,* Int. J. Mach. Tools Manuf., 1997, pp. 1097-1108.

[65] *Mechanical Properties of Carbon Fibre Composite Materials, Fibre / Epoxy resin (120ºC),* Performance Composites Ltd, 28/03/2017.

[66] P. Krishnan, *Vibrations and fatigue interactions of laminate composites,* p. Slide 59 and 60.

[67] P. K. Mallick, *Fiber - Reinforced Composites, Materials, Manufacturing, and Design,* Third Edition ed., Dearborn, Michigan: Department of Mechanical Engineering University of Michigan-Dearborn, CRC Press Taylor & Francis Group, LLC., 2007.

[68] J. R. Vinson and R. L. Sierakowski, *The behaviour of structure composed of composite materials,* New York, Boston, Dordrecht, Moscow, 2004.

[69] D. Gay, S. V. Hoa and S. W. Tsai, *Composite materials design and applications,* London, New York, Washington: Boca Raton, 2003.

[70] AIREX and BALTEK, *Airex C70, Universal Structural Foam, DATA SHEET, 07.2011,* 3A Composites.

[71] C. d. Merchant, *Carbon characteristics, Heat conductivity.*

[72] *Nastran in-CAD For SolidWorks,* NEi, 2017.

[73] "Strategic Concept of Employment for Unmanned Aircraft Systems in NATO," Joint Air Power Competence Center (JAPCC), January 2010. [Online]. Available: http://www.japcc.org/wp-content/uploads/UAS_CONEMP.pdf.

Annexes

Annex 1

Wing Root geometric data points (.txt)

x [mm]	y [mm]	z [mm]
722	0	0
719.66794	0.3971	0
712.88836	1.64616	0
702.08724	3.76162	0
687.61114	6.55576	0
669.62612	9.81198	0
648.31268	13.48696	0
623.98128	17.5446	0
596.9857	21.89826	0
567.7086	26.40354	0
536.5182	30.91604	0
503.74662	35.25526	0
469.74764	39.26958	0
434.8245	42.84348	0
399.30932	45.86144	0
363.51978	48.25126	0
327.79522	49.97684	0
292.46054	50.98764	0
257.85508	51.27644	0
224.29652	50.84324	0
192.13864	49.7097	0
161.68468	47.87582	0
133.23066	45.3777	0
107.0726	42.22978	0
83.4271	38.46816	0
62.51798	34.14338	0
44.52574	29.3132	0
29.55146	23.99206	0
17.59514	18.30992	0
8.69288	12.4906	0
2.888	6.7507	0
0.15162	1.37902	0
0	0	0
0.85918	-2.94576	0
5.4511	-6.44024	0
13.7541	-9.50874	0
25.65988	-11.7686	0
41.32006	-13.1404	0
60.74186	-13.79742	0
83.74478	-13.8624	0
110.08334	-13.4653	0
139.43986	-12.68554	0
171.48222	-11.5881	0
205.83498	-10.23074	0
242.13714	-8.67844	0
279.94828	-7.0034	0
318.84964	-5.25616	0
358.4008	-3.51614	0
398.1469	-1.86276	0
437.57532	-0.38266	0
476.20954	0.87362	0
513.53694	1.8772	0
549.08822	2.5992	0
582.4013	3.01796	0
613.02132	3.14792	0
640.53674	3.00352	0
664.57212	2.62086	0
684.76646	2.0577	0
700.83096	1.39346	0
712.51292	0.73644	0
719.6174	0.20938	0
722	0	0

Wing Tip geometric data points (.txt)

x [mm]	y [mm]	z [mm]
2.312	5.4043	3250
0.12138	1.10398	3250
0	0	3250
0.68782	-2.35824	3250
4.3639	-5.15576	3250
11.0109	-7.61226	3250
20.54212	-9.4214	3250
33.07894	-10.5196	3250
48.62714	-11.04558	3250
67.04222	-11.0976	3250
88.12766	-10.7797	3250
111.62914	-10.15546	3250
137.28078	-9.2769	3250
164.78202	-8.19026	3250
193.84386	-6.94756	3250
224.11372	-5.6066	3250
255.25636	-4.20784	3250
286.9192	-2.81486	3250
318.7381	-1.49124	3250
350.30268	-0.30634	3250
381.23146	0.69938	3250
411.11406	1.5028	3250
439.57478	2.0808	3250
466.2437	2.41604	3250
490.75668	2.52008	3250
512.78426	2.40448	3250
532.02588	2.09814	3250
548.19254	1.6473	3250
561.05304	1.11554	3250
570.40508	0.58956	3250
576.0926	0.16762	3250
578	0	3250

Annex 2

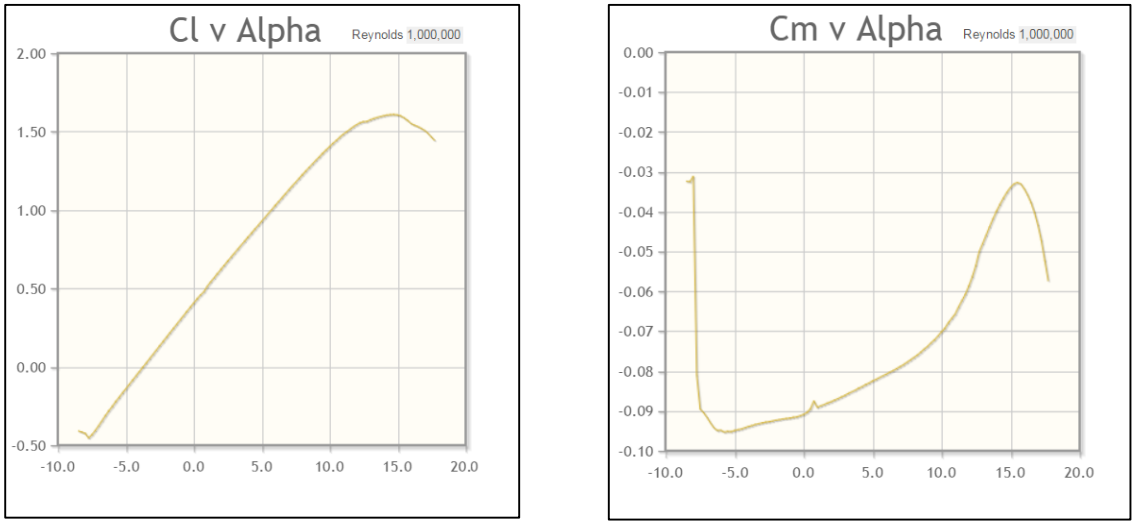

a) b)

Figure 76 – Airfoil S4110 characteristics: a) Cl vs Alpha; b) Cm vs Alpha.

Annex 3

Finite Plane: Size 1.5x1.5 [m]; Thickness: 2 [mm]; Material: Al 2024-T3; Square: 0.5x0.5 [m] (Figure 77); Circle: D=0.5 [m] (Figure 78); 3D meshing with triangular finite elements; Boundary Conditions: roller/slider constraint for the top, bottom and left outer-surfaces and for the frontal surface; forced horizontal displacement of 10 [mm] for the right outer-surface.

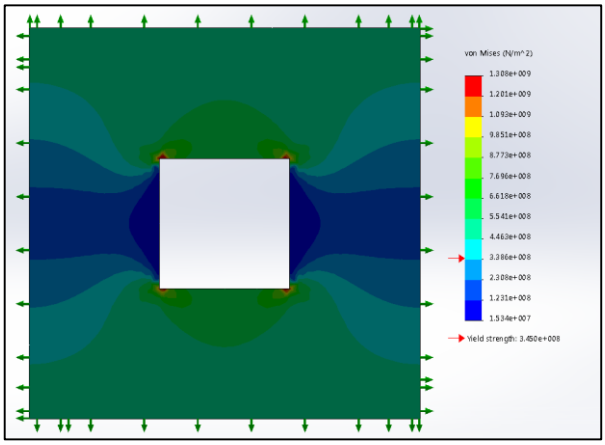

Figure 77 – Finite Element Analysis Stress Results for Square hole. Max stress: 1.308 [GPa].

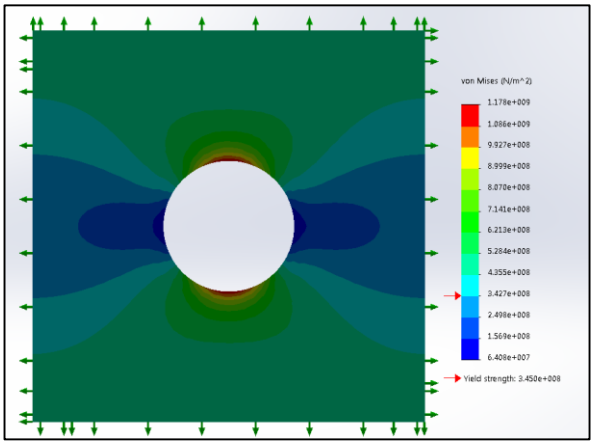

Figure 78 - Finite Element Analysis Stress Results for Circular hole. Max stress: 1.178 [GPa].

Annex 4

Properties needed to be obtain and applicable ASTM standards:

- **Fiber Percentage [%]** → D3171-09
- **Mass Density [kg/m^3]** → D3171-09
- **Tensile Modulus in X (E1) [MPa]** → *D3039/D3039M*

- **Tensile Modulus in Y (E2) [MPa]** → *D3039/D3039M*

- **Tensile Modulus in Z (E3) [MPa]** → *D7291/D7291M* (not available) → Use the Tensile Modulus of the Resin or the Tensile Modulus in Y direction of the Unidirectional composite material.

- **Compression Modulus in X (E1) [MPa]** → *D3410/D3410M*

- **Compression Modulus in Y (E2) [MPa]** → *D3410/D3410M*

- **Compression Modulus in Z (E3) [MPa]** → Same value as in Y for the Uni material. For Bi material the value in Y from the Uni material can also be used (approximation).

- **Poisson's Ratio in XY (ν12)**→ *D3039/D3039M e D3410/D3410M*

- **Poisson's Ratio in YZ (ν23)** → Non-existent. It is common to assume a value of 0.3 or use the Matrix's Poisson's Ratio.

- **Poisson's Ratio in XZ (ν13)** → Non-existent. It is common to assume a value of 0.3 or use the Matrix's Poisson's Ratio.

- **In-plane Shear Modulus in XY (G12) [MPa]** → *D3518/D3518M*

- **Tensile Strength in X (0º) (Stu or σu) [MPa]** → *D3039/D3039M*

- **Tensile Strength in Y (90º) (Stu or σu) [MPa]** → *D3039/D3039M*

- **Compressive Strength in X (0º) (Scu or σu) [MPa]** → *D3410/D3410M*

- **Compressive Strength in Y (90º) (Scu or σu) [MPa]** → *D3410/D3410M*

- **In-plane Shear Strength in XY (45º) (τ12u) [MPa]** → *D3518/D3518M*

- **Yield Strength (σc) [MPa]** → In fiber reinforced composites it is common for the Yield Strength to be coincident with the Tensile Strength (ultimate).

Annex 5

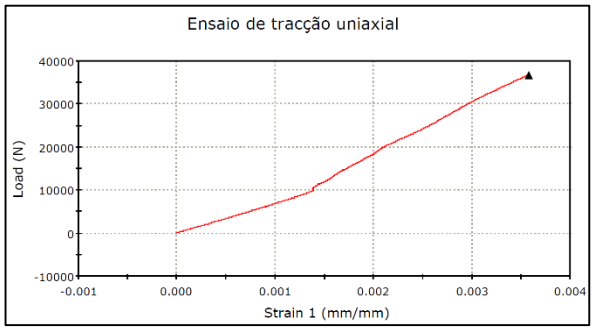

a)

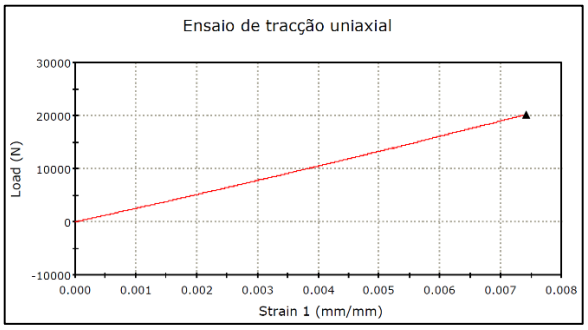

b)

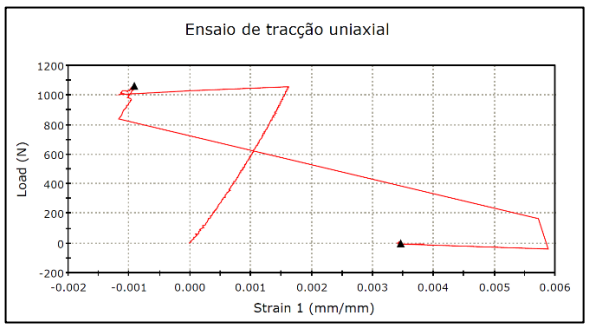

c)

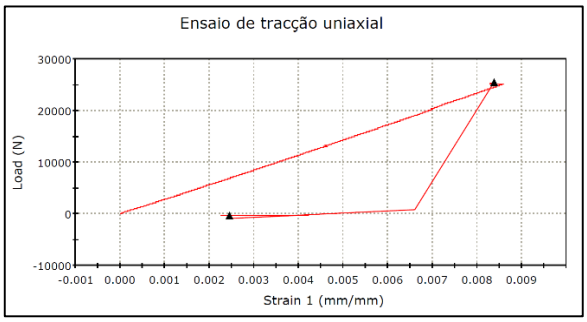

d)

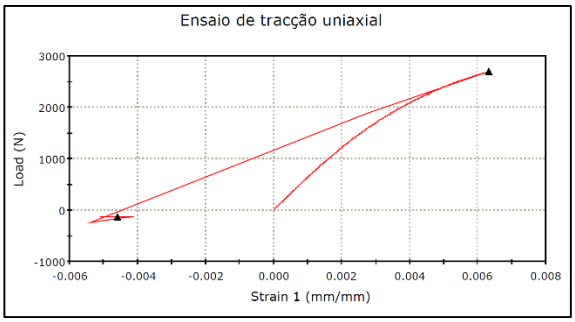

e)

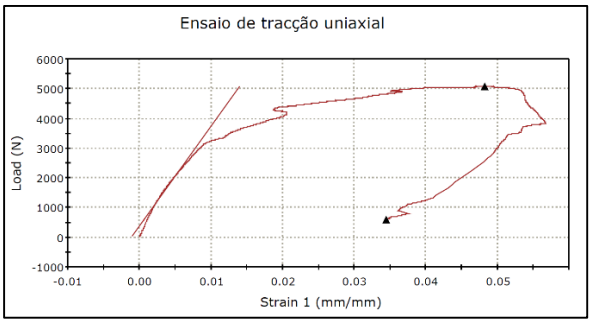

f)

Figure 79 – a) 0º Uni CF (no break); b) 0º Bi CF (no break); c) 90º Uni CF (break); d) 90º Bi CF (break); e) 45º Uni CF (break); f) 45º Bi CF (break).

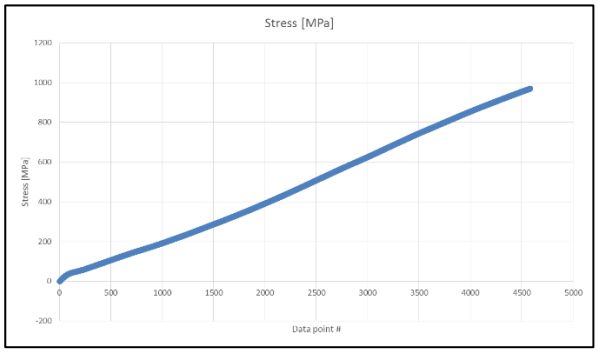

a)

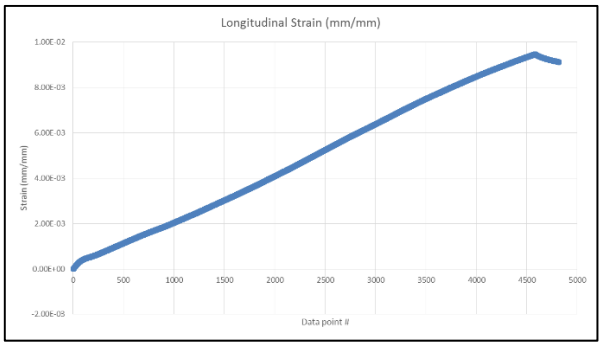

b)

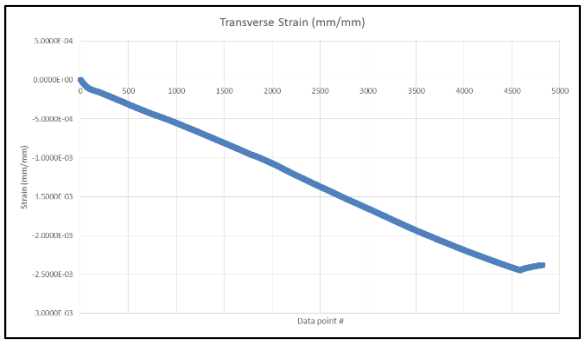

c)

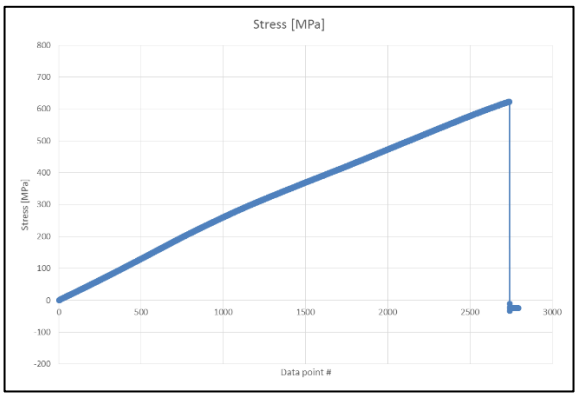

d)

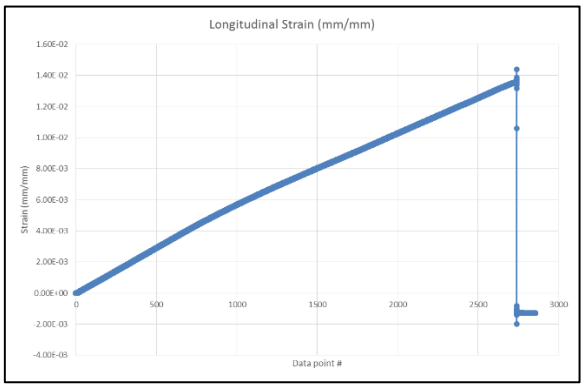
Longitudinal Strain (mm/mm)
Strain (mm/mm)
Data point #

e)

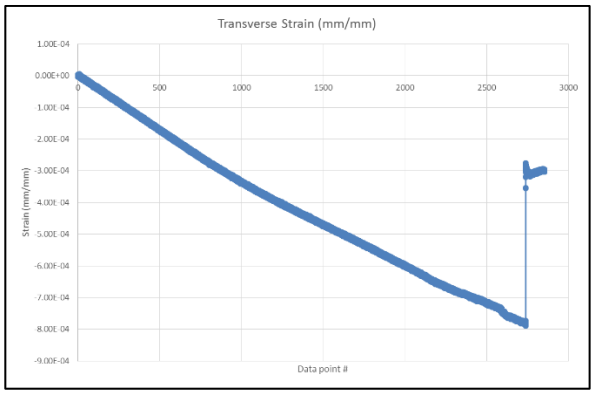
Transverse Strain (mm/mm)
Strain (mm/mm)
Data point #

f)

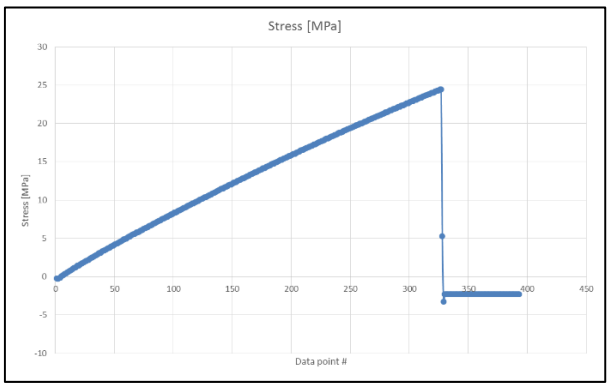
Stress [MPa]
Stress [MPa]
Data point #

g)

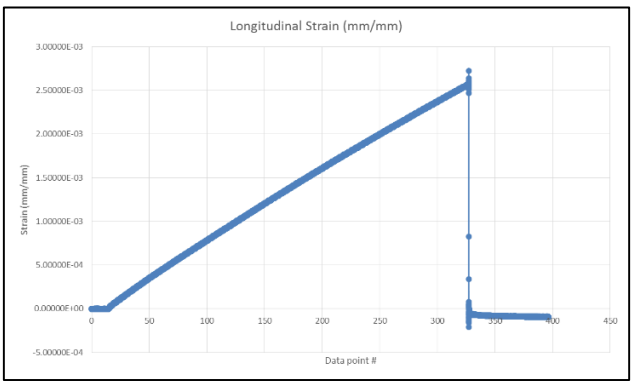
Longitudinal Strain (mm/mm)
Strain (mm/mm)
Data point #

h)

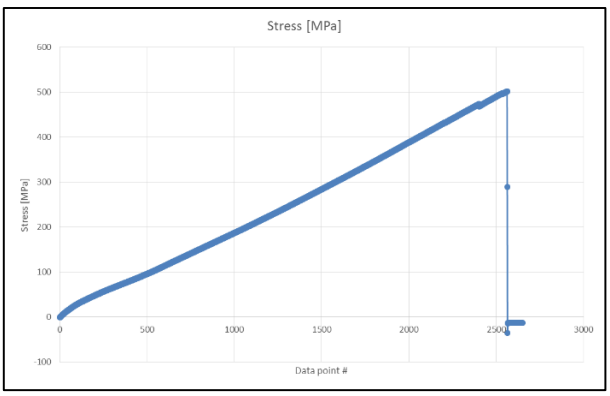
Stress [MPa]
Stress [MPa]
Data point #

i)

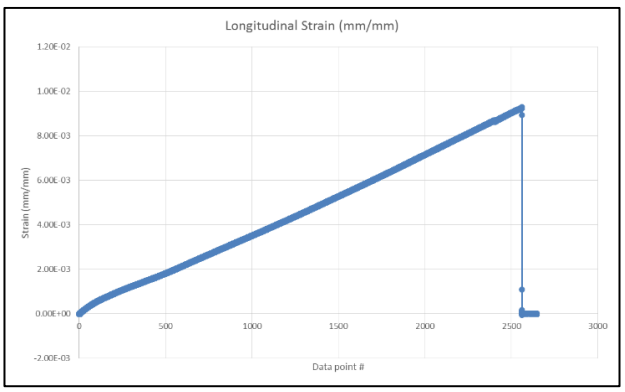
Longitudinal Strain (mm/mm)
Strain (mm/mm)
Data point #

j)

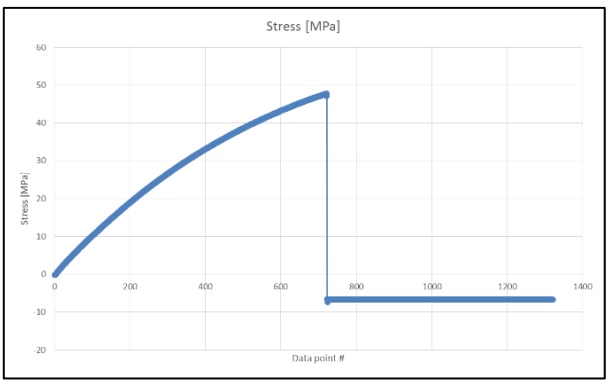
Stress [MPa]
Stress [MPa]
Data point #

k)

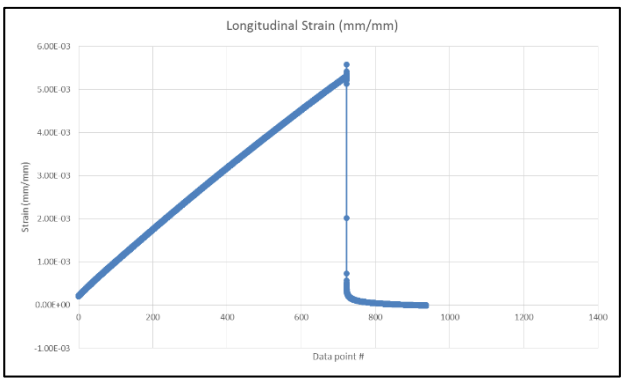
Longitudinal Strain (mm/mm)
Strain (mm/mm)
Data point #

l)

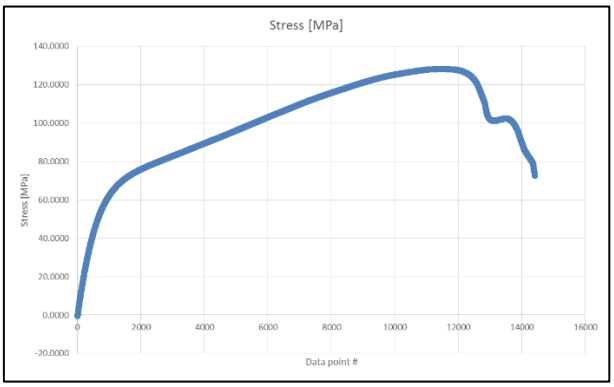

m)

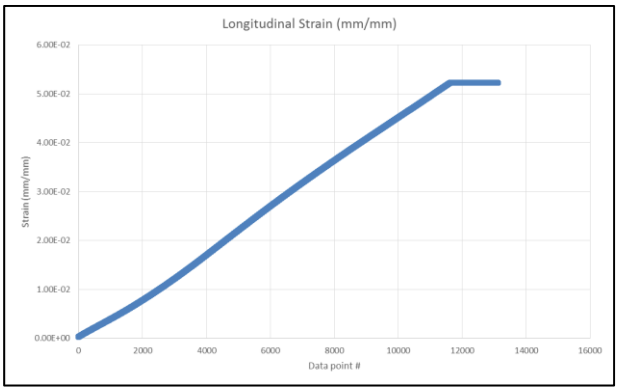

n)

Figure 80 – a) Stress: 0º Uni CF (no break); b) Longitudinal Strain: 0º Uni CF (no break); c) Transverse Strain: 0º Uni CF (no break); d) Stress: 0º Bi CF (break); e) Longitudinal Strain: 0º Bi CF (break); f) Transverse Strain: 0º Bi CF (break); g) Stress: 90º Uni CF (break); h) Longitudinal Strain: 90º Uni CF (break); i) Stress: 90º Bi CF (break); j) Longitudinal Strain: 90º Bi CF (break); k) Stress: 45º Uni CF (break); l) Longitudinal Strain: 45º Uni CF (break); m) Stress: 45º Bi CF (break) (also large yield); n) Longitudinal Strain: 45º Bi CF (break) (also large yield).

Annex 6

Table 12 – Properties of Epoxy + Uni Carbon Fiber (215 [gr/m^2])

		Experimental Uni (a / b)	Average Experimental Database [65]	Theoretical [66]
Resin Epoxy SR 1500 + Hardener Sicomin SD 2505 (100 [g] Epoxy - 33 [g] Hardener) (20ºC Cure, Dry heat air conditioning, -0.5 Bar vacuum)	-	-	-	-
Approximate Liquid Relations: 100 [g] Carbon fiber - 80 [g] Epoxy + Hardener	-	-	-	-
Fiber Mass Percentage [%] (for laminate with 9 Plies)	**0.655**	-	-	-
Average Ply thickness [mm] (for laminate with 9 Plies)	**0.222**	-	-	-
Mass Density [g/mm^3] (for laminate with 9 Plies)	**0.00145**	0.00145	0.0016	-
Tensile Modulus in X (E1) [MPa]	**95069.96**	245726 / 95069.96	135000	94580
Tensile Modulus in y (E2) [MPa]	**9172.87**	10256 / 9172.87	10000	9691
Tensile Modulus in Z (E3) [MPa]	**9172.87**	-	-	-
Longitudinal Tensile Modulus in 45º (E1') [MPa]	**10028.54**	8900 / 10028.54	-	-
Poisson's Ratio in XY (ν12)	**0.262**	0.262	0.3	0.29
Poisson's Ratio in YZ (ν23)	**0.396**	-	-	0.396
Poisson's Ratio in XZ (ν13)	**0.262**	-	-	-
In-plane Shear Modulus in XY (G12) [MPa]	**5000**	-	5000	2474
Out-of-plane Shear Modulus in YZ (G23) [MPa]	**3470**	-	-	3470
Out-of-plane Shear Modulus in XZ (G13) [MPa]	**5000**	-	-	-
Yield and Ultimate Tensile Strength in X (0º) (Stu or σu) [MPa]	**1500**	N.A / N.A. (σmax = 968 [MPa])	1500	-
Yield and Ultimate Tensile Strength in Y (90º) (Stu or σu) [MPa]	**22.46725**	20.472 / 24.4625	50	-

Yield and Ultimate Tensile Strength in Z (Stu or σu) [MPa]	**22.46725**	-	-	-
Yield and Ultimate Compressive Strength in X (0º) (Scu or σu) [MPa]	**1200**	-	1200	-
Yield and Ultimate Compressive Strength in Y (90º) (Scu or σu) [MPa]	**250**	-	250	-
Yield and Ultimate Compressive Strength in Z (Stu or σu) [MPa]	**250**	-	-	-
Yield and Ultimate Shear Strength 45º (Stu or σu) [MPa]	**49.4125**	51.721 / 47.104	-	-
Yield and Ultimate In-plane Shear Strength in XY (τ12u) [MPa]	**70**	-	70	-
Thermal Expansion Coefficient in X (0º) [/K]	**-0.3**	-	-0.3	-
Thermal Expansion Coefficient in Y (90º) [/K]	**28**	-	28	-
Thermal Expansion Coefficient in Z [/K]	**28**	-	28	-

a) Experimental data obtained from attached extensometer;

b) Experimental data obtained from glued extensometers;

Table 13 – Properties of Epoxy + Bi Carbon Fiber (160[gr/m^2])

		Experimental Bi (a / b)	ASTM calculations	Uni	Average Experimental Database [65]	Theoretical [66]
Resin Epoxy SR 1500 + Hardener Sicomin SD 2505 (100 [g] Epoxy - 33 [g] Hardener) (20ºC Cure, Dry heat air conditioning, -0.5 Bar vacuum)	-	-	-	-	-	-
Approximate Liquid Relations: 100 [g] Carbon fiber - 85 [g] Epoxy + Hardener	-	-	-	-	-	-
Fiber Mass Percentage [%] (for laminate with 10 Plies)	**0.63**	-	-	-	-	-
Average Ply thickness [mm] (for laminate with 10 Plies)	**0.19**	-	-	-	-	-
Mass Density [g/mm^3] (for laminate with 10 Plies)	**0.0013**	0.0013	-	-	0.0016	-
Tensile Modulus in X (E1) [MPa]	**44792.61**	54222 / 44792.61	-	-	70000	52665
Tensile Modulus in y (E2) [MPa]	**53192.65**	60003 / 53192.65	-	-	70000	52665
Tensile Modulus in Z (E3) [MPa]	**9172.87**	-	-	9172.87	-	11285
Longitudinal Tensile Modulus in 45º (E1') [MPa]	**17433.91**	6832 / 17433.91	-	-	19100	-
Poisson's Ratio in XY (ν12)	**0.06**	N.A / 0.06	-	-	0.1	0.054
Poisson's Ratio in YZ (ν23)	**0.388**	-	-	-	-	0.388
Poisson's Ratio in XZ (ν13)	**0.388**	-	-	-	-	0.388

In-plane Shear Modulus in XY (G12) [MPa]	**5000**	-	-	-	5000	2474
Out-of-plane Shear Modulus in YZ (G23) [MPa]	**2889**	-	-	-	-	2889
Out-of-plane Shear Modulus in XZ (G13) [MPa]	**2889**	-	-	-	-	2889
Yield and Ultimate Tensile Strength in X (0º) (Stu or σu) [MPa]	**622.598**	N.A / 622.598	-	-	600	-
Yield and Ultimate Tensile Strength in Y (90º) (Stu or σu) [MPa]	**508.568**	515.003 / 502.133	-	-	600	-
Yield and Ultimate Tensile Strength in Z (Stu or σu) [MPa]	**22.46725**	-	-	22.46725	-	-
Yield and Ultimate Compressive Strength in X (0º) (Scu or σu) [MPa]	**570**	-	-	-	570	-
Yield and Ultimate Compressive Strength in Y (90º) (Scu or σu) [MPa]	**570**	-	-	-	570	-
Yield and Ultimate Compressive Strength in Z (Stu or σu) [MPa]	**250**	-	-	250	-	-
Ultimate Shear Strength 45º (Stu or σu) [MPa]	**115.33**	102.53 / 128.138	-	-	120	-
Yield Strength 45º (σc) [MPa]	**57.66**	50 - 70 / 50 - 70	57.6645	-	-	-
Ultimate In-plane Shear Strength in XY (τ12u) [MPa]	**90**	-	-	-	90	-
Yield In-plane Strength (τ12c) [MPa]	**45**	-	45	-	-	-
Thermal Expansion Coefficient in X (0º) [/K]	**2.1**	-	-	-	2.1	-
Thermal Expansion Coefficient in Y (90º) [/K]	**2.1**	-	-	-	2.1	-
Thermal Expansion Coefficient in Z [/K]	**28**	-	-	-	28	-

a) Experimental data obtained from attached extensometer;

b) Experimental data obtained from glued extensometers;

Table 14 – Airex C70.75.

	Experimental	Manufacturer data [70]	Theatrical [71]
Mass Density [g/mm^3]	0.000089	-	-
Tensile Modulus E [MPa]	-	66	-
Compression Modulus E [MPa]	-	104	-
Elastic Modulus (Average between tensile and compressive) [MPa]	-	85	-
Shear Modulus (G) [MPa]	-	30	-
Yield and Ultimate Tensile Strength (Stu or σu) [MPa]	-	2	-

Compressive Strength (Fcu or σu) [MPa]	-	1.45	-
Shear Strength (τu) [Mpa]	-	1.2	-
Poisson's Ratio	-	0.3	-
Thermal conductivity at room temperature (20ºC) [W/m.K]	-	0.033	-
Thermal expansion coefficient [/K]	-	-	0.00004387

Table 15 – Epoxy + Kevlar 49.

	Experimental	Average Experimental Database [65]
Mass Density [g/mm^3]	0.0012	-
Fiber Mass Percentage [%]	53	-
Fiber Volume Percentage [%]	-	44
Yield Tensile Strength (0º) [MPa]	-	410
Yield Compression Strength (0º) [MPa]	-	199

Annex 7

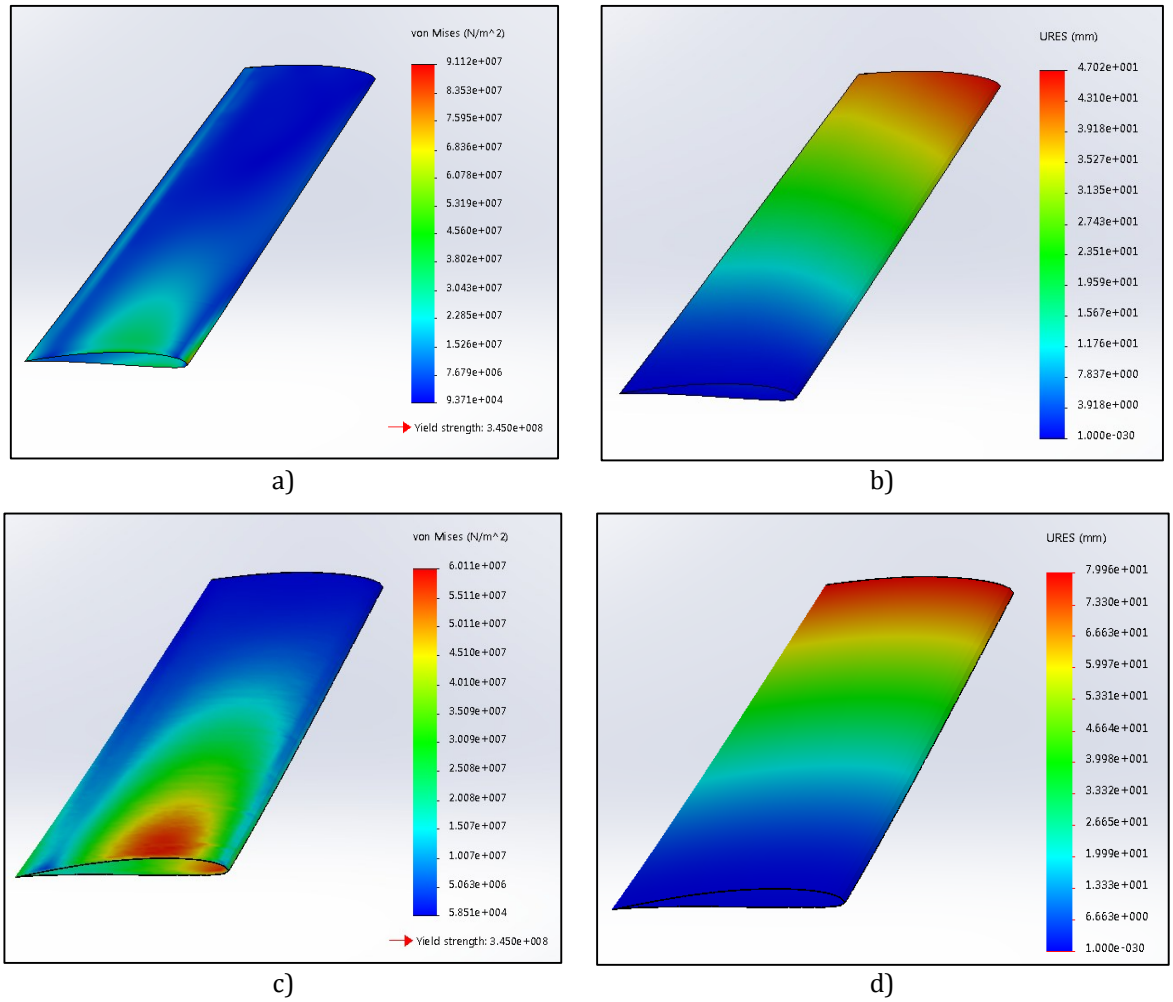

a) b)

c) d)

Figure 81 – a) 2D Stress. Max Stress: 91.12 [MPa]; b) 2D Displacement. Max Displacement 47.02 [mm]; c) 3D Stress. Max Stress: 60.11 [MPa]; d) 3D Displacement. Max Displacement: 79.96 [mm].

Annex 8

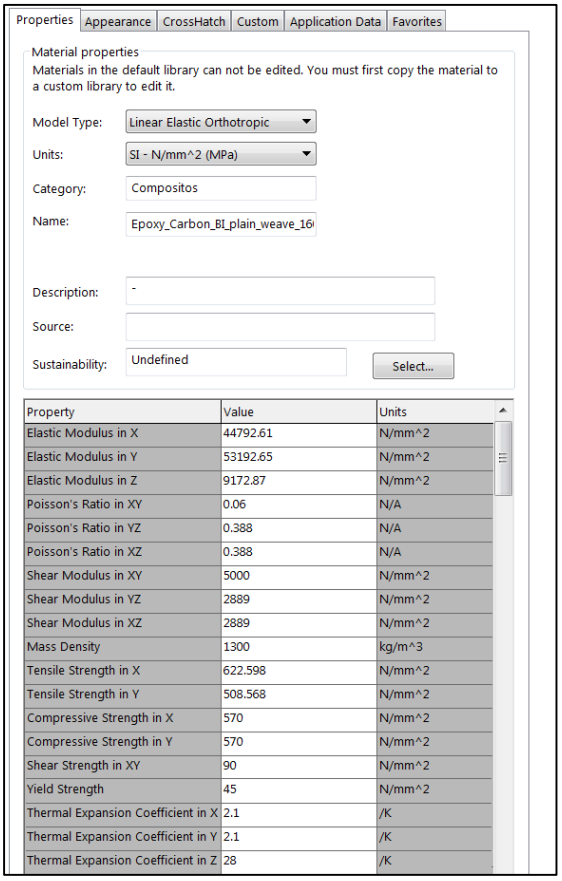

Figure 82 – Material properties menu.

Annex 9

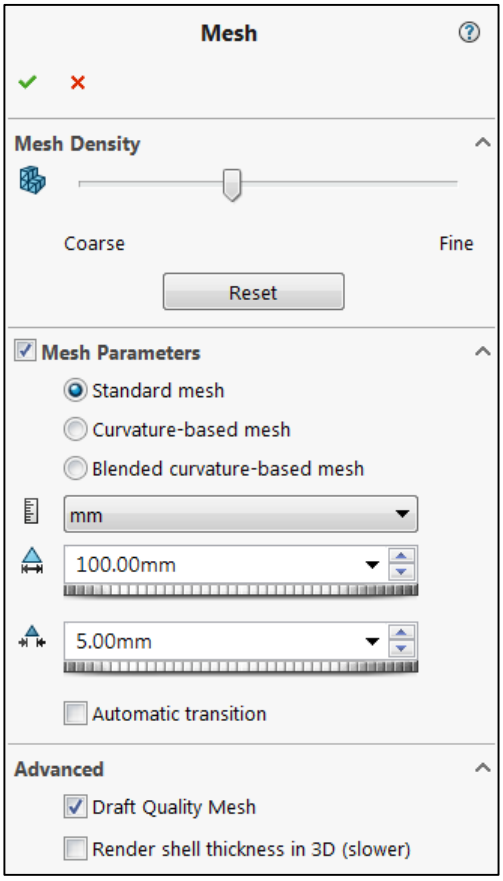

Figure 83 – Mesh parameters definition.

Annex 10

Table 16 – Simplified initial model characteristics.

	Material density (Carbon_Bi_160g) [g/mm^3]	0.0013					
	Section	0-25% (root)	25-50%	50-75%	75-100% (tip)		
Skin	**Surface Area [mm^2]**	1018242.49	761113.4	720570.11	736987.59		
	Thickness [mm]	1.9	1.9	1.9	1.9		
	Calculated Mass [g]	2515.05895	1879.950098	1779.808172	1820.359347		
1st Spar	**Surface Area CAPS [mm^2]**	126718.74	120172.91	113666.82	107209.57		
	Thickness [mm]	1.9	1.9	1.9	1.9		
	Calculated Mass [g]	312.9952878	296.8270877	280.7570454	264.8076379		
	Surface Area WEBS [mm^2]	238319.94	225731.14	213147.7	201199.45		
	Thickness [mm]	1.9	1.9	1.9	1.9		
	Calculated Mass [g]	588.6502518	557.5559158	526.474819	496.9626415		
2nd Spar	**Surface Area CAPS [mm^2]**	63360.71	60089.61	56838.21	53624.56		
	Thickness [mm]	1.9	1.9	1.9	1.9		
	Calculated Mass [g]	156.5009537	148.4213367	140.3903787	132.4526632		
	Surface Area WEBS [mm^2]	61212.1	57943.72	54692.08	51445.4		
	Thickness [mm]	1.9	1.9	1.9	1.9		
	Calculated Mass [g]	151.193887	143.1209884	135.0894376	127.070138		
Ribs	**Surface Area [mm^2]**	60933.06	43073.79	18272.03	38951.68		
	Thickness [mm]	1.9	1.9	1.9	1.9		
	Calculated Mass [g]	150.5046582	106.3922613	45.1319141	96.2106496		
ALL Components	**TOTAL MASS [g]**	3874.903989	3132.267688	2907.651767	2937.863078	**12852.68652**	TOTAL
	Max Stress [Pa]	-	-	-	-	**9.306E+07**	
	Max Displacement [mm]	-	-	-	-	**117.3**	